Control of a separating turbulent boundary layer using pulsed jets

A thesis presented for the Master's degree in Aerospace Engineering

Politecnico di Torino
Academic year 2024/2025

Supervisors
prof. Francesco Avallone
prof. Marios Kotsonis
Dr. Woutijn J. Baars
PhD candidate Parisa Ghanoni Bostanabad

Candidate
Gabriele Gagliasso

”Venderò il mio diploma
ai maestri del progresso
per costruire un nuovo automa
che dia a loro più ricchezza e a me il successo”
E. Bennato

Abstract

This thesis investigates the control of a separating turbulent boundary layer using periodic excitation via pulsed jets. Experiments were conducted on an airfoil-like model subjected to an adverse pressure gradient at its curved trailing edge. Two different jet array configurations - streamwise and skewed slits - were compared to assess their effectiveness in modifying the flow. Detailed characterization of the actuation system was performed using hot wire anemometry, and the interaction between the pulsed jets and the boundary layer was studied through static surface pressure measurements and particle image velocimetry. Results indicate that skewed slits enhance the coherence of the generated vortical structures, leading to more effective separation control compared to streamwise slits. The study also highlights the critical influence of actuation frequency, velocity ratio, and jet orientation on the separation dynamics; moreover, it was found that the flow field - when subjected to actuation - shows a much higher degree of variability in the spanwise direction than anticipated.

The findings contribute to a deeper understanding of active flow control strategies for drag reduction and improved aerodynamic performance in practical applications.

Acknowledgements

Thank you to my family, for their continuous support, both material and spiritual; I wouldn't be where I am today without them.

Thank you to all of my long-time friends, Alessandro, Chiara, Federico, Mario, Paolo, Riccardo, Stefano, for always providing me with a safe space and for never giving up on our friendship, even when you deserved better.

Thank you to the friends I've met along the way, Andrea, Burak, Vittorio, for always being there to share a laugh when it was needed the most.

Thank you to my engineering family, Squadra Corse, for always pushing me to be a better version of myself and for giving me memories and marks I will forever carry with me. To Luco and Vittorio in particular, thank you for the countless hours spent dreaming about a brighter future.

List of Figures

Contents

Introduction

The term *separation control* refers to the notion of artificially delaying or advancing the detachment and/or reattachment process through passive or active systems[8].

Figure 1.1: Stall on the suction side of an airfoil, visible with the aid of flow-visualization tools, from [35].

Flow separation plays a key role in modifying the flow field around a body; it is a very important problem in fluid dynamics, as separation is the main source of pressure drag in many industrial applications, such as road vehicles[13], and drag reduction studies have been conducted on the topic[20].

The *effectiveness* of a separation control device is defined differently depending on the specific case study; for instance, if the aim of separation control is to increase the maximum angle of attack before aerodynamic stall, separation control is more effective if the separation point is moved downstream along the surface; if separation is locally induced to increase lift, such as in Gurney flaps[32], the effectiveness can be related to the increase in lift compared to the uncontrolled case. A peculiar case of separation control is the one operated by Kalyankar et al. [16]: separation control is used to increase and decrease lift of specific aerodynamic surfaces, with the aim of inducing moments to control an aircraft without the use of conventional moving control surfaces; instead, moments around the three axes are induced by strategically stalling and de-stalling dedicated surfaces around the aircraft.

1.1 Research aim and document structure

The aim of this thesis is to explore the effects that periodic excitation with pulsed jets has on the turbulent separation over a three-dimensional wing-like's adverse-pressure-gradient segment; in particular, a comparison between two different geometrical configurations of jet arrays was operated: in both cases, the actuation block consists of an array of twenty-six jets, positioned along the spanwise direction at a fixes streamwise location; as will be shown in the following chapter, there is very little knowledge about the influence of geometrical parameters on the preservation of coherence of the structures generated by periodic excitation; in particular, a comparison between *skewed* and *streamwise* jet orifices was operated, with the aim of gaining a better understanding of the mechanisms that favor one configuration over the other.

Chapter 2 presents a structured summary of state-of-the-art knowledge about separation and separation control using pulsed jets; chapter 3 presents the experimental methodology and techniques applied to this case study; chapter 4 walks through the characterization of the actuation system used for the present work; chapter 5 presents the results obtained from pressure measurements and PIV fields; finally, chapter 6 presents conclusions, along with further recommendations and suggestions for future studies.

Background

Most of the theoretical background information about boundary layer theory and separation was extrapolated from Schlichting and Gersten [28], Arina [2] and Pope [22], and it all refers to *incompressible* flows (Mach number lower than 0.3).

2.1 The turbulent boundary layer

At high Reynolds number Re, viscous effects are only relevant in a small region close to the wall, commonly known as the *boundary layer* or *frictional layer*; originally hypothesized by Prandtl in the early 20th century, it's been a major subject of studies in fluid mechanics ever since.

The boundary layer is the region of the flow field where velocity smoothly transitions from its zero-value at the wall (*no-slip* condition) to its freestream value; fig. 2.1 shows a schematic of the formation of a boundary layer over a zero-incidence flat plate.

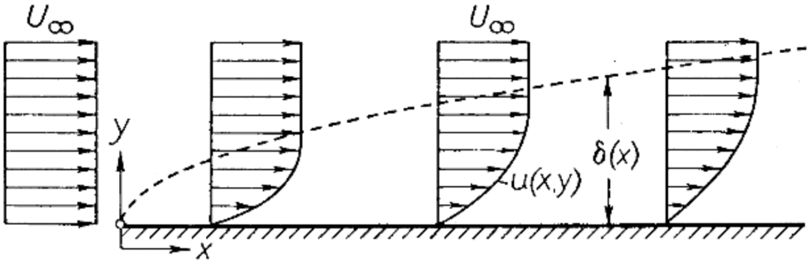

Figure 2.1: Formation of boundary layer over a flat plate; U_∞ is the freestream velocity, while $u(x, y)$ is the local velocity within the boundary layer. The dotted line represents the upper limit of the BL, while $\delta(x)$ its local thickness, a concept explained below. Image from Schlichting and Gersten [28].

Boundary layer thickness. Fig. 2.1 also shows the *boundary layer thickness* $\delta(x)$, defined as the point where the local velocity has 99% of its freestream value; for this reason, it is often referred to as δ_{99}.
It is important to note the boundary layer is an artificially introduced concept, thus no real boundary layer limit exists; therefore, there are other ways to define the thickness of a boundary layer:

1. *Displacement thickness*, defined as

$$\delta^* = \int_{y=0}^{+\infty} \left(1 - \frac{u}{U_e}\right) dy$$

   where U_e represents the local velocity outside of the BL; the displacement thickness gives an idea of how far off the wall the streamlines have been displaced by the presence of the boundary layer; fig. 2.2 gives a schematic idea of the size of the displacement thickness.

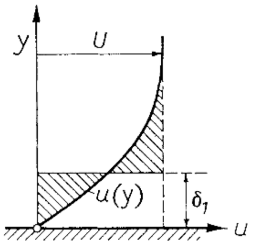

Figure 2.2: Schematic of a boundary layer over a flat plate; δ_1 refers to the displacement thickness. Image from Schlichting and Gersten [28].

2. *Momentum thickness*, defined as

$$\theta = \int_{y=0}^{+\infty} \frac{u}{U_e}\left(1 - \frac{u}{U_e}\right) dy$$

The momentum thickness can be interpreted as the distance from the wall where the momentum flow rate is the same as it would be in an inviscid flow.

3. *Shape factor*, the ratio between the two aforementioned thicknesses:

$$H = \frac{\delta^*}{\theta}$$

The shape factor is widely used to differentiate laminar and turbulent boundary layers: according to Blasius, $H = 2.59$ for laminar boundary layers, while $H = 1.3 - 1.4$ for turbulent ones.

Skin friction. A very important quantity associated to boundary layers is the *skin friction* τ_w, as it leads to aerodynamic drag; according to Newton's law of friction, given the fluid's *dynamic viscosity* μ:

$$\tau_w(x) = \mu \left(\frac{\partial U}{\partial y}\right)_{y=y_w}$$

where y is the coordinate normal to the wall.
The non-dimensional *skin friction coefficient* can also be defined:

$$c_f(x) = \frac{2\tau_w(x)}{\rho U_\infty}$$

The *friction drag*, the force exchanged between the wall and the fluid because of the presence of the boundary layer, can be obtained by integrating the skin friction τ_w:

$$D_\tau = b \int_{x=0}^{x=l} \tau_w(x) dx$$

where b is the wall's width, l its length and x the streamwise coordinate.

Transition to turbulence. Considering viscous flow over a flat plate, the boundary layer becomes *turbulent* when the *local* Reynolds number, defined as $Re_x = \frac{U_\infty x}{\nu}$ (where x is the streamwise coordinate starting from the leading edge of the flat plate and ν is the fluid's kinematic viscosity) exceeds its critical value; it has been widely observed that, for unpertubed flows:

$$Re_{x,crit} = 5 \cdot 10^5$$

Transition to turbulence is commonly associated to a sudden increase of skin friction and BL thickness.

2.1.1 Universal law of the wall

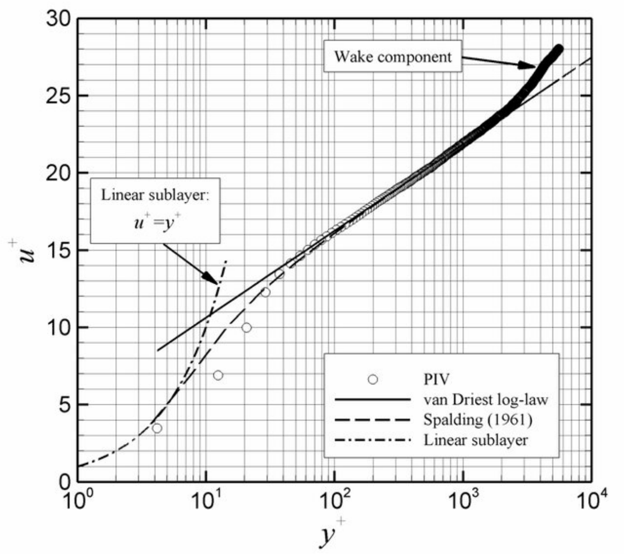

Figure 2.3: Graphic representation of the universal law of the wall; the red line represents the velocity distribution in the boundary layer, while the blue lines represent the velocity distributions in the *viscous sublayer* and in the *log law region.* Image from Humble et al. [14].

For a turbulent boundary layer it is common to define a few fundamental dimensional and non-dimensional quantities:

1. $u_\tau = \sqrt{\tau_w/\rho}$, commonly referred to as *friction velocity*
2. $\eta = y/\delta$
3. $u^+ = u/u_\tau$
4. $y^+ = yu_\tau/\nu$

where ν is the fluid's kinematic viscosity.

It can be shown that for any turbulent boundary layer one can write what is known as the *universal law of the wall*, which correlates the non-dimensional velocity u^+ and the non-dimensional wall coordinate y^+, namely $u^+ = f(y^+)$; the *inner layer*, the region of the boundary layer closest to the wall, can be divided into three subregions:

1. *pure viscous sublayer* ($0 \le y^+ < 5$): viscous effects dominate, the relation is linear:

$$u^+ = y^+ \tag{2.1}$$

2. *buffer layer* ($5 \le y^+ < 70$): viscous effects start to subside inertial effects, and the following law is obeyed:

$$\frac{du^+}{dy^+} = \frac{1}{1 + (A+B)(y^+)^3} + \frac{B(y^+)^3}{1 + \kappa B(y^+)^4} \tag{2.2}$$

where

$$\begin{cases} \kappa = 0.41 \\ A = 6.1 \cdot 10^{-4} \\ B = 1.43 \cdot 10^{-3} \end{cases}$$

3. *overlap layer* ($70 \le y^+$), also known as *log-law region*, where the relation is logarithmic:

$$u^+ = \frac{1}{\kappa} ln\ y^+ + C^+ \tag{2.3}$$

with $C^+ = 5$.

Fig. 2.3 shows a graphic representation of the universal law of the wall.

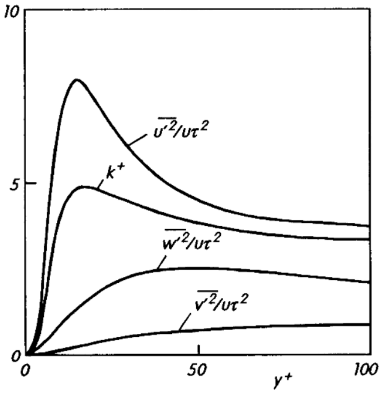

Figure 2.4: Graphic representation of the energy content of a turbulent boundary layer, in terms of Reynolds normal stresses and turbulent kinetic energy. Image from Schlichting and Gersten [28].

Fig. 2.4 shows the energy distribution in a turbulent boundary layer; it is immediately noticeable how the majority of the turbulent fluctuations are contained in the buffer layer, the region with the highest production of turbulent kinetic energy.

2.2 Boundary layer separation

In flows with a high Reynolds number, a fluid particle converts pressure to kinetic energy when encountering a *favorable pressure gradient* (FPG), and kinetic energy to pressure when encountering an *adverse pressure gradient* (APG); however, the kinetic energy of the particles close to the wall is dissipated by viscosity, and if the APG is too strong, i.e. $-dp/dx \ll 0$, such particles are too "weak" to overcome it, and *reverse flow* can occur close to the wall, leading to streamlines not following the wall's curvature anymore: this process is called ***boundary layer separation***.
A useful indicator for the *local* pressure gradient's sign and magnitude is the *Clauser pressure gradient parameter*:

$$\beta = \frac{\delta^*}{\tau_w}\frac{dP_e}{dx} \tag{2.4}$$

where P_e denotes the pressure just outside of the TBL.

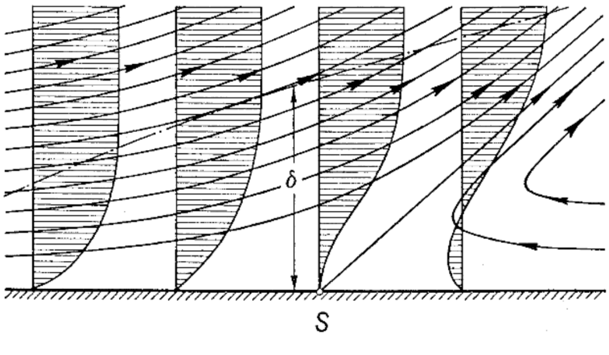

Figure 2.5: Sketch of a boundary layer as it approaches separation; the velocity profile at various streamwise coordinates is shown. Image from Schlichting and Gersten [28].

Figure 2.5 shows the process in its different stages: in the first two velocity profiles the BL is firmly attached to the wall; due to APG, however, the third velocity profile presents an *inflection point* and a local minimum at the wall: this is the coordinate after which the flow reverses and separation begins, as shown in the fourth velocity profile.
In the case of an unsteady separating boundary layer, the *forward flow fraction* γ is introduced, defined as the fraction of time when the near-wall flow goes in the main streamwise direction; in this context, Simpson [30] and Mohammed-Taifour and Weiss [19] describe six characteristic points of a separated boundary layer:

1. *incipient detachment* (ID), the first point with $\gamma = 0.99$
2. *intermittent transitory detachment* (ITD), the first point with $\gamma = 0.8$
3. *transitory detachment* (TD), the first point with $\gamma = 0.5$
4. *detachment*, (D), the first point where $\tau_w = 0$
5. *transitory reattachment* (TR), the second point where $\gamma = 0.5$
6. *complete reattachment* (CR), the second point where $\gamma = 0.99$

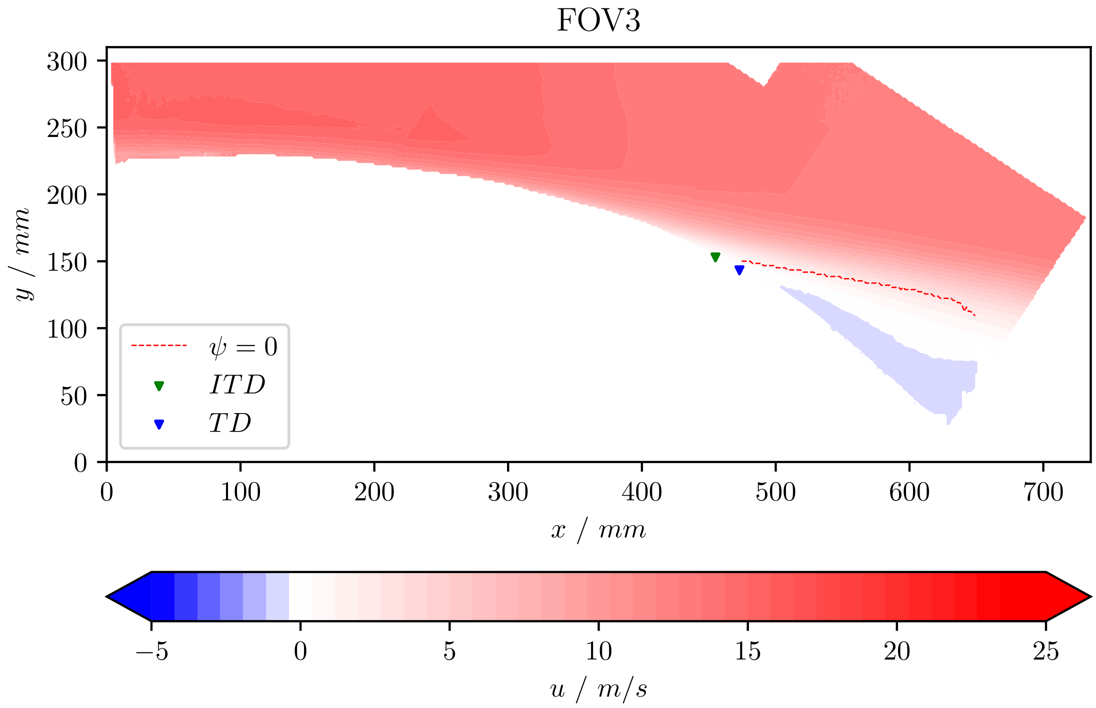

Figure 2.6: Example test case from one of the PIV cases in the context of the present work; *ITD* and *TD* are marked in the figure; the contour represents $x-$velocity component. The field of view presents the curved section of the wing-like segment used for the experiment; the *white* part below the velocity field represents the masked wall.

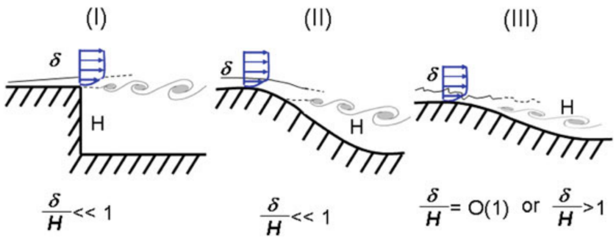

Figure 2.7: Categories of separation, as described in Deck [5].

Furthermore, as sketched in fig. 2.7 Deck [5] describes three different categories of separation, depending on the origin of the phenomenon:

I. *geometry-fixed separation*, where a sharp edge imposes the detachment point, such as on a forward facing step

II. *APG-induced separation*, where the detachment point is free to move along the surface; this is the type of separation found on the suction side of airfoils at low angles of attack

III. separation strongly influenced by incoming boundary layer dynamics

Categories II and III are of particular interest for this work, as the separation point is free to move along the surface, allowing for an extra degree of freedom in terms of separation control.

2.2.1 The recirculation bubble

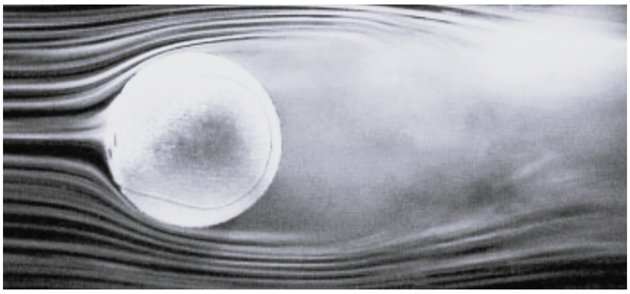

Figure 2.8: Visualization of the flow around a tennis ball made with the aid of smoke trails; the separated region is clearly visible downstream of the ball (right side): the streamlines fuse together and they are not well defined anymore, a clear sign of recirculation. Image courtesy of *NASA Ames Research Center and Cislunar Aerospace Inc.*

As mentioned above, boundary layer separation is caused by a region of reversed flow; this inevitably leads to a region affected by strong *recirculation*: this is what is called a *turbulent separation bubble*, TSB. A visual example of the recirculation region is provided in fig. 2.8.

2.3 Unsteady separation

An extensive study of unsteady recirculation bubble dynamics is found in Wu, Meneveau, and Mittal [36], which conducted a direct numerical simulation of an APG separation on a flat plate; they observed three characteristic frequencies: *high*, *medium*, and *low*; dimensional analysis reveals the most common non-dimensional number used for frequencies in fluid mechanics: the *Strouhal number*, defined as

$$St = \frac{fL}{U} \tag{2.5}$$

where f is the frequency, L is a reference length and U is a reference velocity.

High and medium frequency. The high- and medium-frequency modes appear to be located in the upstream region of the separation bubble, and Wu, Meneveau, and Mittal [36] speculate that they could be related to the Kelvin-Helmholtz instability in the shear layer.
As shown by the topological analysis in figure 2.9 the two modes are characterized by coherent, periodic spanwise structures, just like for the KH instability.

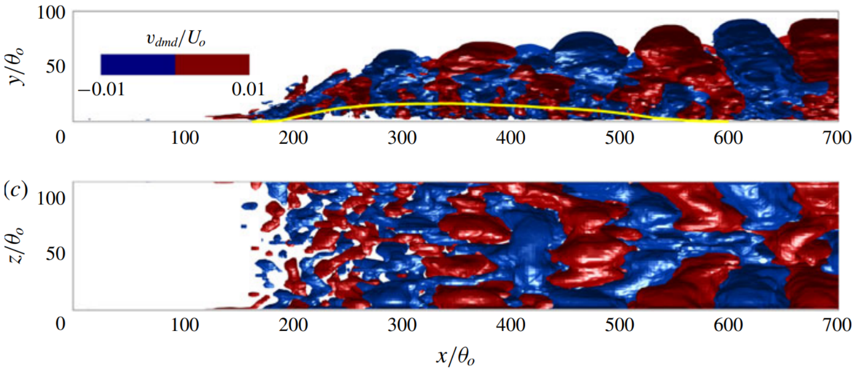

(a) *high-frequency*

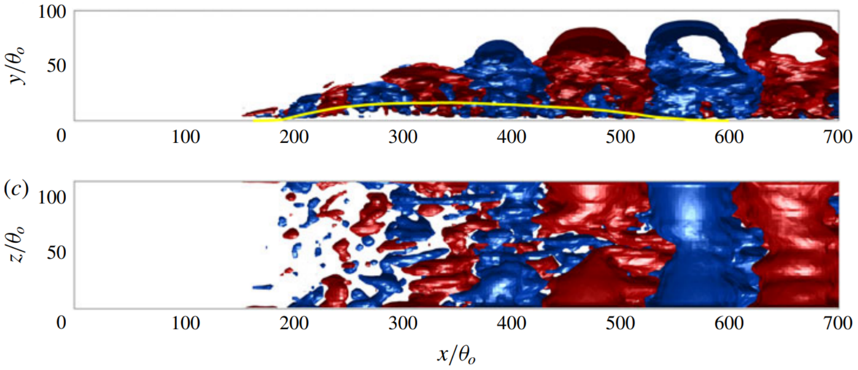

(b) *medium-frequency*

Figure 2.9: Isosurfaces of the real part of the *medium-* and *high-frequency* DMD modes, from [36].

Moreover, Wu, Meneveau, and Mittal [36] report that the Strouhal numbers for the high- and mid-frequency modes are well within the range of literature for the dominant frequency in a turbulent mixing layer, providing even stronger support for the KH hypothesis.
The vortex-rollup mechanism caused by this instability evolves downstream into the classical *shedding* mode present in fixed-separation phenomena, as pointed out by Weiss, Mohammed-Taifour, and Schwaab [34].

Low frequency. The low frequency mode, sometimes referred to as ”breathing”[37], or ”flapping”[34][6], is characterized by back and forth motion of the detachment and reattachment points; its frequency is usually an order of magnitude less than the *high-* and *mid-frequency* values[34][36].
The topology of such low frequency mode is very different from the high- and medium-frequency ones: as shown in fig. 2.10, the DMD analysis of a separating turbulent boundary layer on a flat plate performed by Wu, Meneveau, and Mittal [36] shows long structures elongated in the streamwise direction.

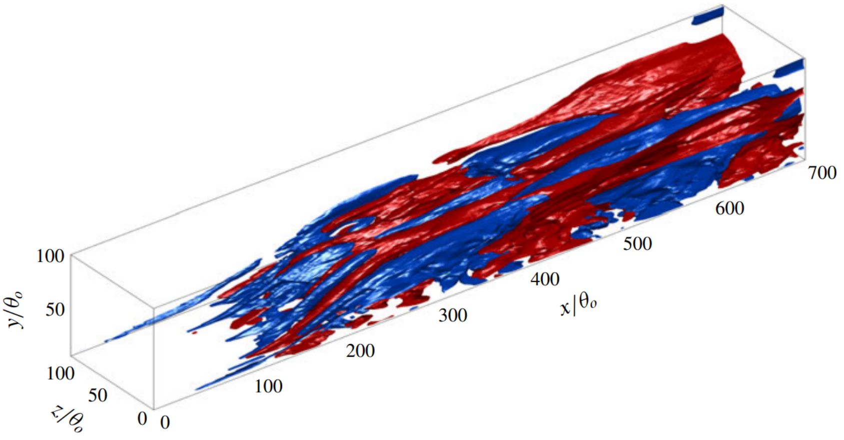

Figure 2.10: Isosurfaces of the real part of the *low-frequency* DMD mode, from [36].

The origin of this mode is still very much a question of research, but a relation to the Görtler instability seems to emerge from the aforementioned topological analysis.
Görtler instability was first studied in Görtler [11], and it is characterized by streamwise rollers; it manifests itself as the Görtler number exceeds 0.3; it is defined as

$$G_T = \frac{U_\infty \theta}{\nu}\sqrt{\frac{\theta}{R}} \tag{2.6}$$

where θ is the boundary layer's local momentum thickness ν is the fluid's dynamic viscosity, and R is the mean flow's curvature radius.
Wu, Meneveau, and Mittal [36] also observe that the low frequency is precisely half the medium frequency (i.e., a subharmonic), which could be an indication of vortex pairing of the medium frequency mode.

2.4 Separation control

Separation control can be enacted through active or passive systems; these systems trigger mechanisms that fall into the wider category of *boundary layer control*, which refers to the act of causing the boundary layer to behave differently than it naturally would[31].
Gad-el-Hak and Bushnell [8] identify four different ways for dealing with separation control:

- methods that affect the shape of the velocity profile in the incoming boundary layer;
- methods for time-dependent separation events;
- methods that make use of *turbulators*, devices that enhance turbulence in low-Reynolds applications;
- methods that promote *near-wall momentum addition.*

2.4.1 Near-wall momentum addition

Within the category of momentum addition devices, the most obvious example are *passive vortex generators*, small appendices mounted on aerodynamic surfaces with the aim of delaying separation; visual examples are presented in fig. 2.11, where vortex generators are used behind the nose cone of a commercial aircraft and on the sidepod of a racecar.

(a) Nose cone of a Boeing 737 aircraft (b) Close-up of a 2013 Mercedes-AMG Formula 1 car

Figure 2.11: Examples of vortex generators used in engineering applications.

Passive vortex generators are angled fins, that generate a pressure difference between their two sides once they're immersed in moving flow; such pressure difference generates a streamwise vortex that is then convected downstream, bringing high-momentum fluid closer to the wall, thus energizing the boundary layer in the APG region.

Active vortex generators

The same principle forms the base for *active* vortex generators, which work by injecting high-momentum fluid in the boundary layer through the formation of fluid structures; generally, active vortex generators consist of either *zero-net mass flow* jets (also called *synthetic* jets), or actual non-zero-net mass flow jets; in contrast to passive vortex generators, active tools allow for *modulation* of the control, paving the way for interaction with the pre-existing flow structures described in section 2.2.1; a review of flow control through preiodic excitation can be found in Greenblatt and Wygnanski [12].

Synthetic and non-synthetic jets have been extensively studied for a wide variety of applications: Gilarranz, Traub, and Rediniotis [9] found that placing synthetic jets on the surface of a NACA0015 airfoil at $Re \simeq 9 \cdot 10^5$ can lead to a strong increase in C_L for α between 10^o and 15^o; Ramaswamy and Schreyer [23] studied the effects of jet vortex generators on a shock-induced separation; Abe et al. [1] compared the differences between the effects of pulsed jets and plasma actuators on a stalled NACA0015 airfoil through an implicit Large Eddy Simulation; Rice, Taylor, and Amitay [24] explored the effects of pulsed modulation of synthetic jets in two different chord-positions on a S817 airfoil undergoing dynamic stall, and observed a reduction in C_L hysteresis; Vukasinovic, Rusak, and Glezer [33] studied the effects of actuation upstream of a backward-facing step; Joseph, Amandolèse, and Aider [15] observed a Reynolds-dependent drag reduction when actuation pulsed jets is done on a 25^o slant angle Ahmed body; Wu et al. [37] performed a DNS of a pressure induced TSB, highlighting the importance of physics-base flow control by acting on specific turbulent structures with the use of synthetic jets, and observed a reduction in pressure loss as a result; Mohammed-Taifour, Floc'H, and Weiss [18] observed a reduction in separation bubble size within their experimental study of the effects of active forcing on a pressure-induced TSB over a flat plate.

2.4.2 Jets in crossflow

To understand the physics behind active vortex generators, one must first understand the phenomenology of a jet interacting with a perpendicular crossflow; what follows is a presentation of such phenomenology for incompressible flows, inspired by the work of Mahesh [17].

When discussing jets in crossflows, it is first essential to define two fundamental parameters: the *velocity ratio* r_j and the *momentum ratio* μ_j:

$$r_j = U_j / U_\infty \tag{2.7}$$

$$\mu_j = \frac{\rho_j U_j}{\rho_\infty U_\infty} \tag{2.8}$$

where U_j is the jet's mean outlet velocity; for pulsed jets, U_j is the maximum jet velocity.

With regard to vortical structures, one can observe three main features:

1. a pair of counter-rotating vortices (CVP), for jets with high r_j;
2. Horseshoe and wake vortices;
3. Hairpin vortices, for jets with low r_j.

Counter-rotating vortex pair, CVP. Whenever a jet with a high enough velocity ratio encounters a crossflow, its cross-section velocity profile evolves from a uniform distribution into a pair of counter-rotating vortices; a visual representation of this evolution in time is provided in fig. 2.12.

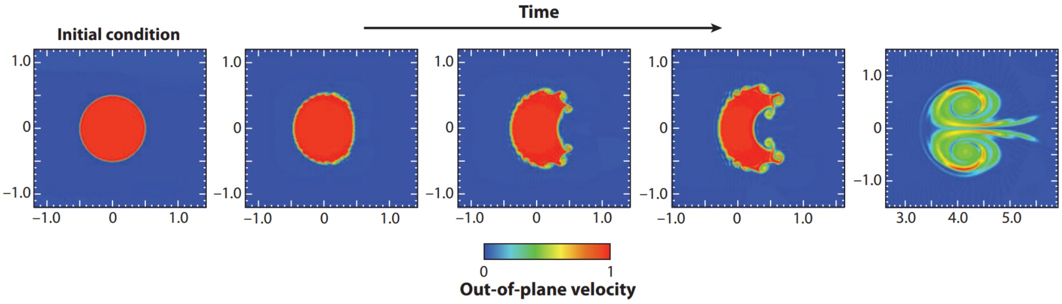

Figure 2.12: Evolution in time of a circular region of out-of-plane velocity in the presence of crossflow, from [17].

The two vortices, whose intial vorticity is perpendicular to the crossflow, are subsequently convected, and their vorticity aligns with the freestream.
The mechanism that leads to their formation has been long debated; a qualitative and intuitive explanation, initially provided by Breidenthal [3], views the jet as an 'impulse' introduced to the crossflow. This impulse generates upwash, resulting in the formation of vortices similar to the tip vortices observed at the ends of finite-span wings.
However, the general consensus on this topic agrees on a different explanation: the jet's shear layer is titlted and folded by the presence of crossflow, and this leads to the circulation necessary for the generation of a vortex pair; this process is represented schematically in fig. 2.13a.

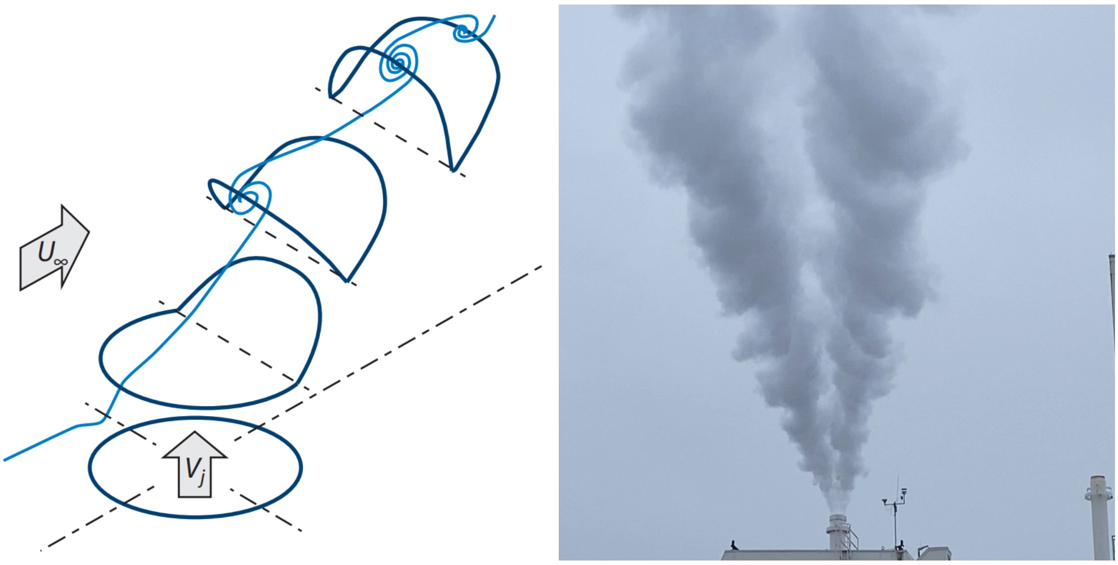

(a) Schematic representation of the jet's shear layer and formation of vortex, from [17].

(b) Real-world visualization of CVP, picture taken by the author of this thesis on a fortunate Wednesday morning at the TU Delft campus.

Figure 2.13: Visualizations of a circular jet evolving into CVP when encountering crossflow.

Horseshoe and wake vortices. As the freestream's boundary layer approaches the jet, it encounters an adverse pressure gradient; due to the mechanisms explored in section 2.2, the BL separates and generates a spanwise-oriented vortex, which is then convected downstream and around the jet, taking a horseshoe-like shape.

Wake vortices are vortices that are found downstream of the jet, whose axis is perpendicular to the freestream direction, and they extend from the wall to the downwind-side of the jet.
At a first glance, it could seems that the mechanisms that lead to their formation and shedding are equivalent to those found for solid cylinders immersed in a high-Reynolds number flow; however, it can be shown that the wake behind a cylinder is very different from the wake behind a jet at similar Reynolds number.

Evidence shows that wake vortices originate from separation events in the freestream's boundary layer downstream of the jet; it is also interesting to note that wake vortices and horseshoe vortices interact with each other: horseshoe vortices with the same sign of vorticity as the freestream's boundary layer merge in the wake system, while those with opposite sign merge into the CVP system.

Hairpin vortices. When the jet's velocity ratio is low (approximately, $r_j < 1$), the structure of the aforementioned vortices is different.
At low velocity ratios, the vorticity of the incoming freestream boundary layer overwhelms the vorticity of the jet's shear layer at the leading edge; this process leads to vortex shedding at the jet's trailing edge, with the formation of hairpin vortices; if the Reynolds number increases, these vortices become unstable as they evolve.

Jet trajectory

In separation control, the trajectory of a jet in crossflow is a critical factor. If the jet penetrates too far into the boundary layer, the incoming flow may perceive it as a blockage, potentially increasing drag and inducing separation. Conversely, if the jet remains too close to the wall, it may entrain low-momentum fluid into the higher regions of the boundary layer, counteracting the intended control effect. Achieving the right balance in jet penetration is essential to effectively manipulate the flow and delay separation.

A common way to scale the trajectory of a jet is by using the product between the velocity ratio r_j and the jet's diameter d; if x is the freestream direction and y is the initial direction of the jet, the trajectory is described by an exponential law:

$$\frac{y}{r_j d} = A\left(\frac{x}{r_j d}\right)^B \tag{2.9}$$

where A and B are determined experimentally; commonly, $1.2 < A < 2.6$ and $0.28 < B < 0.34$.

However, as pointed out by Breidenthal [3], eq. 2.9 is valid under the hypothesis that the jet is point-like source of momentum flux viewed from the far field; in regards of the far field (where the CVP is assumed to be fully developed), they propose to treat the jet as a point-like source of normal momemtum, yielding the following law:

$$\frac{y}{l} \propto \left(\frac{x}{l}\right)^{1/3} \tag{2.10}$$

where, in the case of a jet's fluid with the same density as the crossflow's, the length scale l is equal to $\sqrt{\pi/4}\; r_j d$.

Other scalings for the jet trajectory have been proposed, such as using $r_j^2 d$ instead of $r_j d$, but evidence shows that they fail to fit a wide range of data; this is because there are many factors at play when it comes to the penetration extent of a jet in a crossflow's boundary layer: a laminar jet penetrates more than a turbulent one, and a thicker boundary layer allows more penetration. The momentum distribution is another aspect that has an effect on how far the jet penetrates: evidence has shown that pipe-generated jets behave differently compared to nozzle-generated ones.

For all these reasons, Muppidi and Mahesh [21] suggest the law

$$\frac{y}{r_j d} = A'\left(\frac{x}{r_j d}\right)^B \left(\frac{h}{d}\right)^C \tag{2.11}$$

where

$$\frac{h}{d} = \left\{\frac{3}{4}\pi C_m r^2 \frac{\delta^2 d_j^2}{d^4}\right\}^{1/3}, \qquad \textit{when } h \leq d$$

$$\frac{h}{d} = \frac{2}{3}\frac{\delta}{d} + \frac{\pi}{4} C_m r^2 \frac{d_j^2}{d^2}, \qquad \textit{when } h > d$$

where C_m is a constant and $\int u_j dA = \frac{\pi d_j}{4} U_j^2$; in other words, d_j is the diameter of a circular jet with the same volumetric flow rate, but uniform velocity distribution.

2.4.3 Jet position

The position of the jets in the streamwise direction is crucial: if the jets are placed too far upstream from the separation point, the generated structures may completely lose coherence and end up not having any effect on the flow; if they are placed too close upstream of the separation point, the structures could have too little time to effectively bring momentum to the weak boundary layer, or, in a worst-case scenario, be seen as a "wall" by the incoming boundary layer and move the separation point upstream.

The first question one should ask is how to appropriately scale distances in a separation phenomenon, in order to effectively compare different use cases; as discussed in section 2.2, separation is related to the nature of the incoming boundary layer. For this reason, two main parameters are chosen for scaling: the boundary layer thickness δ and the momentum thickness θ; for separation phenomena on airfoils, distances are also usually scaled with the chord length c.

Table 2.1 includes a summary of the streamwise distance between the actuation and separation points found in literature, scaled using the aforementioned parameters.

Source	$\Delta x/\theta$	$\Delta x/\delta$	$\Delta x/c$
Mohammed-Taifour, Floc'H, and Weiss [18]	46	4.546	N/A
	15.34	1.515	N/A
Wu et al. [37]	$56 \div 114$	$5.45 \div 11.1$	N/A
Joseph, Amandolèse, and Aider [15]	42.9	4.17	N/A
	-6.42	-0.625	N/A
Vukasinovic, Rusak, and Glezer [33]	22.9	1.7	N/A
Rice, Taylor, and Amitay [24]	N/A	N/A	-0.15 & -0.35
Abe et al. [1]	~ 0	~ 0	~ 0
Ramaswamy and Schreyer [23]	40.4	3.93	N/A
Gilarranz, Traub, and Rediniotis [9]	Variable w/ AoA	Variable w/ AoA	Actuation at 0.12

Table 2.1: Streamwise position of actuation with respect to separation point; *positive* values refer to actuation upstream of separation, *negative* values refer to actuation downstream of separation.

As table 2.1 shows, a wide range of nondimensionalized actuation positions has been used in the past; while it is safe to assume that such position plays a role in separation control effectiveness, it is still unclear whether an *optimal* streamwise position exists, and if so, what the best scaling factor for such length is.

2.4.4 Jet orientation

When discussing jets with a rectangular cross section, an important parameter to define is the *skew angle* β: it is defined as the angle the jet orifice - often referred to as *slit* - makes with the streamwise direction; in order words, it's the rotation of the jet slit around an axis normal to the wall. Figure 2.14 provides a visual representation of the skew angle.

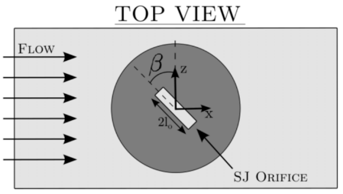

Figure 2.14: Schematic representation of a jet slit, top view, from [4].

The orientation of a jet in crossflow is an extremely important parameter: when a jet is angled, in addition to the structures presented in section 2.4.2, another streamwise-oriented vortex is formed; the phenomenology of a skewed jet in crossflow was explored in depth by Van Buren et al. [4]; what follows is a brief summary of their work.

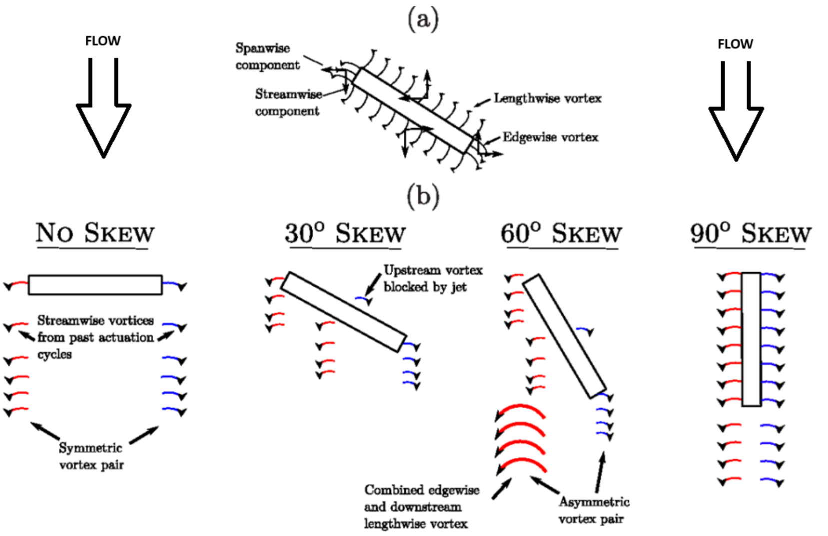

Figure 2.15: Schematic representation vortices formed around a skewed jet, from [4].

As anticipated in the previous paragraphs, a non-skewed jet slit (i.e., a slit that presents a symmetry along its streamwise-oriented centerline) features a dominant streamwise-oriented counter-rotating vortex pair; additionally, another vortex pair forms along the spanwise-oriented sides of the slit itself, with vorticity along the spanwise direction. However, this spanwise vortex pair has minimal effect farther downstream, and can be disregarded when considering flow separation control.

When the slit is skewed, such spanwise vortex pair loses its purely spanwise orientation: its windward side is blocked by the jet, while its leeward side coalesces with the streamwise vortex with same-sign vorticity; the result far downstream is an asymmetric vortex pair. A visual representation is reported in fig. 2.15.

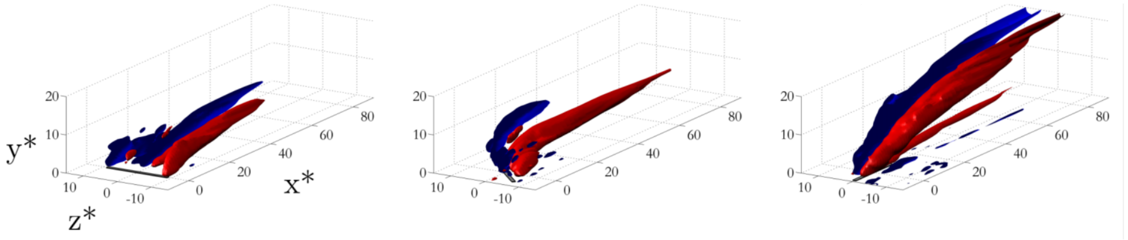

Figure 2.16: Isosurfaces of time averaged Q-criterion for skewed jet slits ($\beta = 0^o, 45^o, 90^o$), from [4].

A visualization made with the aid of the time-averaged Q-criterion (for further reading, see appendix A) is proposed in fig. 2.16: the first and third visualizations refer to spanwise and streamwise-oriented slits, respectively, and they clearly show a symmetric CVP. However, the image in the middle refers to a 45^o skewed slit, and it clearly shows the aforementioned asymmetry in the streamwise-oriented vortex pair.

Another interesting aspect regarding the $\beta = 45^o$ slits is the difference in wall-distance between the two vortices: the weak vortex is advected away from the wall to a much greater extent; it will be shown that this detail may be of great importance in the context of separation control.

However, an important question is yet to be answered: what is the optimal slit orientation for turbulent separation control? Regarding isolated actuators, $\beta = 45^o$ is found to be the optimal skew angle for near-wall momentum addition[29].

For what concerns actuator arrays, it is first crucial to observe that the best possible geometrical configuration is to have alternating slits with $+\beta$ and $-\beta$ (see sketch in fig. 2.17 for reference); in this way, the vortices generated by adjacent slits are counter-rotating, and can thus form regions of downwash, bringing high-momentum fluid closer to the wall. Due to the discussions mentioned above about the CVP's inherent asymmetry, *diverging* slits should show stronger vortices in between them, and, thus, stronger downwash.

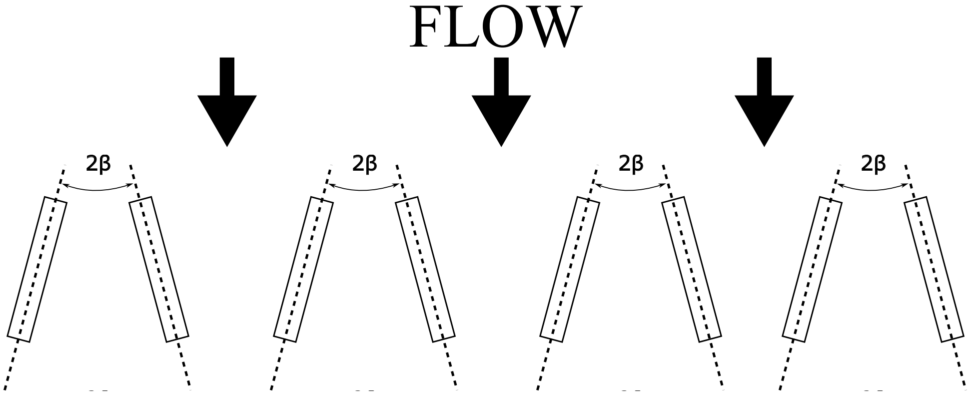

Figure 2.17: Figurative sketch of geometrical configuration of slit array.

Godard, Foucaut, and Stanislas [10] conducted an extensive optimization study, using the configuration shown in fig. 2.17 with a decelerating boundary layer, and found that $\beta = 15^o$ represented the optimal skew angle for skin friction increase.

Despite these findings, the mechanisms that correlate slit skew angle and separation control effectiveness - measured in the preservation of coherence of vortex-generated structures downstream - remain mostly unknown.

2.4.5 Unsteady actuation

As mentioned in the previous sections, one of the main advantages of active over passive control is the possibility of *modulation*, to enhance interaction with turbulent structures in the uncontrolled flow.

The unsteady nature of excitation carries out several inherent concerns, among which three are pointed out:

1. if the excitation frequency aligns with frequencies of flow structures, interaction is enhanced;
2. the experimental setup has inherent mechanical and pneumatic inertia: if the excitation frequency is too high, the jet's velocity in time will not have the desired waveform;
3. the jet's *stroke ratio*, defined below, influences the type of structure generated by the jet in crossflow.

Point 2 will be addressed in the following chapters with proper jet characterization experiments; point 3 is explored in the following paragraph.

Firstly, an important parameter needs to be defined: the *stroke ratio* L/D, where L is the jet's stroke length (the height of a column of fluid ejected in a single cycle) and D is the jet's diameter; it can be easily shown that - assuming incompressible flow - a generic time-dependent periodic jet velocity profile $U_j(t)$ with period T yields

$$\frac{L}{D} = \frac{1}{D}\int_t^{t+T} U_j(t)dt \tag{2.12}$$

Under the assumption of a square waveform with 50% duty cycle and peak velocity U_j, eq. 2.12 is simplified as

$$\frac{L}{D} = \frac{U_jT}{2D}$$

It is trivial to note that, as frequency approaches 0 (steady blowing), $L/D \to +\infty$.

Sau and Mahesh [26][27] performed DNS studies to find the optimal stroke ratio for jet penetration into crossflow; assuming a square waveform for the jet velocity in time, they identified three different flow regimes on the stroke ratio-velocity ratio (as defined in section 2.4.2) map shown in fig. 2.18.

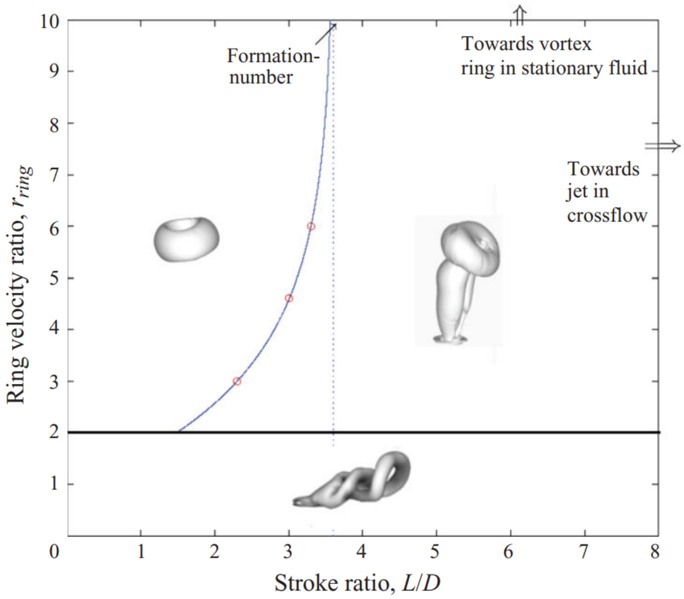

Figure 2.18: Stroke ratio-velocity ratio map, from [26]; r_{ring} is the velocity ratio as defined in section 2.4.2. In the plot, the blue, solid curve represents the formation number for jets in crossflow; the dashed vertical line represents the formation number for jets in quiescent surroundings.

The bottom region, characterized by low velocity ratios, is the one described in the third paragraph of section 2.4.2: the structures generated by the jet are a *periodic train of hairpin vortices* shed downstream; it is important to note that the agreement on a threshold velocity ratio value is not unanimous: as visible in fig. 2.18, Sau and Mahesh [26] report a value of 2, while different authors[17] report a value of 1.

For high velocity ratios (above the solid horizontal line in figure 2.18), the concept of *formation number* needs to be introduced; such number represents the value of stroke ratio that marks the transition between two different flow structures: on the left-hand side of the SR-VR map, the jet forms an annular vortex, which tilts upstream and penetrates into the crossflow, while on the right-hand side of the map, the jet forms an annular vortex followed by a *trailing column*, which corresponds to the CVP presented in the first paragraph of section 2.4.2.

2.5 Final remarks and research motivation

From what has been shown, it appears clear that little knowledge is available about the behavior of skewed jet outlets with the purpose of separation control; however, it is clear that the structures generated by a skewed jet in the presence of crossflow are fundamentally different from those generated by a streamwise one.

This thesis aims to investigate several topics:

1. can skewed jet outlets for separation control yield better results than streamwise ones? Why?
2. what is the role played by actuation frequency in the control mechanisms?
3. can the instantaneous behavior of the flow field reveal further information about the frequency-driven mechanisms?

Experimental methodology

3.1 Experiment design

3.1.1 Airfoil-like model

The airfoil-like model used for the experimental campaign is shown in fig. 3.1: it has a chord of 1366 *mm* and a total span of 1234 *mm*; it is divided into three sections:

1. a curved leading edge;
2. an extended flat middle section, to allow for a fully turbulent boundary layer to develop;
3. a curved trailing edge section, characterized, on its suction side, by a steep adverse pressure gradient to induce separation.

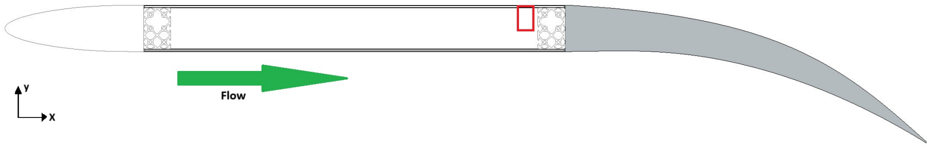

Figure 3.1: 2D section of the airfoil-like model used for the experiment. The green arrow indicates flow direction, while the red rectangle represents the actuators' position.

The model is equipped with an array of 83 pressure taps, positioned along a streamwise line on the suction side, at a spanwise location 555 *mm* from the left edge; figure 3.2 provides a representation of the spacing between two adjacent taps: the taps on the curved part, where the adverse pressure gradient is, are much closer to one another, to ensure a good spatial resolution in the pressure distribution.
Figure 3.3 shows a rendered image where the spanwise location of the tap array is highlighted; is worthy of noting that the pressure taps, with the *skewed slits* mounted (more about slits in the following sections), are located between two *convergent* slits.

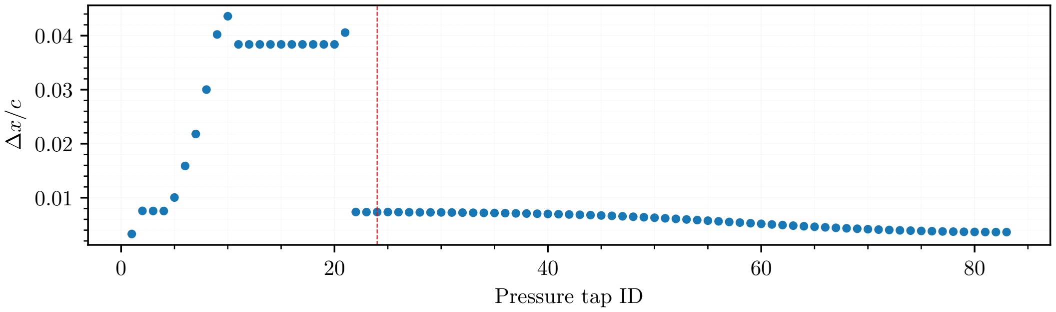

Figure 3.2: Spacing between two adjacent taps; tap IDs go in increasing order starting from the model's leading edge. the red dotted line represents the starting point of the model's curved part.

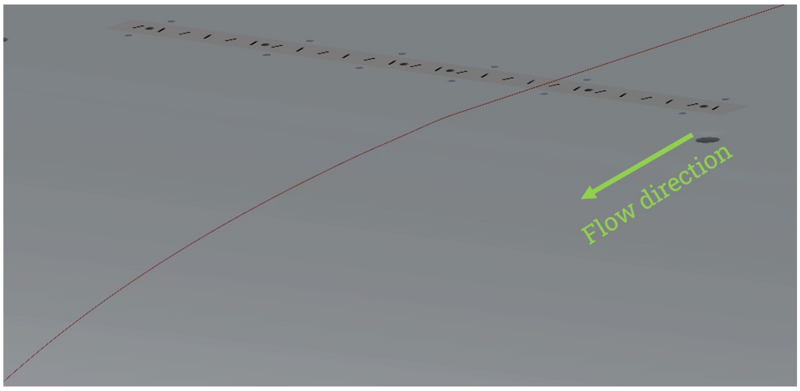

Figure 3.3: Spanwise location of pressure tap array, represented in the rendered image by the red line; the flow goes from top-right to bottom-left.

3.1.2 LTT wind tunnel

Much of the testing was conducted at TU Delft's *Low turbulence Tunnel* (LTT); it is a closed-loop subsonic wind tunnel, capable of reaching speeds up to 120 m/s, thanks to its six-bladed fan driven by a 525 kW DC motor.

Due to the large contraction ratio of 17.8, the freestream turbulence level in the test section varies from only 0.015% at 20 m/s to 0.07% at 75 m/s. The corner vanes that curve the flow in the corners of the tunnel avoiding separation are equipped with a cooling system to control the flow's properties.
The test section is octagonal, and it is 1.80 m wide, 1.25 m high and 2.60 m long.

Figure 3.4: Airfoil-like model firmly placed in the LTT's test section.

3.1.3 Actuation system

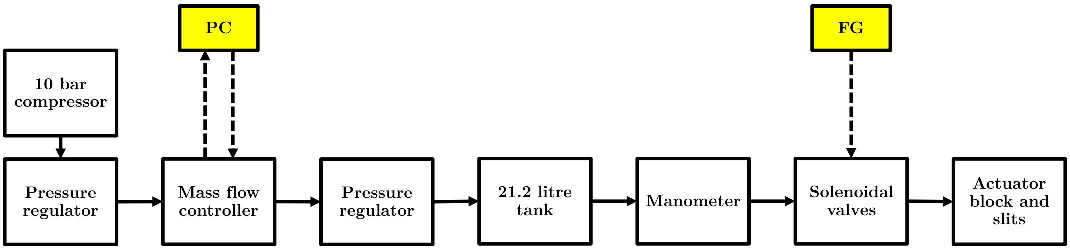

Figure 3.5: Sketched block-diagram of the actuation system.

As sketched in fig. 3.5, the actuation system is an open-loop controlled pneumatic open circuit; high-pressure air is supplied by a portable 10 *bar* compressor; the velocity of the jets is controlled by a mass flow controller, easily operated through a PC interface; the mass flow controller is also able to give real-time feedback of the mass flow passing through it. A 21.1 l tank is added to introduce some pneumatic inertia to the system.

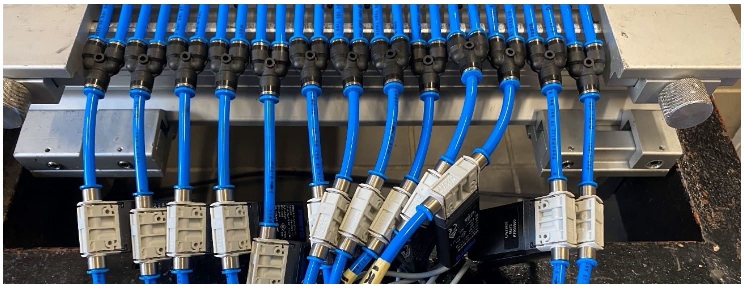

Figure 3.6: Close-up of the valves connected to the actuation block.

To control the frequency of actuation, 13 solenoidal valves are placed just upstream of the actuator block; such valves are controlled with a square-waveform voltage signal generated by a digital function generator. As shown in Fig. 3.6, each valve is connected to two slits through a split tubing connection.

Compressor

Figure 3.7: Genmac KZ 480-50 piston compressor.

As mentioned above, high-pressure air was supplied by a compressor; more specifically, the Genmac KZ 480-50 piston compressor.
The datasheet of such product specifies a peak volumetric flow rate of 480 l/min, at aspiration, and a working pressure of 10 *bar*; upon delivery, such value was tested, and the results are shown in fig. 3.8.

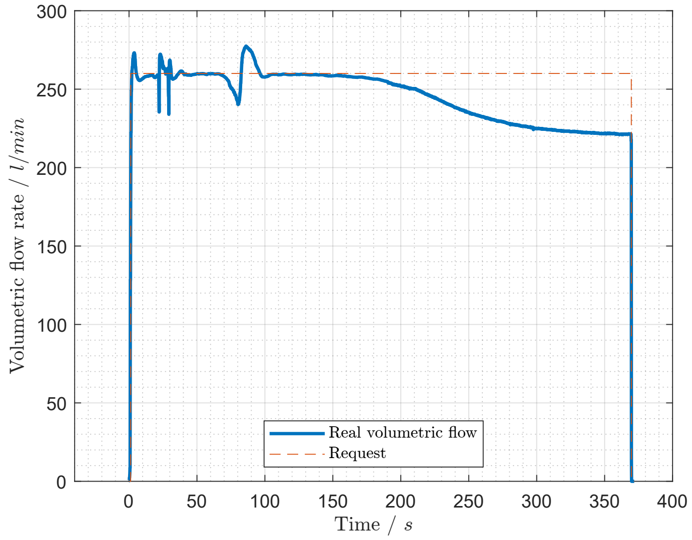

Figure 3.8: Time series of the air flow supplied by the compressor at a flow rate specified by the mass flow controller.

To assess what continuous air flow the compressor could supply, it was connected to the mass flow controller (see the paragraph below for more details about the instrument), and it was instructed to deliver 260 l/min indefinitely.
The plot in fig. 3.8 clearly shows that, apart from a few oscillations, the compressor was able to keep up with the request for approximately 4 minutes, after which the volumetric flow rate started slowly decaying.

Interpreting the plot, it can be safely assumed that initially, since the compressor tank was pressurized to 10 bar, the requested airflow could be easily supplied, but as the pressure in the tank decreased, the compressor motor could not keep up, thus showing that the value of 480 l/min declared by the manufacturer was not reliable.

Mass flow controller

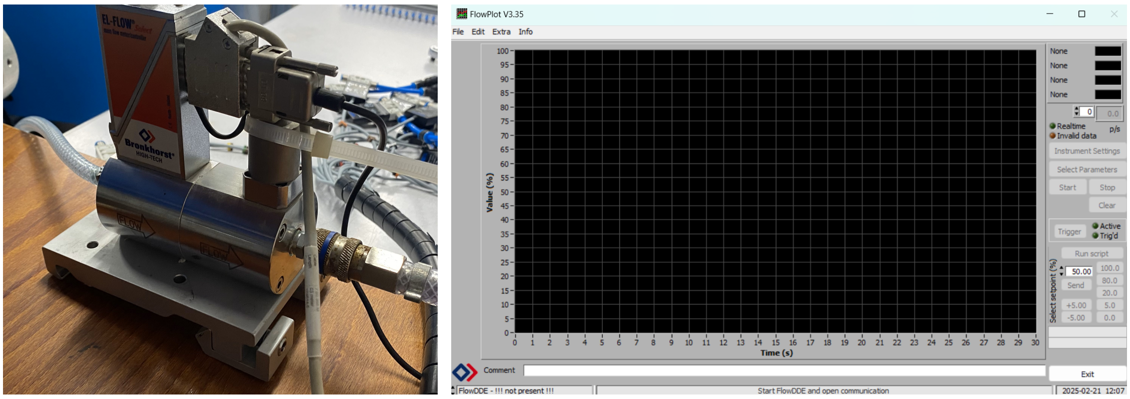

FlowDDE - !!! not present !!!

Start FlowDDE and open communication

2025-02-21 12:07

Figure 3.9: Mass flow controller Bronkhorst EL-FLOW and proprietary control software *FlowPlot*.

The mass flow controller is a Bronkhorst EL-FLOW; it has a full scale value of 260 l/min; such instrument can be operated by PC interface, with the aid of Bronkhorst's proprietary softwares *FlowDDE* and *FlowPlot*.

Other than allowing the user to control the instrument, *FlowPlot* gives a real-time feedback of the volume flow passing through the mass flow controller, in the form of a low-fidelity plot, or as a text file containing volume flow as a time series; thanks to this specific feature, a step-response test was performed.

The mass flow controller was supplied with high-pressure air, and it was instructed to deliver 0 l/min; suddenly, it was instructed to deliver its full scale value of 260 l/min. After allowing some time to let the flow stabilize, it was once again instructed to deliver 0 l/min.

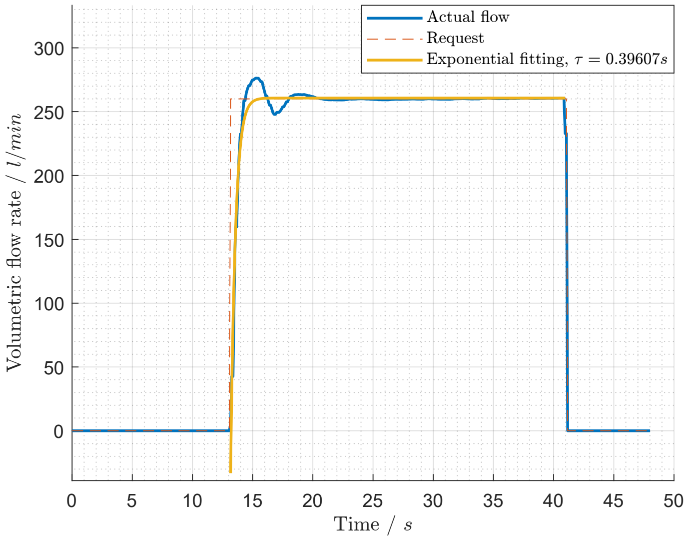

Figure 3.10: 0-100-0% step response test of the mass flow controller.

The results of such test are presented in fig. 3.10; the real flow's behavior was fitted with an exponential law, namely:

$$\dot{V}(t) = \dot{V}_{t\to\infty} + \left(\dot{V}_{t=0} - \dot{V}_{t\to\infty}\right) e^{-t/\tau} \tag{3.1}$$

where t is time, $\dot{V}$ represents the volumetric flow rate and τ is the time constant.
As visible in the figure, the time constant is equal to approximately 400 ms; after a time equal to $5\tau = 2\ s$, it can be safely assumed that the system has reached its asymptotic value with very good approximation.

Solenoidal valves

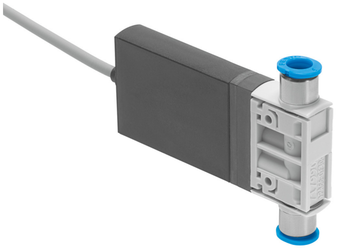

Figure 3.11: Solenoidal valve Festo MHJ10-S-2,5-QS-6-HF.

The valves used to control the actuation frequency are Festo MHJ10-S-2,5-QS-6-HF (see fig. 3.11); they are nominally-close solenoidal valves, which means that Methodology/FG and amplifierey open when a voltage between 3 V and 30 V is applied to them.
These valves are certified to deliver up to 160 l/min, at pressures between 0.5 bar and 6 bar, and the technical datasheet specifies a maximum switching frequency of 400 Hz.

Function generator

Figure 3.12: Function generator (top) and signal amplifier (bottom).

The function generator used to control the valves is a Tektronix AFG 3252; the function generator is connected to a signal amplifier, to provide the valves with enough current (see fig. 3.12).

Actuator block

The actuator block is a PLA 3D-printed assembly, which allows the flow from the Festo valves to be converted into an array of jets; as will be shown below, it is made up of three components: a *base block*, a *slit array*, and a *closing plate*.

The printer used was a Bambulab X1C; its precision was tested by printing the block shown in fig. 3.13; such manifold features 5 slits with slightly different dimensions; such dimensions, in millimeters, are engraved on the object's surface.
The dimensions of the real-life component were then compared with those imposed in the CAD model; the average deviation was measured, with the aid of a caliper, to be 0.02 *mm*, while the maximum deviation was 0.05 *mm*.

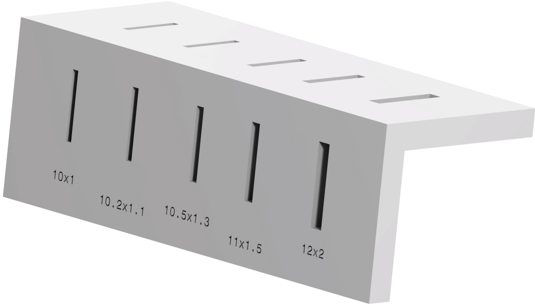

Figure 3.13: Test object used to test the 3D printer's precision.

The base block, as shown in fig. 3.14, consists of an array of 13 cavities, each corresponding to a slit and, therefore, a jet.

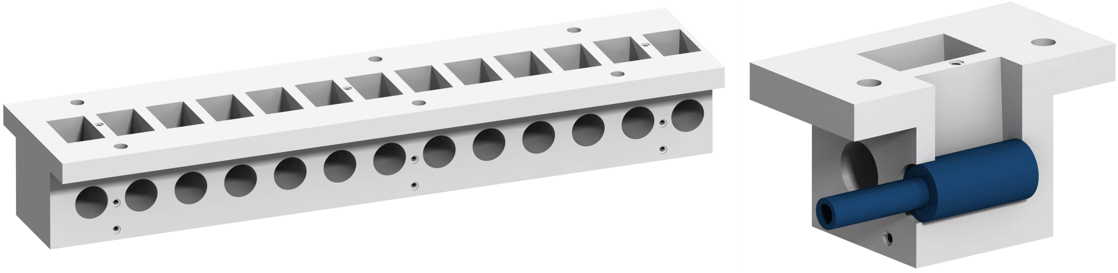

Figure 3.14: On the left, half actuator block; on the right, detail of one of the cavities with the Festo muffler silencer inserted.

Each of the cavities is shaped to allocate the corresponding nozzle system leading to a slit; the bottom end of the cavity is shaped as a half-circle to ensure fit for the Festo silencer shown on the right-hand side of fig. 3.14; such silencer is inserted to ensure cross-sectional uniformity in the jet.

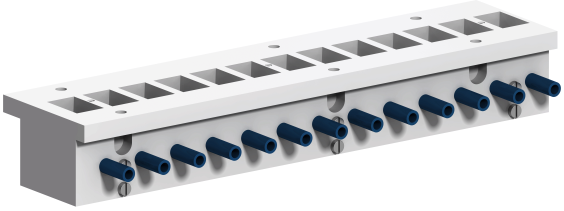

Figure 3.15: Assembled base block.

The base block is completed by a closing plate, attached through six M2 screws, designed to hold the muffler silencers in place; a depiction of the assembled base block, together with mufflers and closing plate, is shown in fig. 3.15.

(a) Streamwise slits.

(b) Skewed slits.

Figure 3.16: Array of slits in the two configurations used for the experiment.

With ease of assembly and disassembly in mind, the slit array, shown in fig. 3.16, was designed as a separate component, to allow for quick change between different configurations.
It consists of a flat top with, on which the 13 slits are engraved, and 13 extremities, which serve as nozzles to connect the base block's cavities with the slits; the cross section of such nozzle is visible in fig. 3.17.

The slits are 1 *mm* wide, 6 *mm* long and are spaced 12 *mm* between centerlines.

Figure 3.17: Cutaway view of one of the nozzles.

For the reasons discussed in paragraph 2.4.4, two configurations were selected: streamwise-oriented slits and slits skewed with a 15^o angle with respect to the streamwise direction.
Since the structures generated by streamwise and skewed slits are fundamentally different (refer to paragraphs 2.4.2 and 2.4.4 for further reading), as discussed in the previous chapter, a proper physical comparison between the two configurations is very hard to achieve; thus, it was concluded that it would be easier to go for a more practical approach: the two arrays have the same number of slits, with the same centerline spacing, and with the same cross section. In this manner, a more practical comparison can be achieved with relative ease.

Finally, the entire block assembly is mirrored around its lateral face, to achieve a 26-slit configuration and still stay within the 3D printer's maximum build volume. A depiction of the final assembled product is shown below.

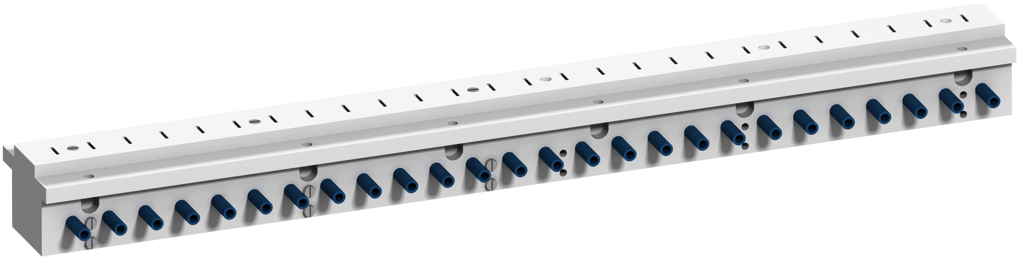

Figure 3.18: Assembled actuator block.

3.2 Hot wire anemometry (HWA)

A *hot wire anemometer* is a type of probe used to measure the module of a fluid's velocity in a certain point; it consists of a thin filament, usually made in tungsten, that is part of an electric circuit.
The probe can work in two ways:

1. *constant current*: the probe is heated up due to Joule effect, and as the airflow cools it down, it changes its resistance; an electronic device ensures that constant current flows through the probe;
2. *constant temperature*: the probe, maintained at a constant temperature, changes its resistance due to heat loss caused by forced convection from the fluid flow. This results in a potential variation across the diagonal of a Wheatstone bridge (in which the probe occupies one of the branches). A servo-amplifier responds by adjusting the current to keep the probe at a constant temperature.

The probe used for this work is operated at constant temperature; thus, what follows refers to such operating condition.

In the end, the measured voltage values are a function of the fluid velocity; finding such function is part of a process called *calibration.*

To improve accuracy, two additional parameters need to be introduced: the *offset* E_0 and the *gain* G; calling E the output voltage and E_{hw} the voltage measured at the probe:

$$E = E_0 + G \cdot E_{hw}$$

E_0 represents the voltage measured when the flow is stationary.

A physics-derived form of such function, the derivation of which is of very little relevance to this thesis, is *King's law*:

$$E^2 = A + BU^n$$

where U is velocity, and A, B, and n are constants that need to be determined through calibration. Different functions can be used, such as polynomials; more specifically, a 3rd-degree polynomial was used for hot wire calibration in this work:

$$U = a_3E^3 + a_2E^2 + a_1E + a_0$$

where the coefficients a_3, a_2, a_1 and a_0 are determined through calibration.

The hot wire probe used for this work is a Dantec P11.

3.3 Particle image velocimetry

Particle Image Velocimetry (PIV) is a non-invasive optical measurement technique used to visualize and analyze fluid flow. It works by seeding a fluid with tracer particles that follow the flow dynamics. These particles are illuminated, typically using a laser sheet, and their movement is captured in successive images using high-speed cameras. By comparing the displacement of particles between image pairs, PIV calculates velocity vectors across the flow field.

Among the possible types of PIV, two-dimensional-two-component PIV was used for this work; the laser sheet consists of a plane, and the velocity components measured are the ones that lie on such plane.

3.3.1 Laser sheet and fields of view

The position and orientation of the laser sheet are of great importance, because they determine the *field of view*, which is defined as the plane on which velocity is measured.
In the present work, the laser was set perpendicular to the wall and parallel to freestream velocity, such that the wall-normal and wall-tangent velocity components could be measured.

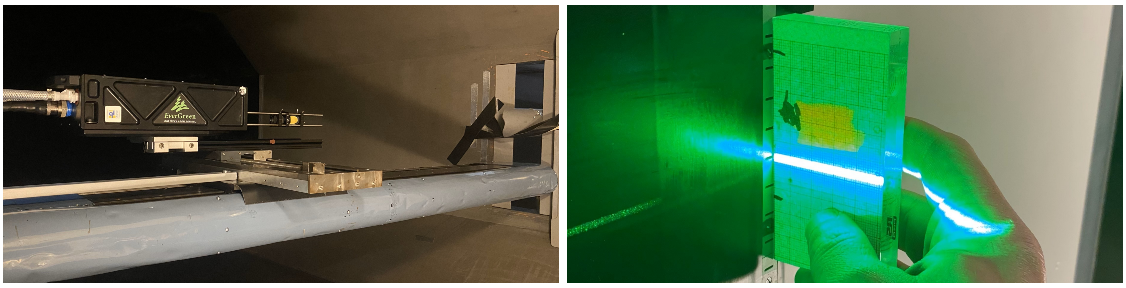

(a) Laser, together with lenses and mirrors, mounted on the traversing system described below.

(b) Visualization of the laser sheet; in the image, the laser is set at *FOV2*.

Figure 3.19

As shown in fig. 3.20. three Fields of view were chosen for the skewed slits, and only two for their streamwise counterparts; the reason behind this difference lies in what was discussed in paragraph 2.4.4: the behavior on the flow between two convergent skewed slits is expected to be different from the behavior between two divergent ones. Streamwise slits, on the other hand, are expected to show symmetry.
Hence, the three laser positions used differed on the basis of the spanwise position of the field of view:

- *FOV1*: a plane passing through the midpoint between two convergent skewed slits;
- *FOV2*: a plane passing through a slit's centerline;
- *FOV3*: a plane passing through the midpoint between two divergent skewed slits;

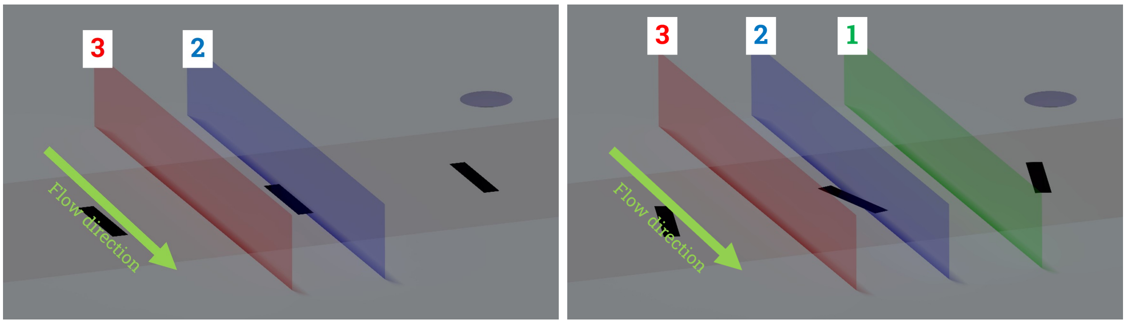

(a) Streamwise slits.

(b) Skewed slits.

Figure 3.20: Position of the three FOVs; FOV 1, 2 and 3 are depicted as green, blue and red respectively; in the figures, the flow goes from top-left to bottom-right.

Since the spacing between two adjacent slits is 12 mm, the spacing between two adjacent planes is 6 mm; a traversing system with a resolution of $\sim 25\mu m$ was used to move the laser.

3.3.2 Cameras and image processing

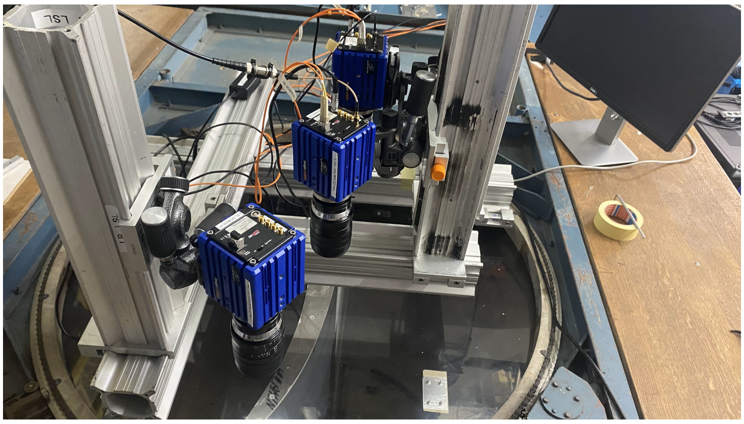

Figure 3.21

The cameras used were LaVision sCMOS 2560x2160 pixel resolution cameras equipped with Nikon 60mm lenses for all planes; To ensure a large enough field of view; three cameras were placed next to one another; the images were pre- and post-processed using LaVision's software *Davis*.

Calibration

Calibration for each field of view was performed with the aid of a custom-made calibration plate, filled with black dots spaced 9.75 mm apart, each with a diameter of 1.95 mm.

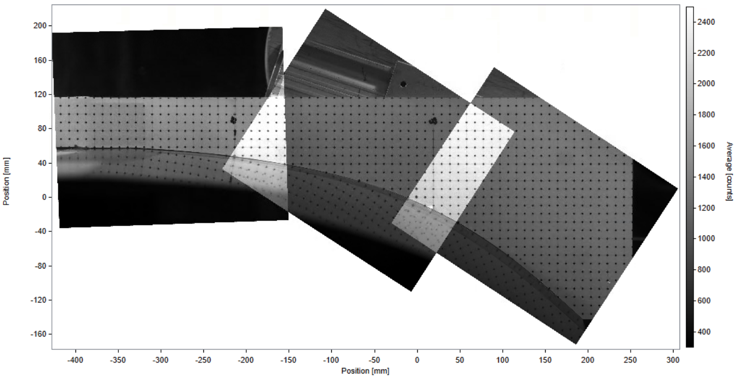

Figure 3.22

With this information, LaVision's *Davis* was able to perform image calibration, gathering the pixel/mm ratio, and constructing a *stitched* field, shown in fig. 3.22.

Image processing

The images were preprocessed to compute background subtraction and get more intense contrast between illuminated particles and black background; subsequently, PIV was performed, with a final interrogation window of $12 \times 12\ px$.

3.3.3 Post-processing

Along with the PIV frames, the q-switch (laser signal) and valve opening signals were acquired (a snippet of of one of the test cases is reported in fig. 3.23 as an example); this allowed to know *precisely* where each pair of frames (and thus, each PIV instant) was in the valve phase.

The sampling frequency was set to be $\sim 10\sqrt{2}\ Hz$; since all of the valve frequencies were multiples of 5 Hz, the ratio between the PIV sampling frequency and the actuation frequency always yielded an irrational number; in short, this meant that all the PIV samples were evenly distributed among the valve phase.

Thanks to this information, all the PIV test cases could easily be discretely phase-averaged.

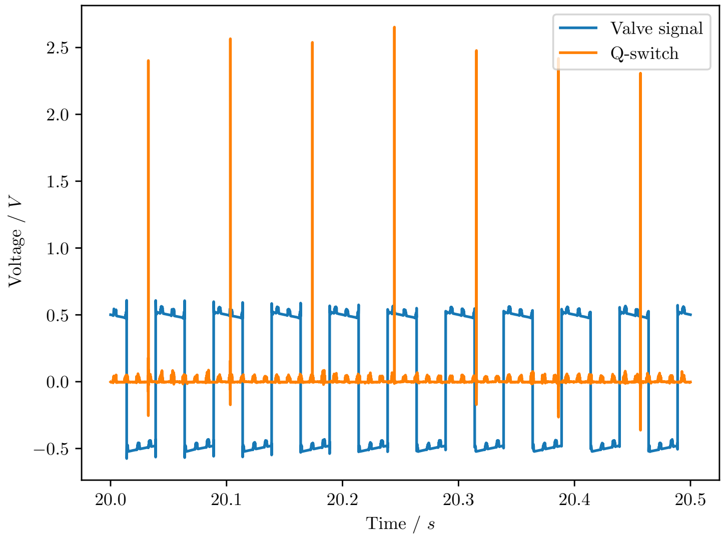

Figure 3.23: Snippet of the voltage time series, showing both the q-switch and the valve opening signals.

Discrete phase-averaging

The process of phase-averaging consists of constructing the *average* period of a periodic time series. When the sampling frequency f_s is smaller than the phenomenon frequency f, the easiest way to proceed is to divide the phase into a finite number of sections called *bins*; in this way, each acquired sample will inevitably fall into one of the bins: all of the samples belonging to the same bins can then be averaged, and the average period can be constructed.
Mathematically, this can be written as:

$$\bar{U}(n) = \frac{1}{K}\sum_{i}^{K} U_i(MT + \phi_i), \qquad n/N < \frac{\phi_i}{2\pi} < (n+1)/N \tag{3.2}$$

where $\bar{U}$ is the phase-averaged field, n is the $n-th$ bin, K is the total number of samples belonging to the $n-th$ bin, U_i is the $i-th$ acquired sample, M is an integer, T is the phenomenon's period, ϕ_i is U_i's phase and N is the total number of bins.

Actuation system characterization

To assess the performance of the actuation system, several tests were performed in *quiescent surroundings*, that is, in the absence of crossflow.

4.1 Assessment of non-uniformity

One of the potential problems was inter-jet non-uniformity: slight geometric imperfections in the system can possibly lead to having jets with different peak velocities across the array; hence, a first test was conducted on both slit configurations, the details of which are discussed below.

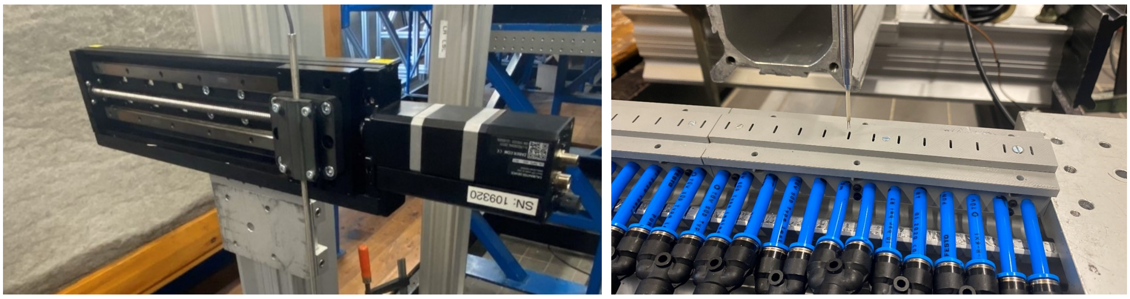

Figure 4.1: On the left: Zaber traversing system; on the right: P11 hot wire probe placed just above the slit array.

The setup is portrayed in fig. 4.1: a Dantec P11 hot wire probe was mounted on a Zaber traversing system, controlled through a PC interface; the probe was then placed just above the slit array and moved across at a rate of 3 mm/s, as steady jets were blowing out of the slits at a flow rate specified by the mass flow controller.
The assess the uniformity across the array, a perfomance paramter is introduced:

$$\frac{\max_i U(i) - \min_i U(i)}{\frac{1}{N}\sum_1^N U(i)} \tag{4.1}$$

where N is the total number of slits examined, i is the $i-th$ slits and $U(i)$ is the peak velocity corresponding to the $i-th$ jet; formula 4.1 represents the maximum deviation between velocities scaled with respect to the average jet velocity.

Tests were performed at five different volume flow rates, each corresponding to a full scale value of the mass flow controller; a summary is presented in table 4.1.

$\dot{V}$ / l/min	$\%_{FS}$	$U_{j,\ expected}$ / m/s	VR, $U_\infty = 12.5$ m/s
23.4	9	2.5	0.2
70.2	27	7.5	0.6
140.4	54	15	1.2
187.2	72	20	1.6
260	100	27.5	2.2

Table 4.1

Results are presented below; for shortness, only results from two of the five velocity ratios are reported. For complete results, see appendix B.

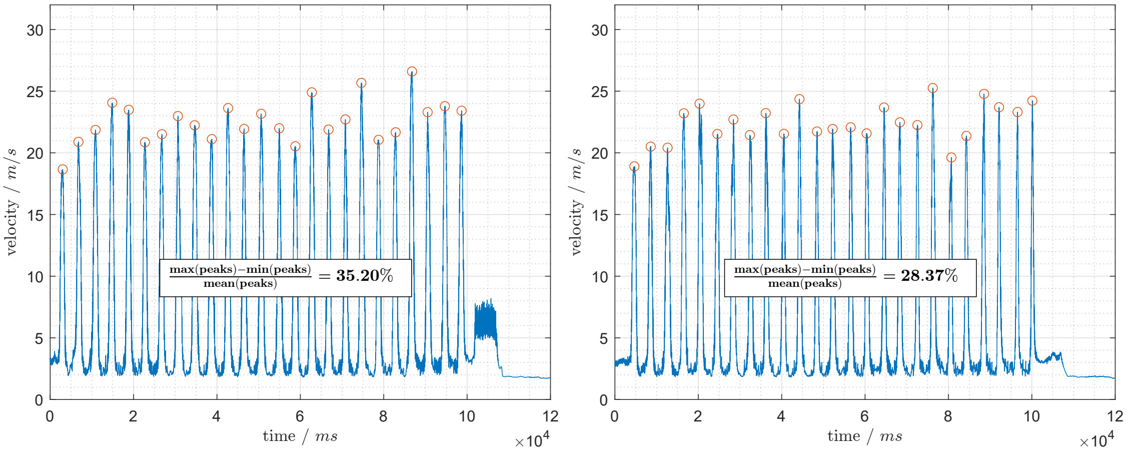

(a) Streamwise slits.

(b) Skewed slits.

Figure 4.2: Mass flow controller set at 54% of full scale value.

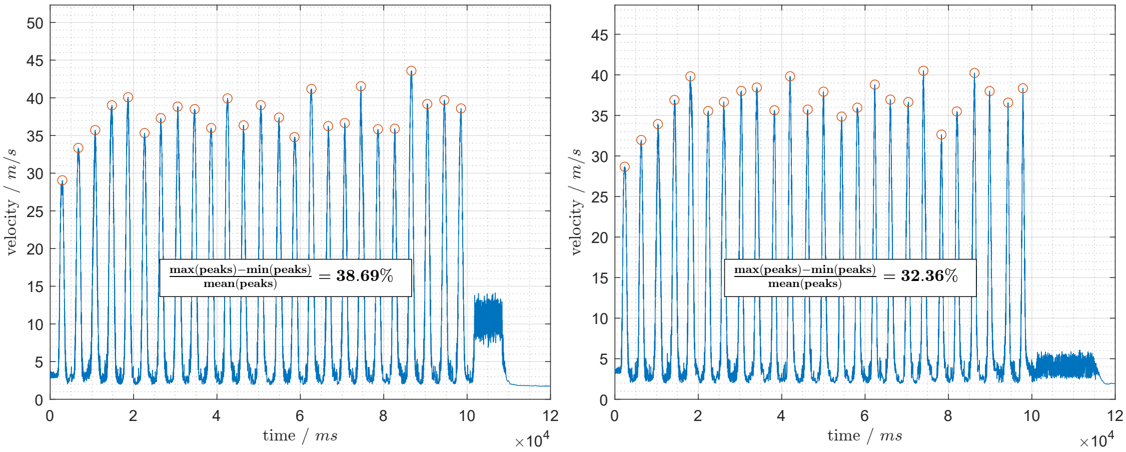

(a) Streamwise slits.

(b) Skewed slits.

Figure 4.3: Mass flow controller set at 100% of full scale value.

Figures 4.2 and 4.3 show a relative deviation between 28% and 38% for both slit configurations; to estabilish where in the system the source of this deviation lied, another test was performed: observing figure 4.3, one can notice a big difference between peaks 1-2 and peaks 5-6, which correspond to the first and third valves, respectively; hence, to rule out any influence on the tubing system upstream of the block as a source of non-uniformity, the two valves were switched. Results of such test are presented below.

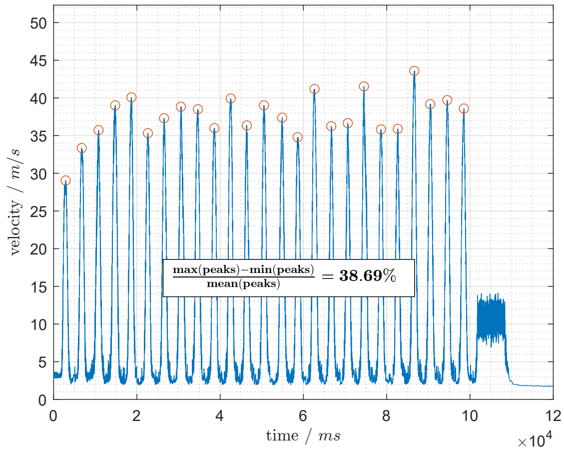

(a) Benchmark test, $\dot{V} = 260\ l/min$.

(b) Switch between first and third valve, $\dot{V} = 260\ l/min$.

Figure 4.4: Comparison between benchmark case and switch between first and third valve; mass flow controller set to 100% of full scale value.

Figure 4.4 shows no clear switch between peaks 1-2 and 5-6; thus, it was concluded that the source of the non-uniformity lies somewhere in the block, rather than the tubing system upstream.

The easiest part of the block to test was the slit array itself; in fact, with two configurations tested, the easiest way to assess whether imperfections in the slit array could be a source of peak-to-peak heterogeneity, was to simply compare data from the two configurations; for this purpose, another parameter is introduced:

$$RD(N) = \frac{|U_{j,streamwise}(N) - U_{j,skewed}(N)|}{0.5 \cdot [U_{j,streamwise}(N) + U_{j,skewed}(N)]} \tag{4.2}$$

where N represents the $N-th$ slit/jet.
Results are presented below; once again, only two of the five plots are included - for complete results, refer to appendix B.

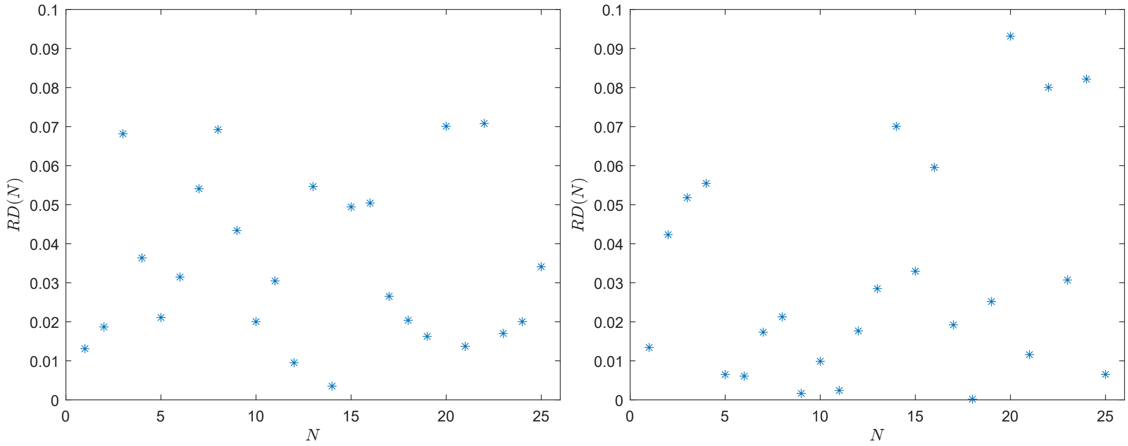

(a) Mass flow controller set to 54% of full scale value.

(b) Mass flow controller set to 100% of full scale value.

Figure 4.5: Comparison between streamwise and skewed slits, evaluated using eq. 4.2.

Figure 4.5 points out how the relative difference between the two configurations is, for most slits, within 5%, and in any case, always below 10%. Thus, it can be concluded with good reason that the slit array is not one of the causes leading to inter-jet non-uniformity.

Figure 4.6: Festo muffler silencer.

Among the components in the block, the one with the least repeatable features were without a doubt the Festo Muffler silencers; as shown in fig. 4.6, they are made of a white, porous material, and they are associated with a substantial pressure drop in a relatively confined space.

Since the mufflers were a component over which the author of this thesis had no control whatsoever, and at the time of characterization there was no time to re-think the whole block assembly, it was decided to accept the inter-jet non-uniformity as it was.

4.2 Velocity time series

In order to evaluate integral quantities, such as the total momentum flux over a period, or the stroke ratio of a pulsed jet, another set of tests was performed: the hot wire probe was held stationary over one of the cavities for a total acquisition time of 30 s, as pulsed blowing was operated. A summary of all the tests performed is reported in table 4.2.

$\%_{FS,\ mass\ flow\ controller}$	Frequencies tested / Hz
11.3	1, 30, 50, 100, 200
22.5	30, 40, 50
27	30, 40, 50
31.5	30, 40, 50
49.5	1, 40, 100, 200

Table 4.2

For the reasons discussed in the previous section, it was deemed unnecessary to test both slit configurations, since they would most likely have given similar results; thus, only the streamwise slits were tested.

4.3 Raw velocity time series and phase averaging

Results for one of the test cases are presented below; for complete results, see appendix C.

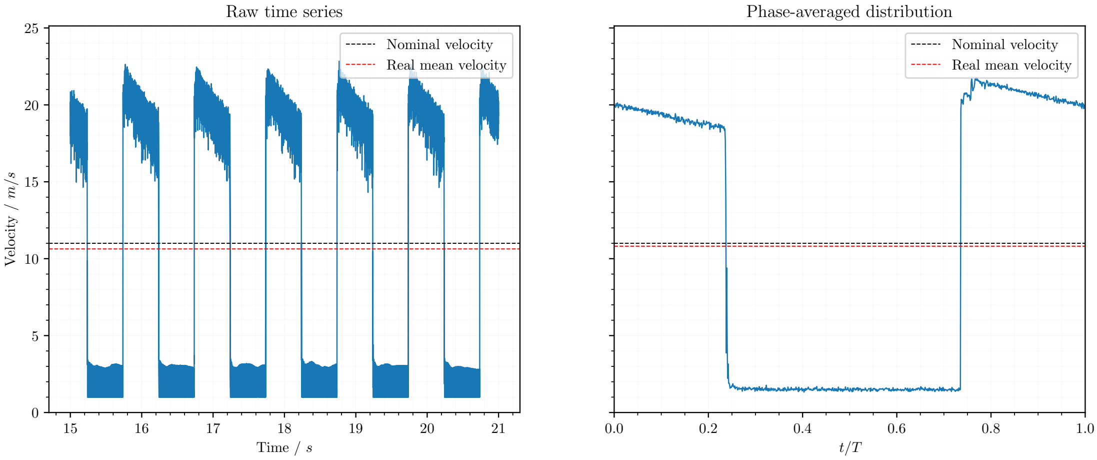

Figure 4.7: Mass flow controller set to 49.5% of full scale, valves operated at $f = 1\ Hz$; the black dotted line represents the expected mean velocity, i.e. the velocity calculated based on the mass flow controller's setpoint; the red dotted line represents the actual mean velocity.

The plot on the left in fig. 4.7, which shows a portion of the acquired raw velocity time series, exposes two main problems:

1. velocity seems to clip at values below 1 m/s;
2. the signal is very noisy.

The first problem is most likely related to the incorrect setting of the offset and gain parameters prior to hot wire calibration; it isn't a highly relevant issue, but it means that the measurements are not reliable for low velocities.
The second problem can be easily solved by performing phase-averaging on the raw signal to obtain an *average period*; the result of such operation is shown in the plot on the right of fig. 4.7: the signal looks much smoother, and it can clearly be recognized when the valve was closed (from $t/T \sim 0.18$ to $t/T \sim 0.68$) and when it was opened.
Another observable behavior is the downward trend in the velocity signal when the valve is opened: this is most likely due to pressure building up in the 21.2 l tank when the valve is closed; as the valve opens, the jet velocity *overshoots*, and the mass flow controller progressively limits the mass flow to comply with the correct mass flow requested.

The velocity distribution shown in fig. 4.7 has a general *good* look, meaning that the velocity signal behaves as expected; however, not all velocity distributions recorded show such *good* behavior.

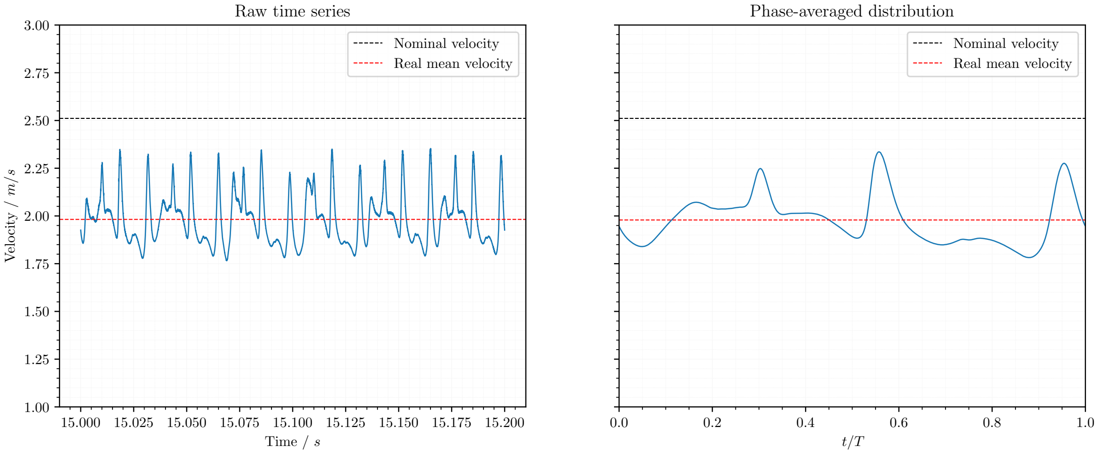

Figure 4.8: Mass flow controller set to 11.3% of full scale, valves operated at $f = 30\ Hz$.

Figure 4.8 illustrates one of the problematic test cases: the velocity time series exhibits seemingly random fluctuations, suggesting that the valve may not have been fully opening or closing as intended. This irregular behavior was hypothesized to stem from limitations in the control method—specifically, the function generator used in the system may not have been capable of supplying adequate current. At certain combinations of actuation frequency and jet velocity, this insufficiency could have led to improper valve operation.

To address this issue, the decision was made to discontinue the use of the function generator. Instead, a Simulink-based interface — developed in the context of a separate research project — was adopted to control the valves with greater reliability.

Separation control in wind tunnel conditions

Following characterization, tests were conducted in wind tunnel conditions; to assess the performance of the control methods, both pressure tap and PIV data was acquired.
This chapter aims to explore and analyze such data.

5.1 Pressure results

As discussed in paragraph 3.1.1, pressure data was acquired through a streamwise array of 83 static pressure taps; of those, 59 were positioned downstream of the actuator block, i.e. at $x/c > 0.63$, given the model's chord length c. Data from these pressure taps was used to evaluate the *effectiveness* of separation control: a metric to measure pressure recovery over the curved part of the model was introduced; since separation leads to an abrupt increase in pressure, a non-separated surface has a generally lower c_p: thus, a negative value of the metric represents a greater pressure recovery, and thus, greater control effectiveness:

$$\int_{0.63}^{1} \left[c_{p,forced}(x/c) - c_{p,unforced}(x/c)\right] \; d(x/c) \tag{5.1}$$

where $c_{p,forced}$ and $c_{p,unforced}$ refer to *actuated* and *non-actuated* pressure coefficients on the *suction* side of the model, calculated using a time-averaged value of static pressure over a time of 10 s.

Due to the nature of the experiment, one test case can be fully defined by 4 parameters:

1. Slit geometrical configuration: either *streamwise* or *skewed*;
2. Actuation frequency, f
3. Jet velocity ratio, VR
4. Tunnel freestream velocity, U_∞

Two different types of plots are presented below: *velocity ratio sweeps* at constant f, where the dependency on jet velocity ratio is explored, and *actuation frequency sweeps* at constant VR, where the dependency on actuation frequency is explored.

5.1.1 VR sweep, $U_\infty = 20\ m/s$, $f = 40\ Hz$, streamwise slits

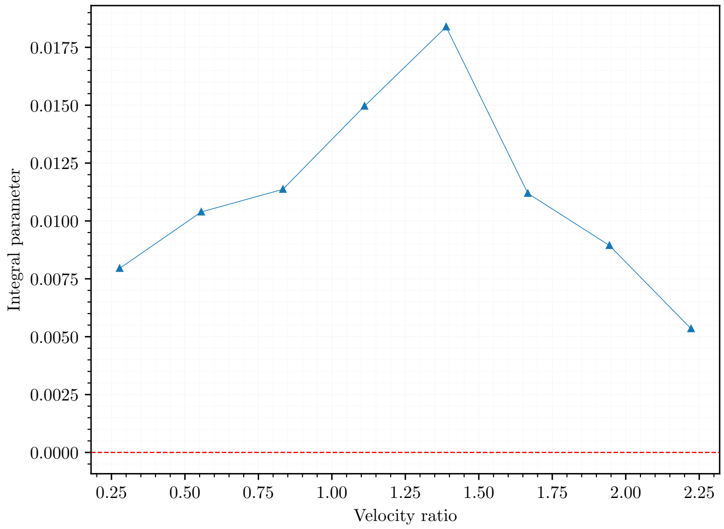

Figure 5.1: Integral parameter from eq. 5.1 as a function of velocity ratio; the red dotted line represents the upper limit for a "working" test case.

The frequency of 40 Hz was chosen because, according to past experiments (as shown in fig. 5.2), it was shown to be the *optimal* frequency for separation control at 20 m/s; in any case, this value is not of high relevance, as frequency sweeps will be presented as well.

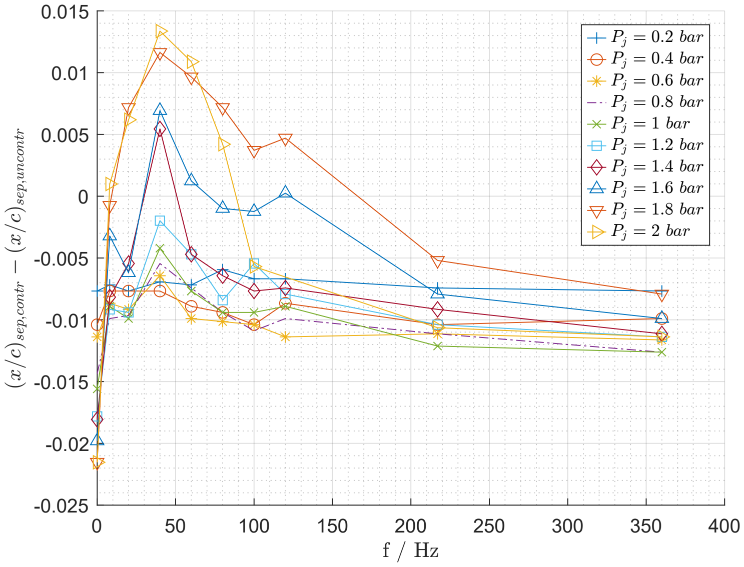

Figure 5.2: Results from a past experimental campaign conducted on the same wing-like model; the plot depicts the separation point translation for several *tank pressures* (in this context, tank pressure is relatex to jet velocity ratio). A positive value indicates a downstream movement of the separation point.

The curve shown in fig. 5.1 appears to exhibit two key aspects: after an initial peak for $VR \sim 1.4$, the integral metric shows a monotonic descent with VR, and the highest velocity ratio tested, ~ 2.25 is not sufficient to reach a negative value of the integral metric, meaning that the control was not effective for any of the cases tested.

It seems clear that the only way to make the control method effective at the desired frequency is to increase the jet velocity ratio; however, as discussed in section 3.1.3, the mass flow control is able to provide a maximum volumetric flow of 260 l/min. Given a total slit cross-sectional area of 156 mm^2, the maximum jet outlet velocity achievable is $\sim 27.8\ m/s$; for a freestream velocity of 20 m/s and valves operating at 50% duty cycle, this yields a maximum velocity ratio of ~ 2.78.

Thus, it was determined that the only way to proceed was to keep the same mass flow controller settings, and instead decrease freestream velocity.

5.1.2 VR sweep, $U_\infty = 10\ m/s$, $f = 20\ Hz$, streamwise slits

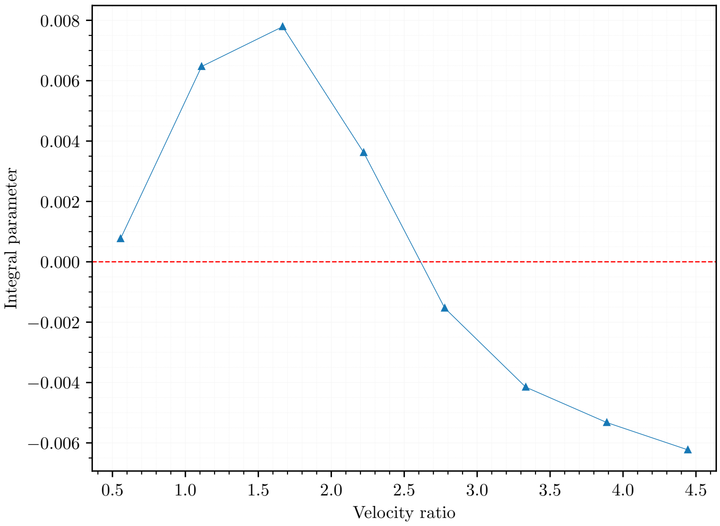

Figure 5.3: Integral parameter from eq. 5.1 as a function of velocity ratio; the red dotted line represents the upper limit for an effectively controlled test case.

Fig. 5.3 depicts the VR sweep conducted at $U_\infty = 10\ m/s$; in order to achieve a proper comparison with the test cases presented in fig. 5.1, the actuation frequency was set to 20 Hz, due to the fact that the Strouhal number is proportional to the ratio between frequency and velocity.

The monotonic descent with VR appears to show itself once again; as predicted, increasing the velocity ratio reveals that certain combinations of the experiment's parameters enable greater pressure recovery. This confirms that the desired separation control effect is indeed achievable.

Having acquired this knowledge, it is now possible to explore the effect of frequency on separation control; for the following frequency sweeps, a velocity ratio of 3.33 was chosen, as fig. 5.3 shows it is a possible working point for $f = 20\ Hz$.

5.1.3 Actuation frequency sweep, $U_\infty = 10\ m/s$, $VR = 3.33$

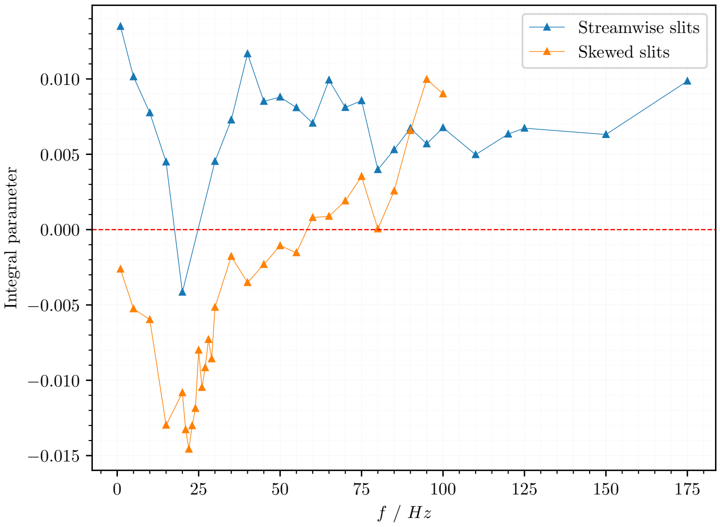

Figure 5.4: Integral parameter from eq. 5.1 as a function of actuation frequency; the red dotted line represents the upper limit for a "working" test case.

Preliminary investigations conducted in the previous paragraphs show a possible working point for streamwise slits; bearing this knowledge, a first comparison between different geometrical configurations was now possible.

Figure 5.4 shows the frequency sweep operated at $VR = 3.33$ for both slit geometrical configurations; it immediately appear evident that they show a similar trend, with on offset on the y-axis. In simpler words, the optimal frequency is $\sim 20\ Hz$ for both configurations, but the skewed slits offer a wider range of *working* frequencies, and the pressure metric's value, given a combination of f and VR is generally lower.
Unfortunately, due to the lack of boundary layer data, proper non-dimensionalization is not possible; a comparison between such frequency and the values found in literature cannot be operated.

5.1.4 Final considerations

In conclusion, pressure data were able to reveal a few key aspects:

- in many instances, separation control seems to have an undesired effect: the integral metric shows a worse pressure recovery when compared to the uncontrolled case;
- increasing VR seems to favor pressure recovery; in particular, it was observed that the maximum freestream velocity for which a desirable effect can be appreciated is $10\ m/s$: for this reason, all the PIV runs were made at this velocity;
- skewed slits seem to be able to favor a stronger pressure recovery, and for a wider range of actuation frequency, compared to their streamwise counterparts.

There are two main questions that remain unanswered:

1. is the pressure recovery shown by the pressure metric correlated to separation delay?
2. are the results shown by pressure data two-dimensional? In other words, did the flow change its behavior at one specific spanwise location, or did a global change occur?

To answer these questions, PIV results are presented below.

5.2 Time-averaged PIV results

5.2.1 Streamfunction and separation line

Given a two-dimensional, incompressible velocity field in the $(x,\ y)$ plane, the streamfunction ψ is defined as a function which yields:

$$u = \frac{\partial \psi}{\partial y} \qquad v = -\frac{\partial \psi}{\partial x} \tag{5.2}$$

ψ is an *integral* function; as such, its absolute value is arbitrary, and infinite equivalent streamfunctions can be built, which all differ by a constant.

The *iso-value* lines of ψ represent lines across which there is zero-net volume flux; in other words, the iso-value lines of ψ represent *streamlines*, the paths fluid particles follow as they move across the domain; for this reason, if the streamfunction is defined as zero at the wall, all points in the internal domain with $\psi = 0$ represent the path a fluid particle follows once it detaches from the wall. In other words, The line with $\psi = 0$ is the *separation line*, and it represents the upper limit of the recirculation bubble. An example of a streamfunction field is depicted below.

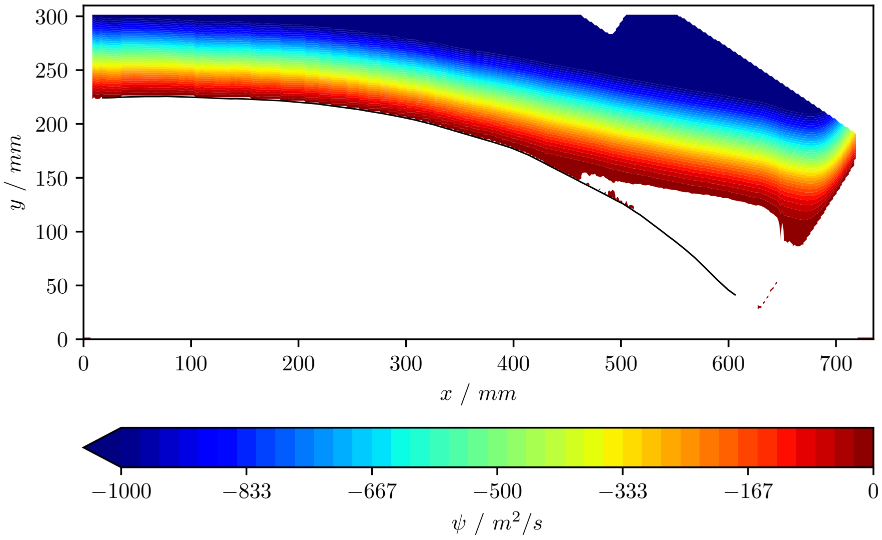

Figure 5.5: Contour representing the streamfunction ψ for FOV2 in the uncontrolled case at $U_\infty = 10\ m/s$; the contour is clipped above zero.

5.2.2 Unforced field

For what concerns the unforced vector field, results from the three fields of view are similar; for this reason, only results from FOV3 are reported. For results from FOV1 and FOV2, see appendix D.

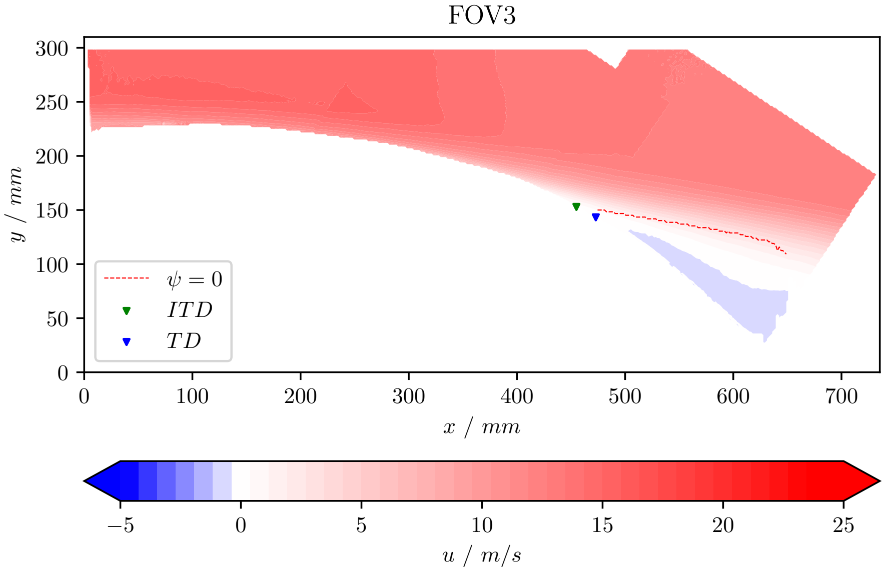

Figure 5.6: Contour representing the x velocity component for FOV3.

Figure 5.6 depicts the x component of the velocity in the unforced field for $U_\infty = 10\ m/s$; *ITD* and *TD* are defined as in section 2.2, while the red dotted line represents the separation line as described in section 5.2.1.

The unforced field, which shows a clear and evident pressure-induced separation, will serve as the *baseline* for the following discussion; specifically, the control method will generally be considered *effective* if *ITD* and *TD* are shifted downstream (in the positive x direction), and/or if the separation line moves closer to the wall (towards the negative y direction).

5.2.3 Forced field

As previously discussed, the three fields of view represent radically different flow conditions in the forced field; for this reason, they will all be presented individually for each of the cases tested.

Skewed slits, $U_\infty = 10\ m/s$**,** $VR = 3.33$**,** $f = 20\ Hz$

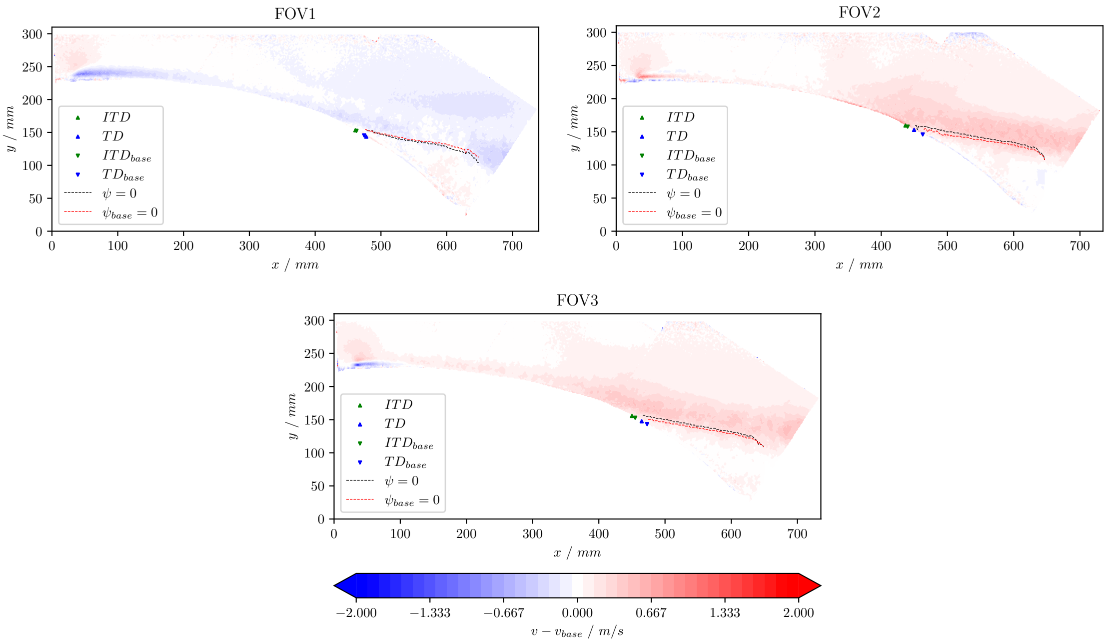

Figure 5.7: Contour representing the difference between y velocity of the forced case ($U_\infty = 10\ m/s$, $VR = 3.33$, $f = 20\ Hz$, skewed slits) and y velocity of the unforced case; all three FOVs are reported.

Figure 5.7 depicts the difference in *vertical* (along the y axis) velocity between the forced and unforced case; near $x = 40\ mm$, where the actuators are positioned, FOV2 shows *upwash*, as expected, since the jets induce a positive vertical velocity, while FOV2 and FOV3 show *downwash*, again, as expected, since the vortices generated induce a negative vertical velocity.

With figure 5.4 as a reference, it seems like $f = 20\ Hz$, $VR = 3.33$ is one of the test cases where separation should be delayed; however, this fact does not appear evident in the PIV fields. FOV1 shows how the separation point is moved slightly upstream, but also how the $\psi = 0$ line is shifted closer to the wall; FOV2 and FOV3, on the other hand, display that separation is *clearly* favored.
This difference could be related to the fact that the blue cloud , associated to downwash, located near the actuators is far bigger in FOV1, but also a bit farther from the wall; this can potentially bring high-momentum fluid from the freestream and energize the boundary layer, while in FOV3, the downwash region may not be extended far enough to reach outside of the low energy fluid which resides close to the wall.
This result may come as a surprise, following the discussion in section 2.4.4; however, it is worth noting that section 2.4.4 does not specifically expand on the extent of *vortex penetration* into the boundary layer, but it does mention how the *weak* vortex (the one in FOV1) is advected farther from the wall compared to the *strong* one (FOV3). It may just be that the streamwise vortex

generated in FOV3 is more intense, but it simply does not penetrate far enough into the upper layers of the BL.

All of this suggests that the flow field is much more three-dimensional than anticipated, even far downstream of the actuators; this point is even more evident in fig. 5.8, which shows the horizontal velocity difference contour: in the shear layer, around the $\psi = 0$ line, the flow is accelerated with respect to the baseline in FOV1, but it's decelerated in FOV2 and FOV3; this could suggest that the structures generated by the pulsed jets persist and stay coherent far downstream of their starting points.

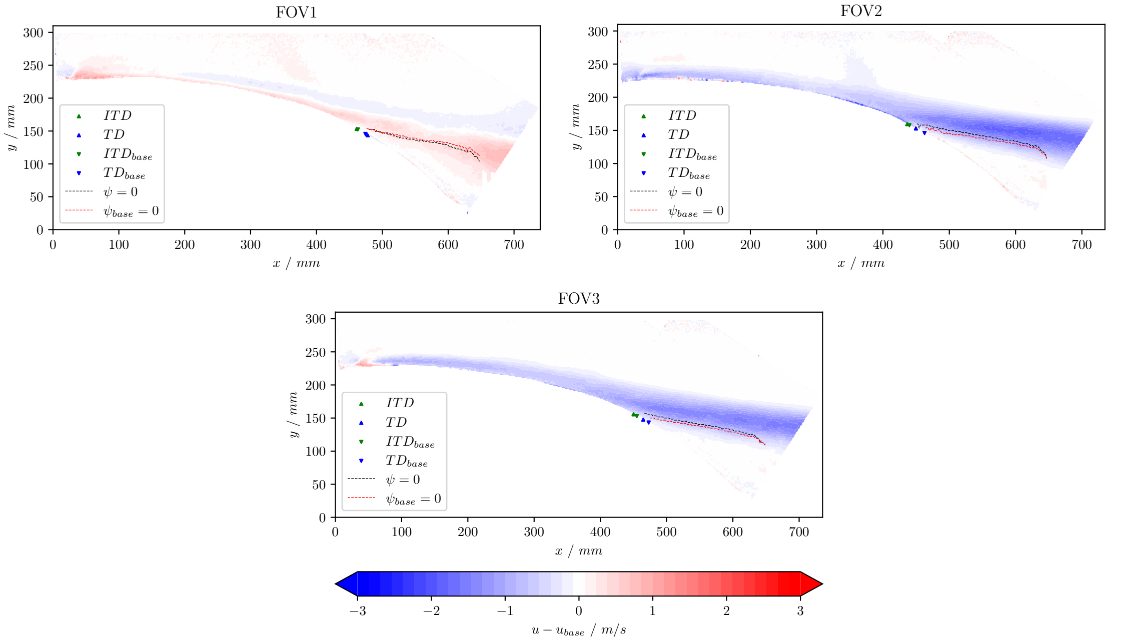

Figure 5.8: Contour representing the difference between x velocity of the forced case ($U_\infty = 10\ m/s$, $VR = 3.33$, $f = 20\ Hz$, skewed slits) and x velocity of the unforced case; all three FOVs are reported.

Streamwise slits, $U_\infty = 10\ m/s$**,** $VR = 3.33$**,** $f = 20\ Hz$

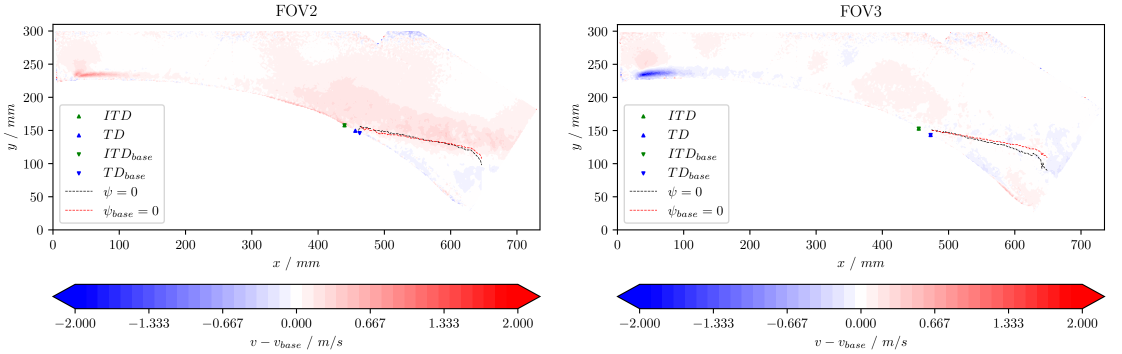

Figure 5.9: Contour representing the difference between y velocity of the forced case ($U_\infty = 10\ m/s$, $VR = 3.33$, $f = 20\ Hz$, streamwise slits) and y velocity of the unforced case; both FOVs are reported.

The features described in the previous section manifest themselves once again in figure 5.9: FOV2, the field of view passing through a slit, exhibits upwash near the actuators, while FOV3 shows the downwash associated to streamwise vortices.

ITD overlaps with ITD_{base} in both fields of view, while TD moves downstream with respect to the baseline in FOV2, while TD and TD_{base} overlap in FOV3; the separation line, on the other hand, barely moves in FOV2, while it has a certain *concavity* in FOV3, meaning that the separation bubble, with respect to the baseline, shrinks towards the trailing edge, almost as if reattachment is somewhat favored once again.

Skewed and streamwise slits, $U_\infty = 10\ m/s$, $VR = 3.33$, $f = 5\ Hz$

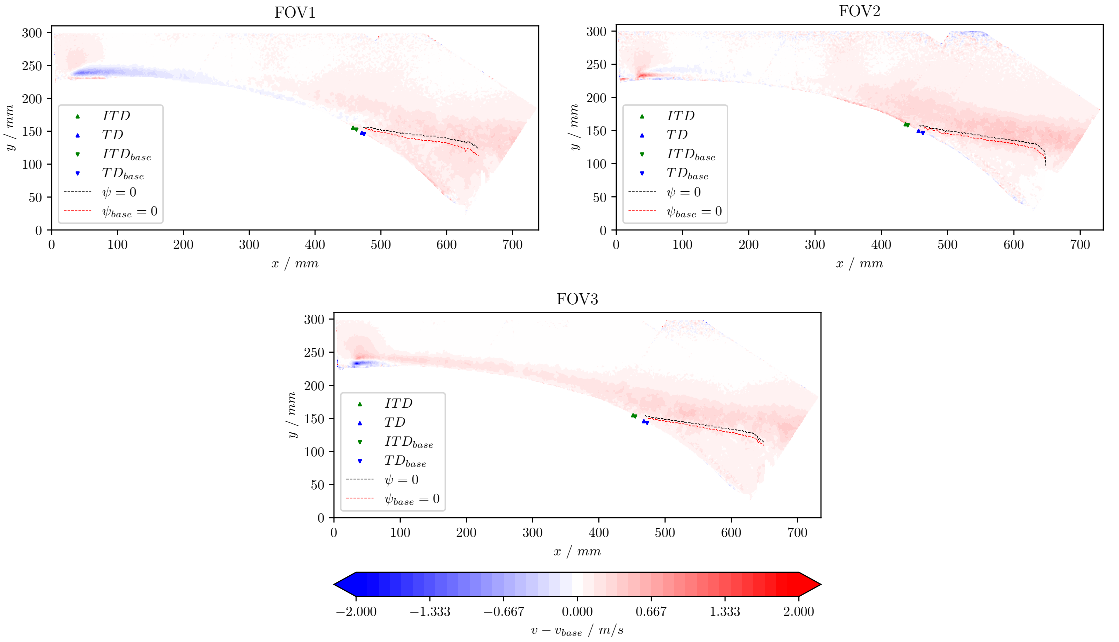

Figure 5.10: Contour representing the difference between y velocity of the forced case ($U_\infty = 10\ m/s$, $VR = 3.33$, $f = 5\ Hz$, skewed slits) and y velocity of the unforced case; all three FOVs are reported.

Figure 5.10 represents the PIV counterpart of one of the test cases performing poorly according to figure 5.4; the PIV fields seem to confirm poor performance: the separation line is moved farther from the wall in all three FOVs, and figure 5.11 shows a clear x velocity decrease.

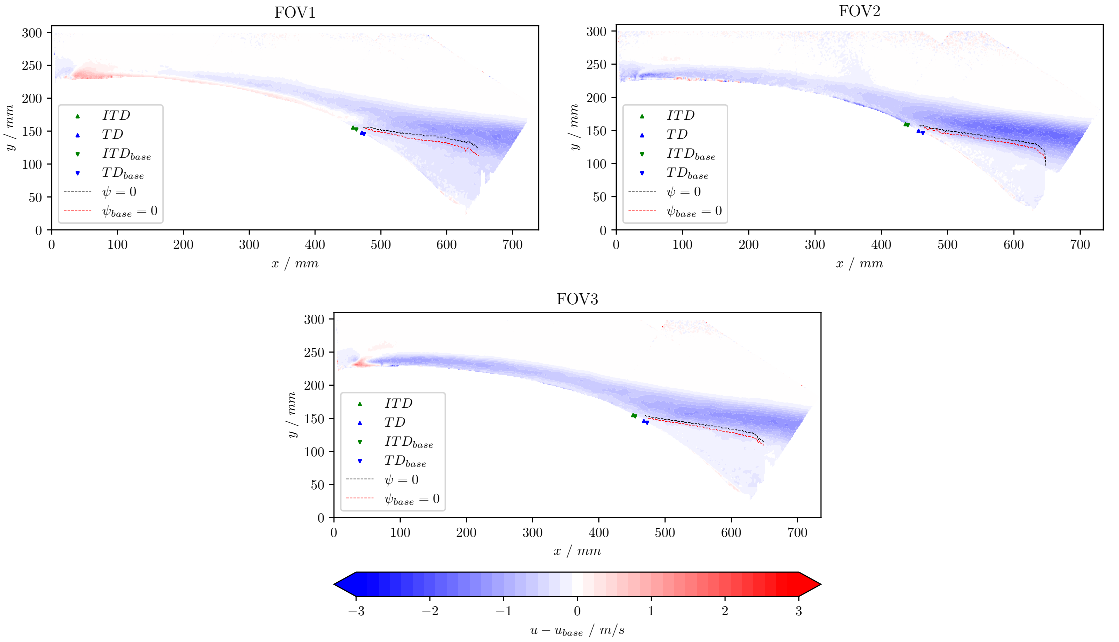

Figure 5.11: Contour representing the difference between x velocity of the forced case ($U_\infty = 10\ m/s$, $VR = 3.33$, $f = 5\ Hz$, skewed slits) and x velocity of the unforced case; all three FOVs are reported.

The trend is also confirmed - and is perhaps even more evident - for streamwise slits: figure 5.12 shows that both ITD and TD are shifted upstream by the actuation in both fields of view, and the presence of a *blue* cloud confirms that the flow is generally slower, leading to lesser pressure recovery.

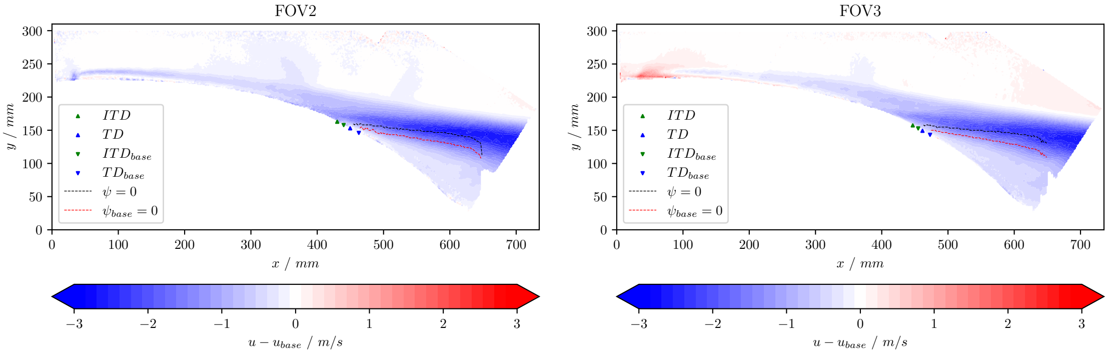

Figure 5.12: Contour representing the difference between x velocity of the forced case ($U_\infty = 10\ m/s$, $VR = 3.33$, $f = 5\ Hz$, streamwise slits) and x velocity of the unforced case; both FOVs are reported.

Streamwise slits, $U_\infty = 10\ m/s$**,** $VR = 3.33$**,** $f = 80\ Hz$

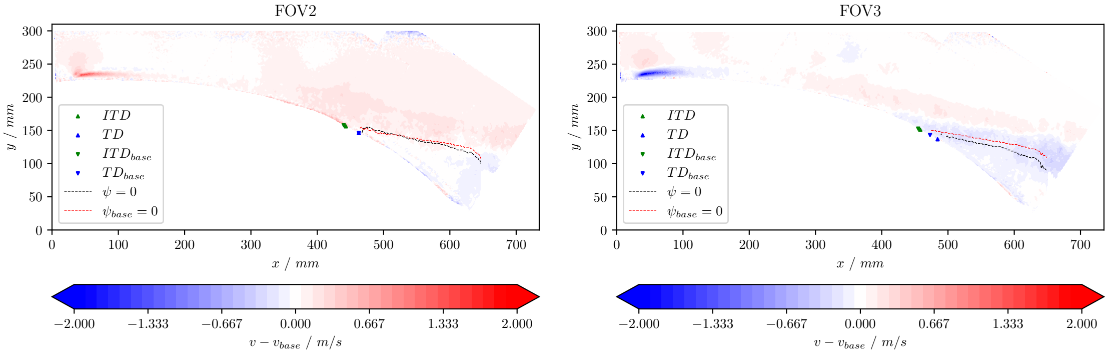

Figure 5.13: Contour representing the difference between y velocity of the forced case ($U_\infty = 10\ m/s$, $VR = 3.33$, $f = 80\ Hz$, streamwise slits) and y velocity of the unforced case; both FOVs are reported.

Figure 5.13 shows a very peculiar test case: it is immediately noticeable how in FOV3 the separation line is moved considerably closer to the wall, and both ITD and TD are shifted downstream; by all means, it appear like separation is delayed, well outside of the estabilished optimal frequency range.

This does not come *entirely* as a surprise: fig. 5.4 illustrates a clear local minimum at $f = 80\ Hz$ for the streamwise slits configuration; further investigations will be carried out in the following section through phase-averaging.

5.2.4 Final considerations

Time-averaged PIV data show - to some extent - correlation with pressure results.

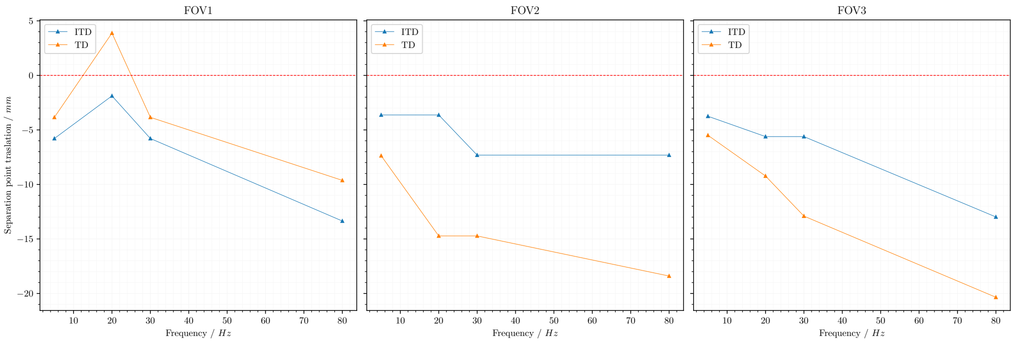

Figure 5.14: Distance between separation points in the forced ($VR = 3.33$, skewed slits) and unforced fields; a negative value indicates an upstream movement of ITD and TD.

Figure 5.14 summarizes all the data collected from skewed slits; the trend for FOV1 seems to agree with the pressure metric, while FOV2 and FOV3 appear to show very little correlation with fig. 5.4 - keeping in mind that the sample size in fig. 5.14 is much smaller.
This does not come as a surprise, since the spanwise location of the pressure tap array is equivalent to FOV1, i.e. it lies on a plane passing through two *convergent* skewed slits; what could be surprising is the intense *three-dimensionality* of the flow field: in a span of only 12 mm (the spacing between FOV1 and FOV3), the flow radically changes its behavior even towards the trailing edge, far downstream of the actuators.

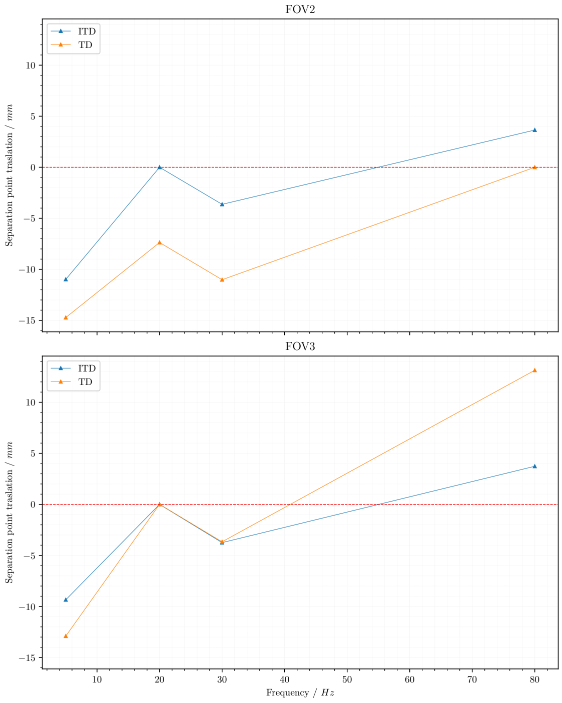

Figure 5.15: Distance between separation points in the forced ($VR = 3.33$, streamwise slits) and unforced fields; a negative value indicates an upstream movement of ITD and TD.

Data concerning streamwise slits is summarized in fig. 5.15. FOV2 and FOV3 show similar trends, although FOV3 exhibits higher maximum values for separation point traslation. This is expected, as FOV3 is located in the plane directly influenced by the structures generated by the jets.

Skewed slits appear to perform very well at the *ideal* spanwise location, whereas streamwise slits demonstrate greater flexibility, albeit at the cost of lower maximum effectiveness. Unfortunately, the lack of pressure data for FOV2 and FOV3 prevents a complete pressure characterization of the entire field.

To gain further insights about the mechanisms underlying the control method, phase-averaged data will now be presented.

5.3 Phase-averaged PIV results

Unless otherwise specified, all the phase-averaged results presented below refer to 4-bin discrete phase-averaging; the reference phase is the valve-signal period, and $t/T = 0$ is defined as the point in time when the valves open.

5.3.1 f = 20 Hz

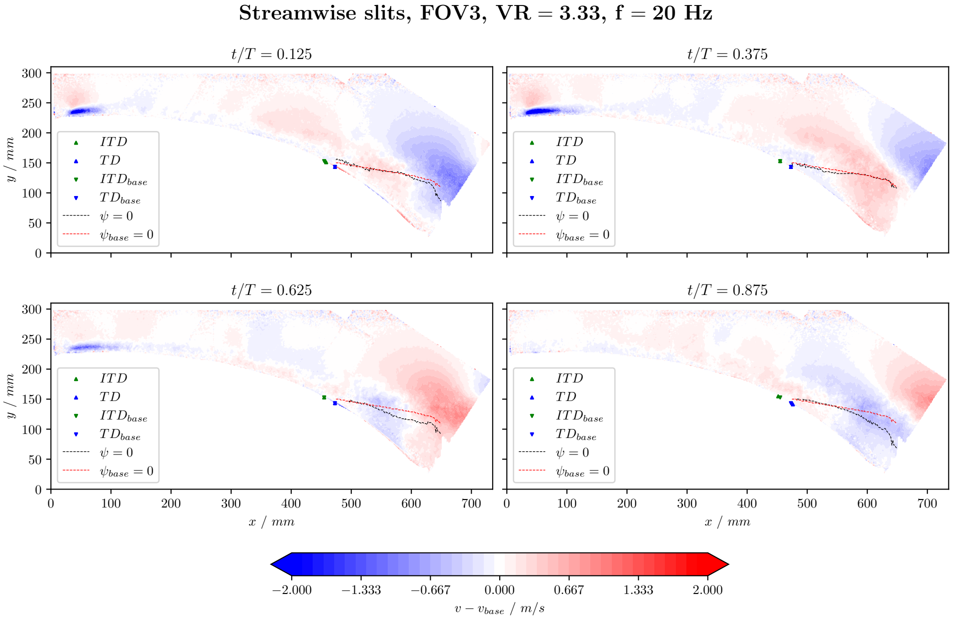

Figure 5.16: Discrete phase-averaging, 4 bins; the contour shows the difference in y velocity between the forced and unforced cases.

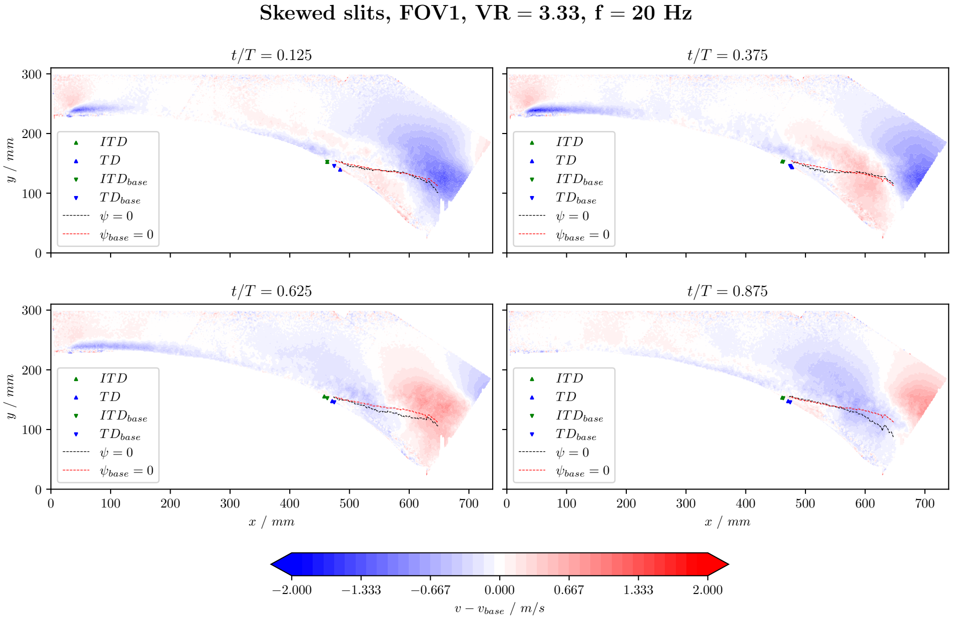

Figure 5.17: Discrete phase-averaging, 4 bins; the contour shows the difference in y velocity between the forced and unforced cases.

Figures 5.16 and 5.17 illustrate the two *best*-working test cases for streamwise and skewed slits respectively; the first important aspect to note is that the separation line is moved closer to the wall in the third and fourth quarters of the phase; for both configurations, it can be observed that the downwash region created by the jets - represented by the blue cloud near the top left of the image for $t/T = 0.125$ and $t/T = 0.375$ - is convected downstream, and it reaches the separation point at around $t/T = 0.625$. A closer look at this phenomenon can be taken by looking at the same fields with 12-bin phase-averaging in appendix E.

It should also be noted how the downwash region for the skewed slits is much more persistent than the one for their streamwise counterparts; possibly, structures maintain more coherence, or the vortices generated by streamwise slits are too close to the wall and are subsequently dissipated more easily.

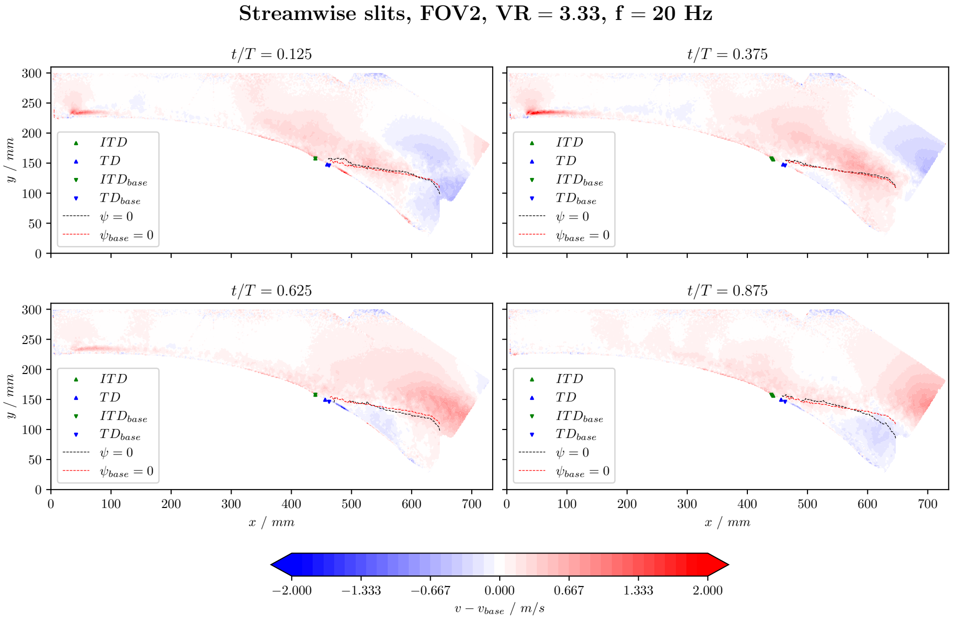
Streamwise slits, FOV2, VR = 3.33, f = 20 Hz

$t/T = 0.125$ $t/T = 0.375$ $t/T = 0.625$ $t/T = 0.875$

Figure 5.18: Discrete phase-averaging, 4 bins; the contour shows the difference in y velocity between the forced and unforced cases.

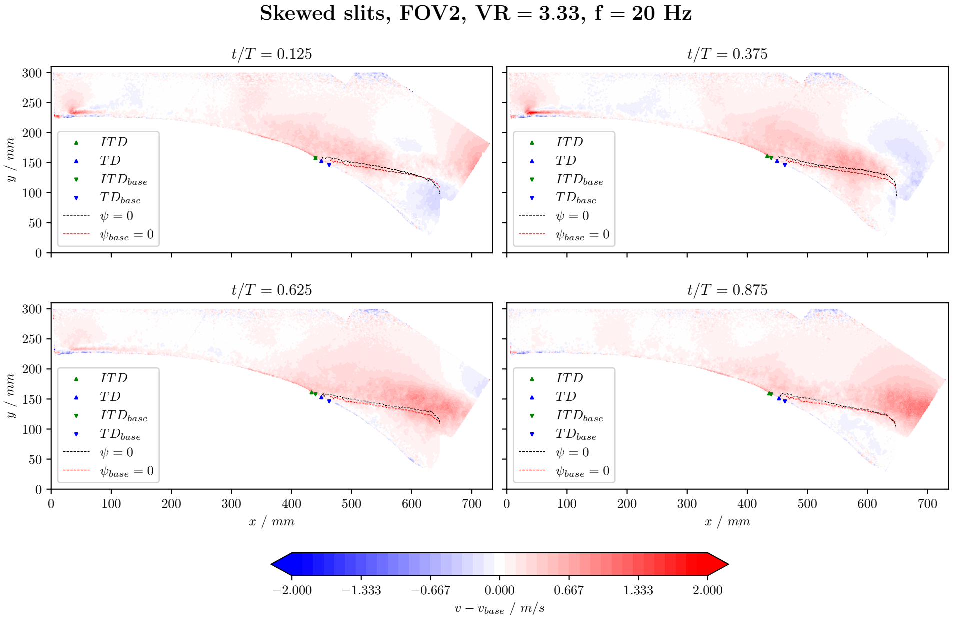
Skewed slits, FOV2, VR = 3.33, f = 20 Hz

$t/T = 0.125$ $t/T = 0.375$ $t/T = 0.625$ $t/T = 0.875$

Figure 5.19: Discrete phase-averaging, 4 bins; the contour shows the difference in y velocity between the forced and unforced cases.

A different situation manifests itself in FOV2, as shown in figures 5.18 and 5.19: the *upwash* cloud generated by the jet is dissipated before reaching the separation point; phase-averaging reveals how at all points in the phase the separation point is shifted upstream, almost as if the virtual *wall* effect created by the jet persists even when the valves are closed.

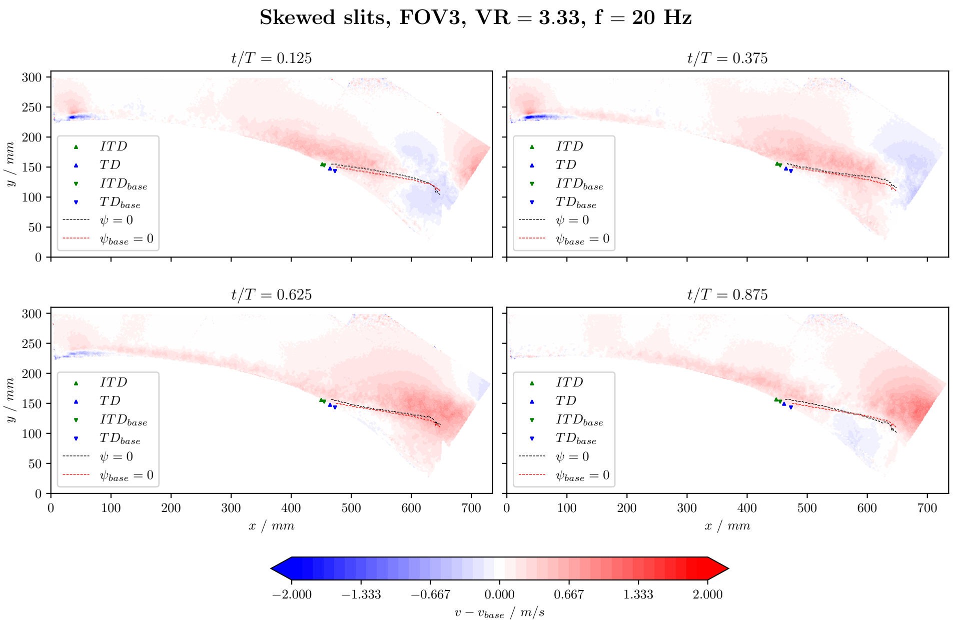

Figure 5.20: Discrete phase-averaging, 4 bins; the contour shows the difference in y velocity between the forced and unforced cases.

An interesting effect is exposed in FOV3 by the skewed slits (fig. 5.20): control has little effect on separation, possibly because the blue downwash cloud generated by the jets is too close to the wall, and is dissipated by viscosity before it can reach the separation point; another possible explanation is that, due to the non-penetration condition at the wall, the downwash is simply arrested, and it cannot persist far downstream.
In any case, it seems like the key to effective separation control is inducing a downwash region not too close to the wall.

5.3.2 f = 80 Hz

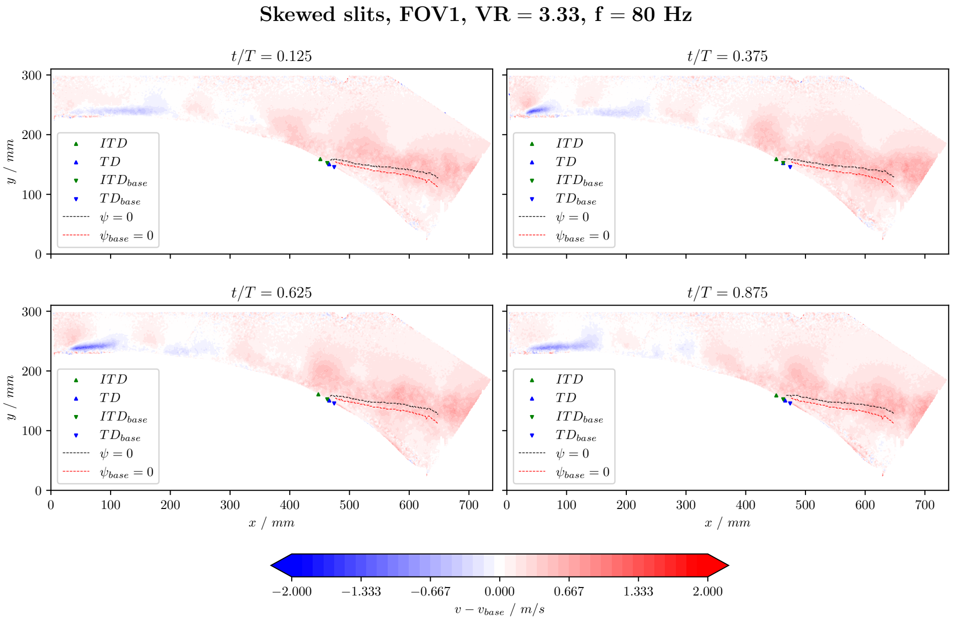

Figure 5.21: Discrete phase-averaging, 4 bins; the contour shows the difference in y velocity between the forced and unforced cases.

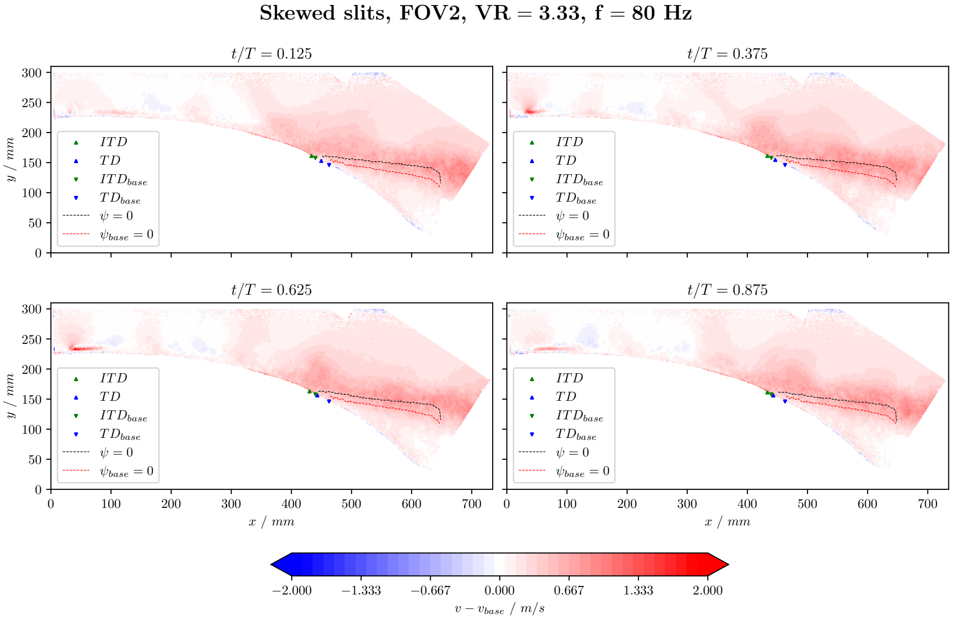

Figure 5.22: Discrete phase-averaging, 4 bins; the contour shows the difference in y velocity between the forced and unforced cases.

The focus is now shifted to a different frequency; particularly, for $f = 80$ Hz, FOV2 (fig. 5.21) PIV shows how the downwash region on the top left corner at $t/T = 0.125$ is slowly dissipated as it gets convected downstream, and it completely disappears before reaching the separation point. The reasons behind this dissipation possibly relate to interactions between the actuation frequency and natural frequencies of the flow; unfortunately, due to the large time resolution of the PIV acquisition, such information is impossible to discern with the data at hand.

Another important feature to observe is how the valves mechanical and pneumatical inertia make it too slow to keep up with the the requested frequency: the valves do not open exactly when they should (first and second quarter of the phase), but instead they open with a finite *delay*; this appears even more evident in fig. 5.22, which shows the field of view passing through one of the slits.

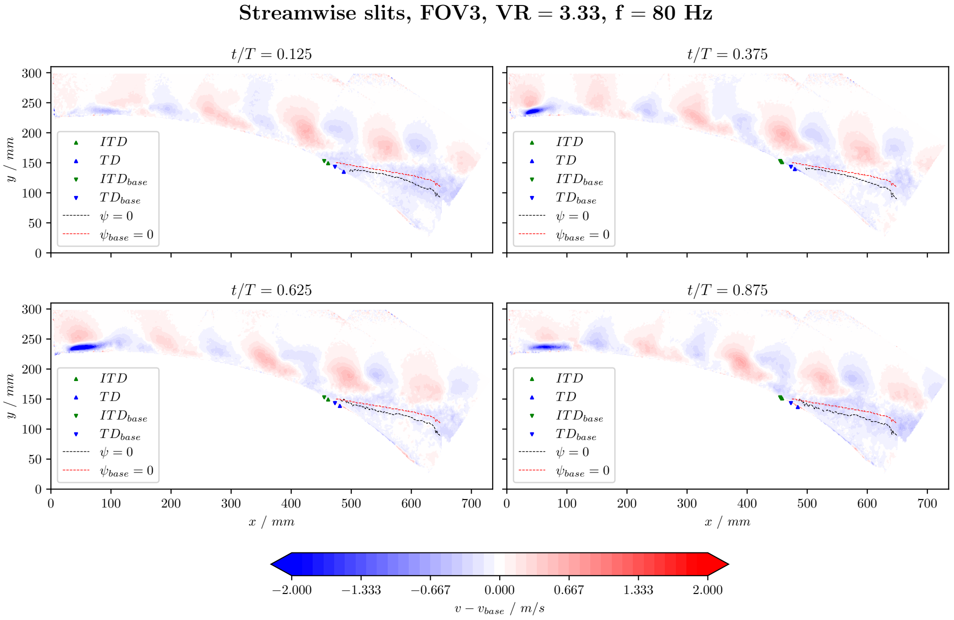

Figure 5.23: Discrete phase-averaging, 4 bins; the contour shows the difference in y velocity between the forced and unforced cases.

Perhaps, the most intriguing test case emerging from phase-average analysis is the one shown in fig. 5.23: it is crystal clear that the structures generated by the jets show *marvelous* coherence; perhaps, this is the reason why fig. 5.4 shows a *local minimum* at $f = 80\ Hz$, and fig. 5.13 shows separation delay.

This phenomenon is probably related to *subharmonics*, since 80 Hz is an integer multiple of the optimal 20 Hz; however, further investigations can only be carried out with higher time resolution measurements, such as hot wire anemometry or time-resolved PIV - which go beyond the scope of this thesis.

Conclusions and recommendations

It was found that skewed slits perform better than their streamwise counterparts, particularly when placed at the optimal spanwise location, due to a more persistent and coherent downwash region; this effect is likely present because skewed slits generate vortices that remain more stable and less susceptible to dissipation than those produced by streamwise slits, which tend to be too close to the wall.
In non-optimal fields of view, skewed slit-induced vortices appeared to dissipate more quickly, likely due to proximity to the wall. Regarding frequency performance, certain frequencies were more effective because they sustained the downwash structures better, while others allowed these structures to dissipate too quickly. Unfortunately, the PIV data lacked sufficient time resolution to fully explore the underlying causes behind this phenomenon.

Pressure measurements were appropriately conducted in the streamwise direction, but not in the spanwise direction, where the flow's unexpected strong spanwise variability would have required additional pressure tap arrays at various spanwise locations: ideally, three pressure tap arrays corresponding to the spanwise locations of FOV1, FOV2 and FOV3.
The PIV data, while generally correlating well with the pressure data - at least in the comparable spanwise locations -, had its own limitations; although the fields of view offered a reasonable overview, improvements such as adding a perpendicular view or using stereo-PIV would enhance the ability to assess streamwise vorticity.

In conclusion, the limitation given by the mass flow controller's full scale didn't allow for chord-based Reynolds numbers higher than $\sim 8{\cdot}10^5$: to keep the velocity ratio high enough for the control method to have any positive effect, the tunnel's freestream velocity had to be limited to 10 m/s.

Appendix - vortex identification

To identify a vortex, one must first understand what a vortex is; surprisingly, a definition doesn't come as easy as one could expect: a vortex can be defined as a finite region of vorticity immersed in irrotational fluid[25]. This thesis is mainly interested in studying vortex filaments, not accounting for vortex sheets (such as the sheet region of vorticity generated in a shear layer).

When it comes to identifying vortex filaments, numerous mathematical tools are available[7]; the most intuitive of these methods would be to establish a *vorticity threshold*: a vortex is a region where vorticity is higher than a certain threshold value, i.e.

$$|\omega| > \omega_{thresh}$$

where the vorticity $\vec{\omega}$ is defined as the velocity field's curl, $\vec{\omega} = \nabla \times \vec{u}$.
This method, while easily implementable, presents a series of criticalities:

- the value of ω_{thresh} is arbitrary;
- there is no distinction between vortex sheets and vortex filaments;
- identifying the vortex's centerline is not possible, since the maximum of $|\omega|$ is not always located in the middle of a vortex;
- the criterion isn't *objective*: considering two reference frames that move with a finite angular velocity with respect to each other, the vorticity value will be different in such systems.

A.0.1 The Q criterion

Assuming incompressible flow, the quantity Q can be defined:

$$Q = \frac{1}{2}\left(||\boldsymbol{\Omega}||^2 - ||\boldsymbol{S}||^2\right) \tag{A.1}$$

where $||\cdot||$ is the Frobenius norm, and $\boldsymbol{\Omega}$ is the *angular rotation rate tensor* and $\boldsymbol{S}$ is the *strain rate tensor*, i.e.

$$\Omega_{i,j} = \frac{1}{2}\left(\frac{\partial u_i}{\partial x_j} - \frac{\partial u_j}{\partial x_i}\right)$$

$$S_{i,j} = \frac{1}{2}\left(\frac{\partial u_i}{\partial x_j} + \frac{\partial u_j}{\partial x_i}\right)$$

This method identifies a vortex as a region where

1. $Q > Q_{thresh}$
2. there exists a point where pressure tends to a minimum

The second condition is typically automatically satisfied in regions where the first one is; the value of Q_{thresh} is, again, arbitrary: setting it too low may result in identifying vortices with lack of physical meaning, while setting it too high can lead to the risk of ignoring relevant ones.

Appendix - jet characterization: non-uniformity results

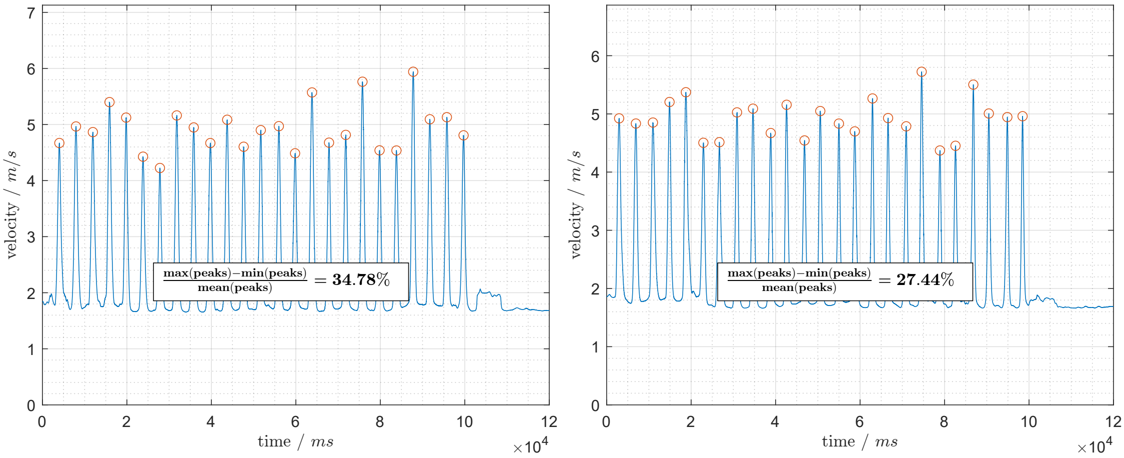

(a) Streamwise slits.

(b) Skewed slits.

Figure B.1: 9% of mass flow controller full scale.

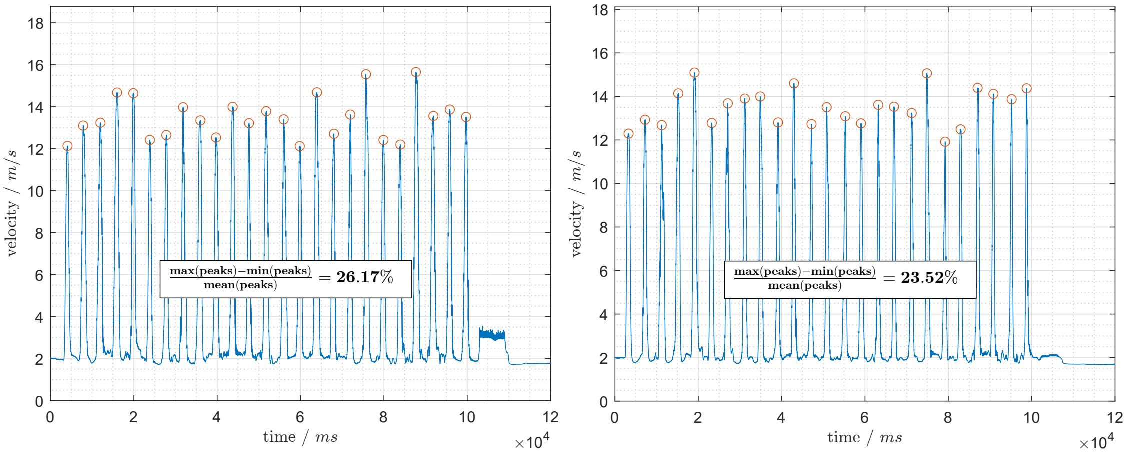

(a) Streamwise slits.

(b) Skewed slits.

Figure B.2: 27% of mass flow controller full scale.

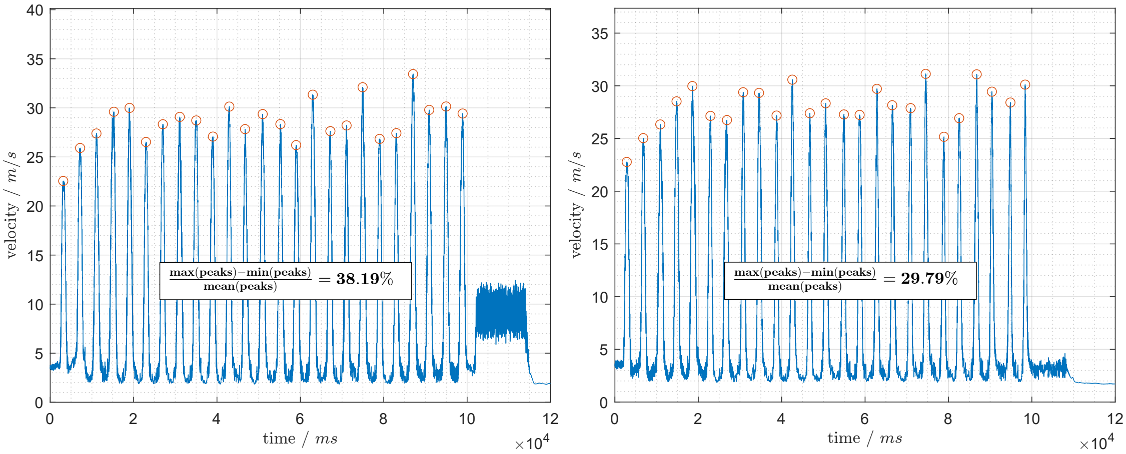

(a) Streamwise slits.

(b) Skewed slits.

Figure B.3: 72% of mass flow controller full scale.

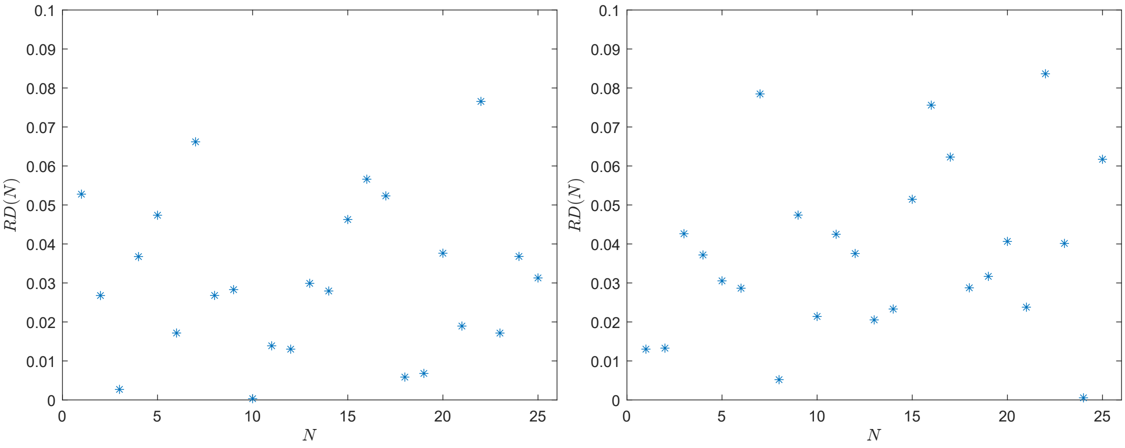

(a) MFC set to 9% of full scale value.

(b) MFC set to 27% of full scale value.

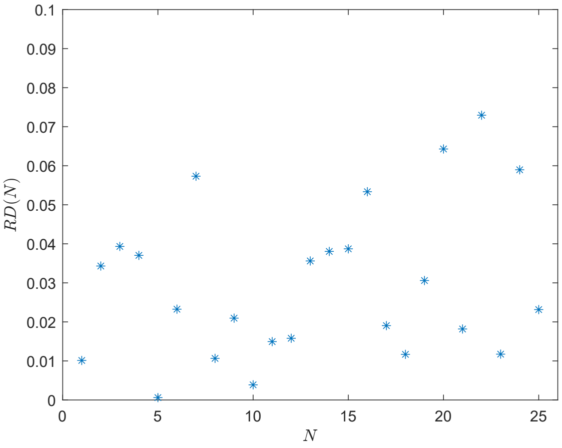

(c) MFC set to 72% of full scale value.

Figure B.4: Comparison between streamwise and skewed slits.

Appendix - jet characterization: time series

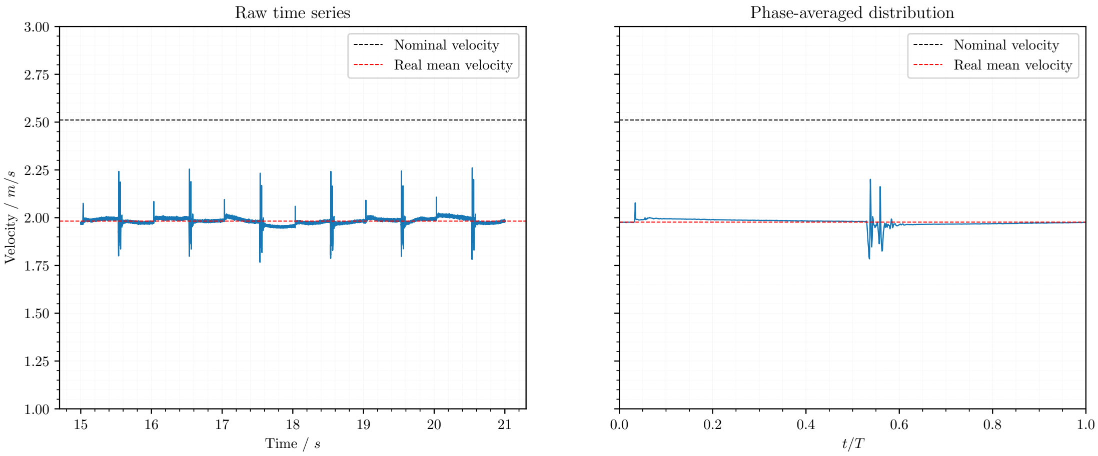

Figure C.1: Mass flow controller set to 11.3% of full scale, valves operated at $f = 1\ Hz$.

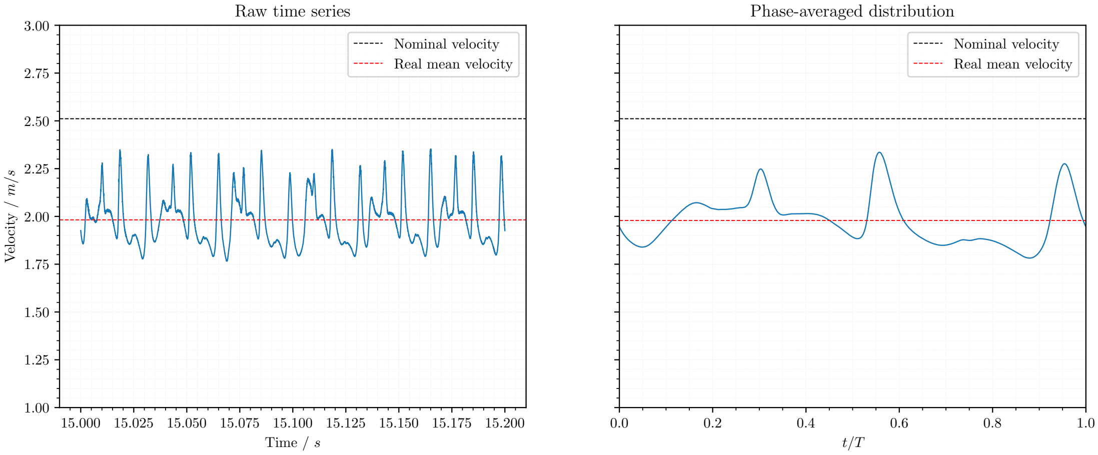

Figure C.2: Mass flow controller set to 11.3% of full scale, valves operated at $f = 30\ Hz$.

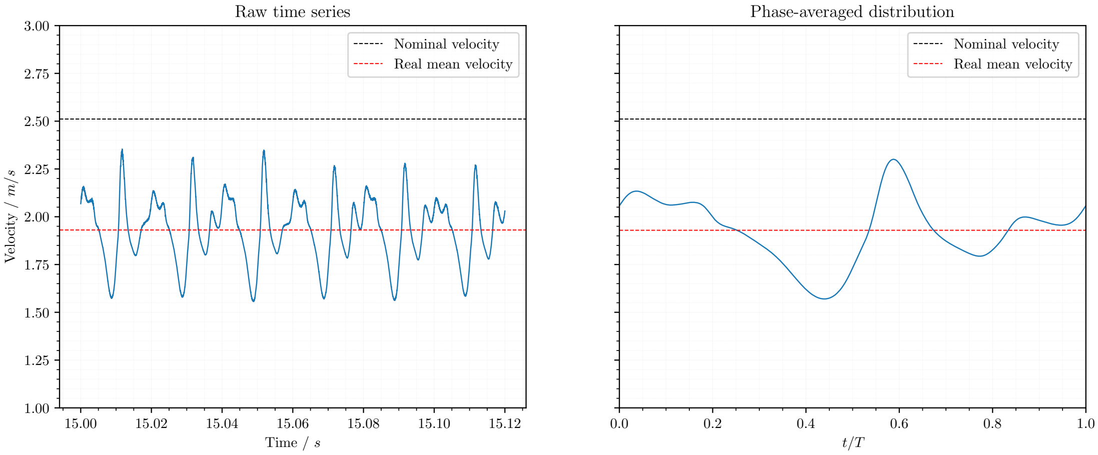

Figure C.3: Mass flow controller set to 11.3% of full scale, valves operated at $f = 50\ Hz$.

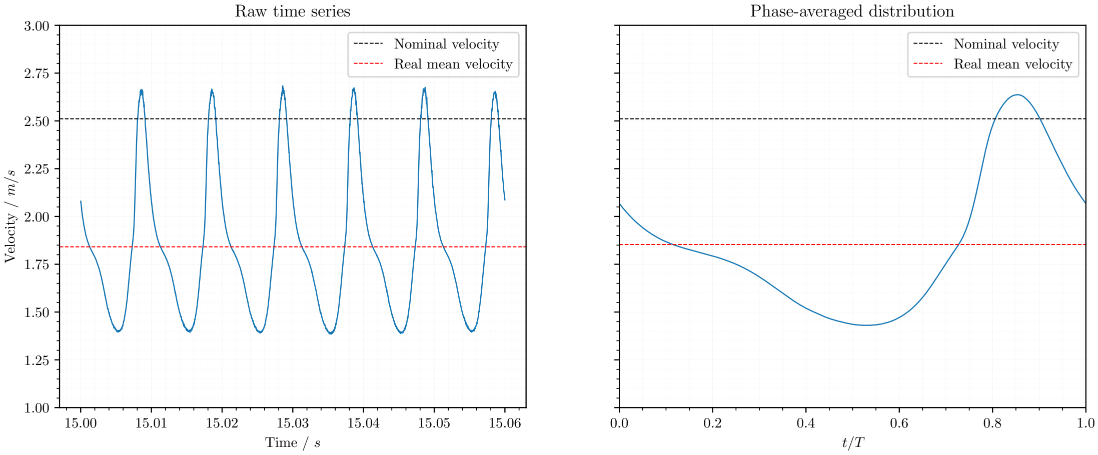

Figure C.4: Mass flow controller set to 11.3% of full scale, valves operated at $f = 100\ Hz$.

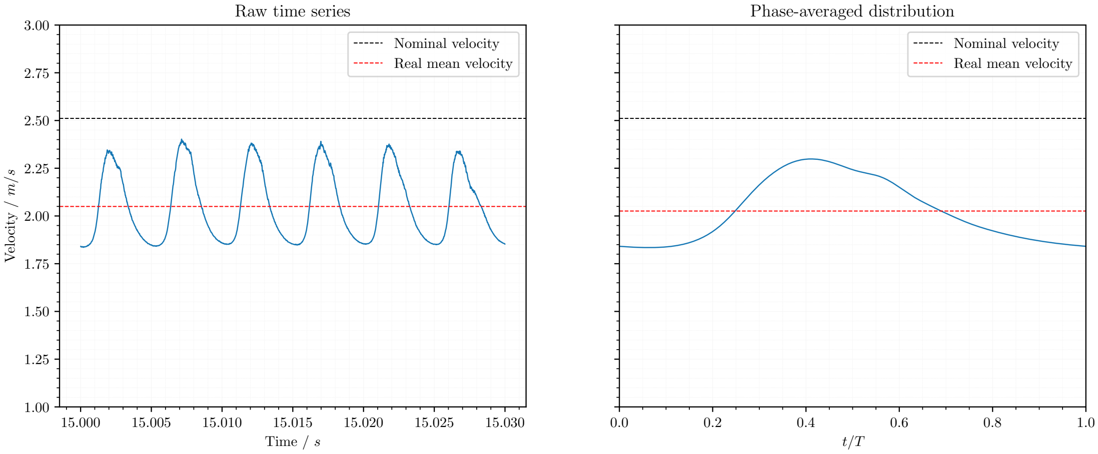

Figure C.5: Mass flow controller set to 11.3% of full scale, valves operated at $f = 200\ Hz$.

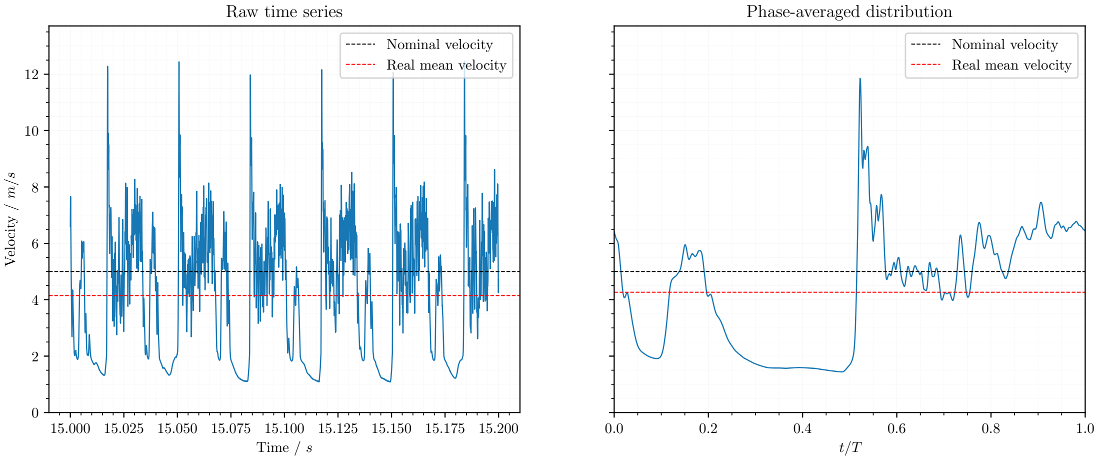

Figure C.6: Mass flow controller set to 22.5% of full scale, valves operated at $f = 30\ Hz$.

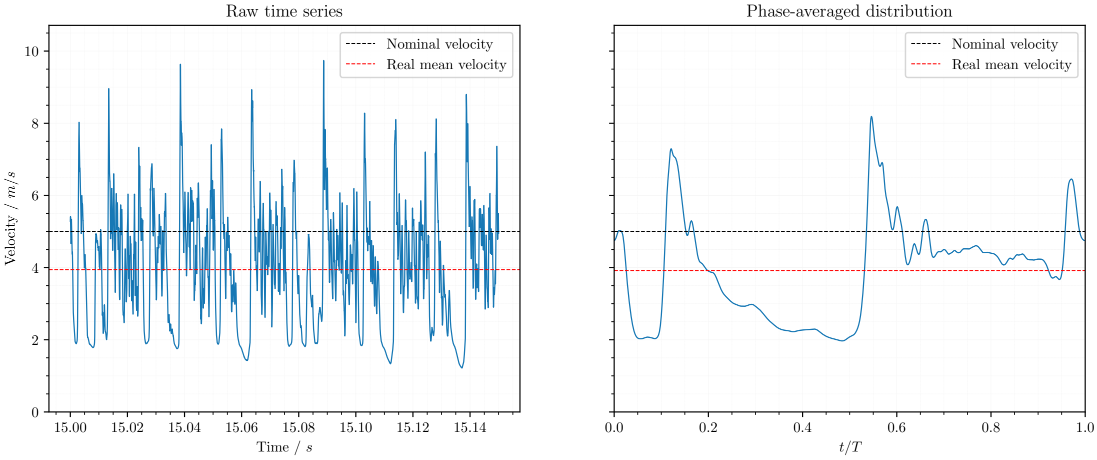

Figure C.7: Mass flow controller set to 22.5% of full scale, valves operated at $f = 40\ Hz$.

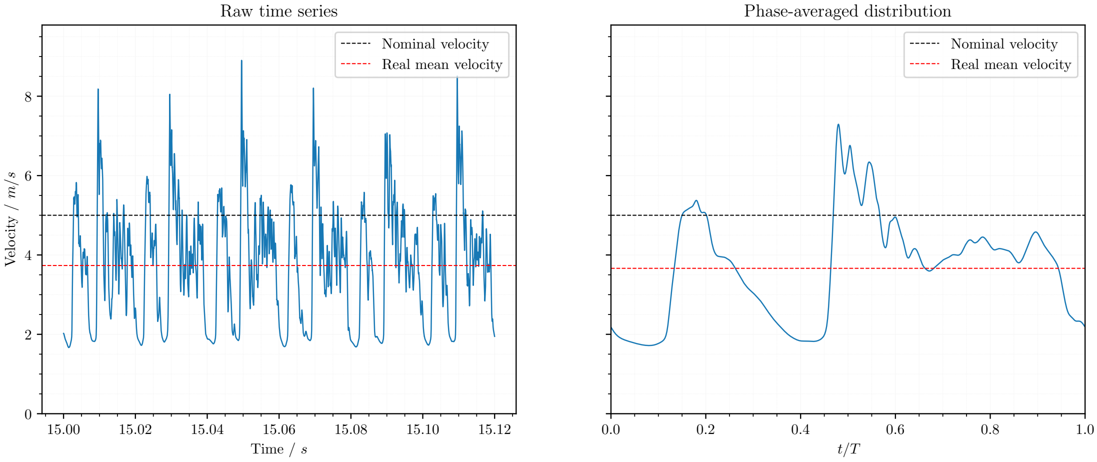

Figure C.8: Mass flow controller set to 22.5% of full scale, valves operated at $f = 50\ Hz$.

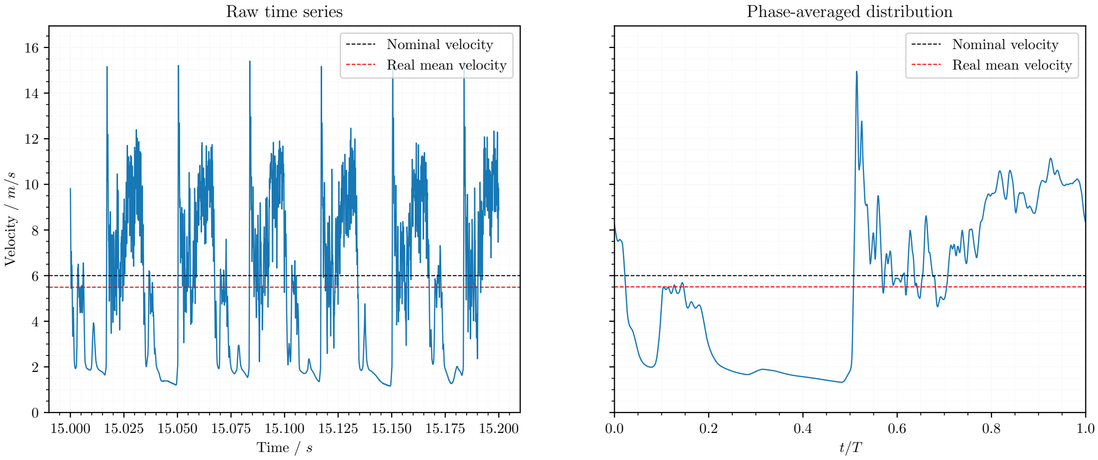

Figure C.9: Mass flow controller set to 27% of full scale, valves operated at $f = 30\ Hz$.

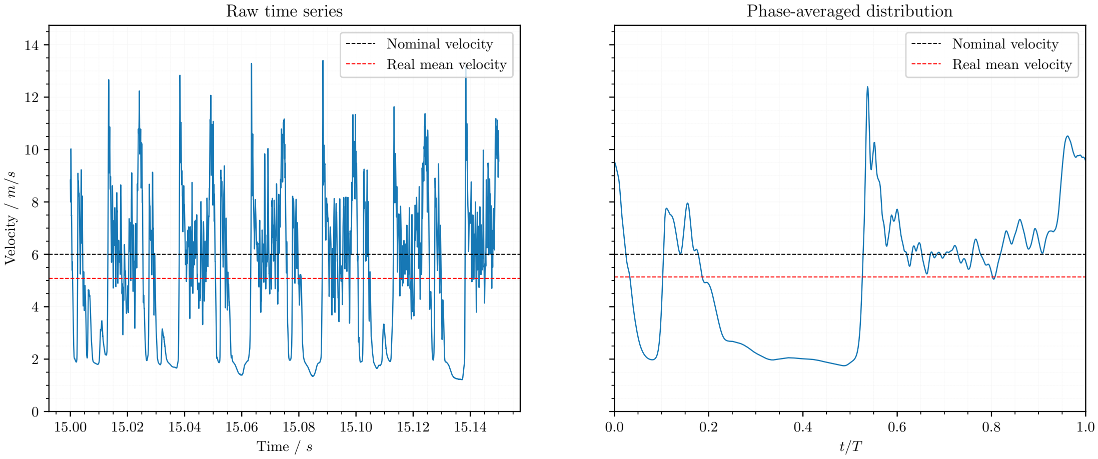

Figure C.10: Mass flow controller set to 27% of full scale, valves operated at $f = 40\ Hz$.

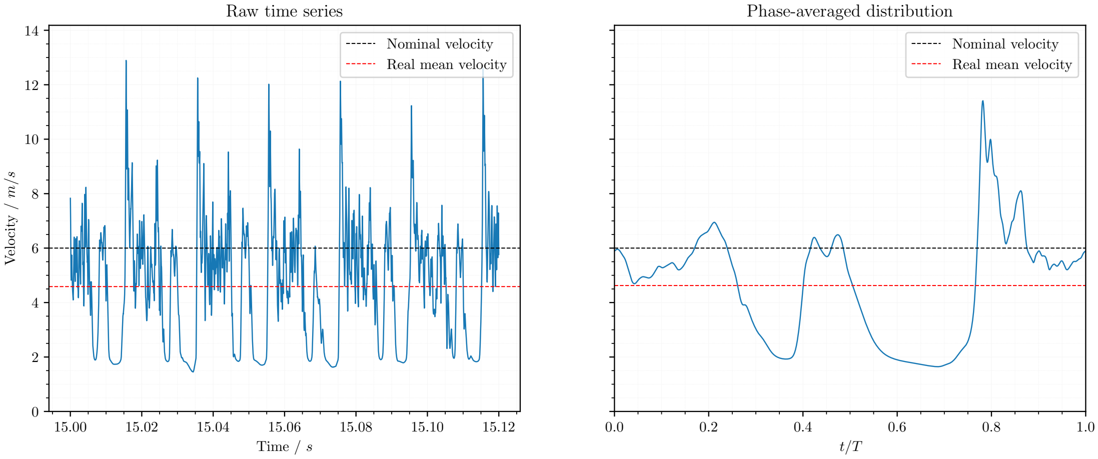

Figure C.11: Mass flow controller set to 27% of full scale, valves operated at $f = 50\ Hz$.

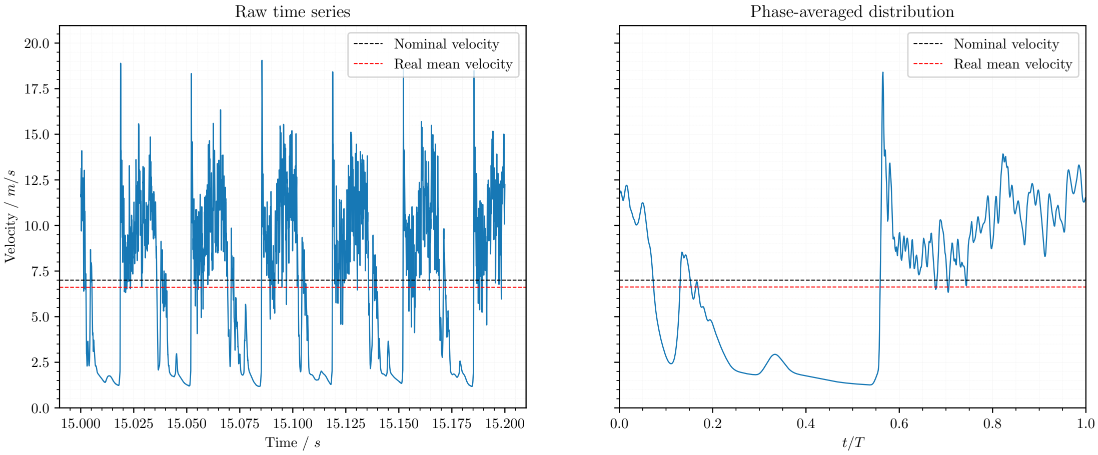

Figure C.12: Mass flow controller set to 31.5% of full scale, valves operated at $f = 30\ Hz$.

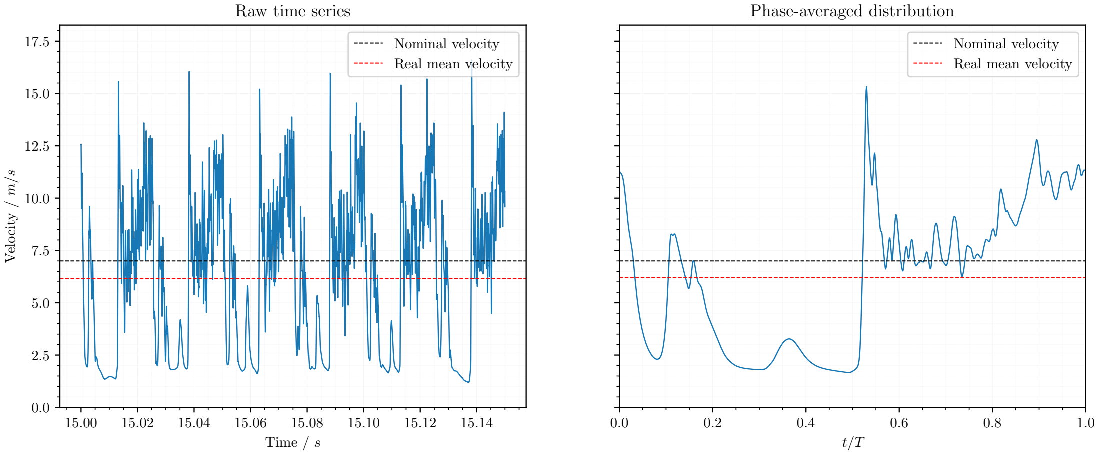

Figure C.13: Mass flow controller set to 31.5% of full scale, valves operated at $f = 40\ Hz$.

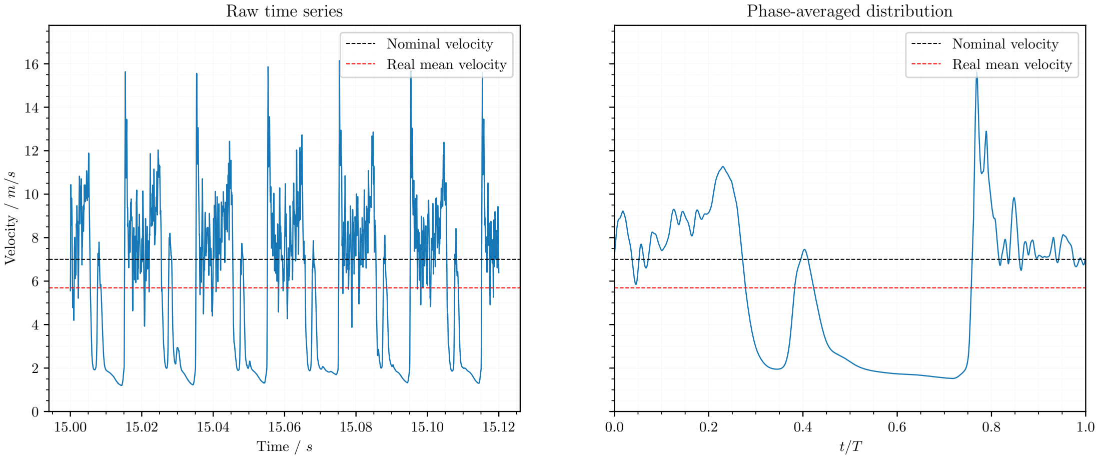

Figure C.14: Mass flow controller set to 31.5% of full scale, valves operated at $f = 50\ Hz$.

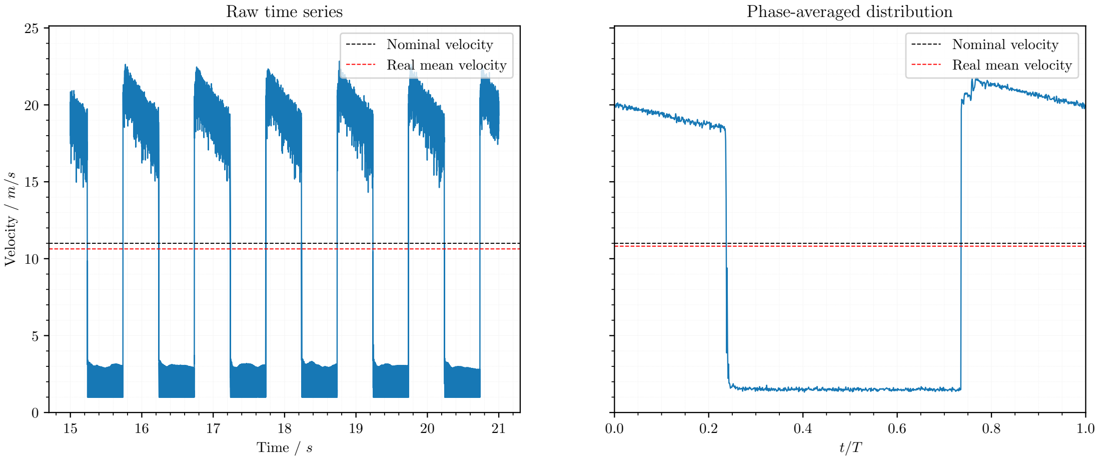

Figure C.15: Mass flow controller set to 49.5% of full scale, valves operated at $f = 1\ Hz$.

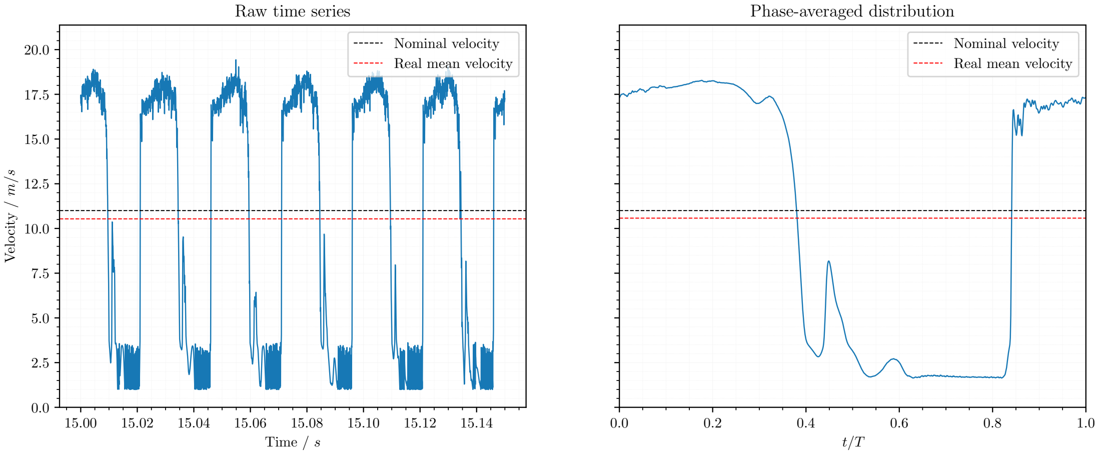

Figure C.16: Mass flow controller set to 49.5% of full scale, valves operated at $f = 40\ Hz$.

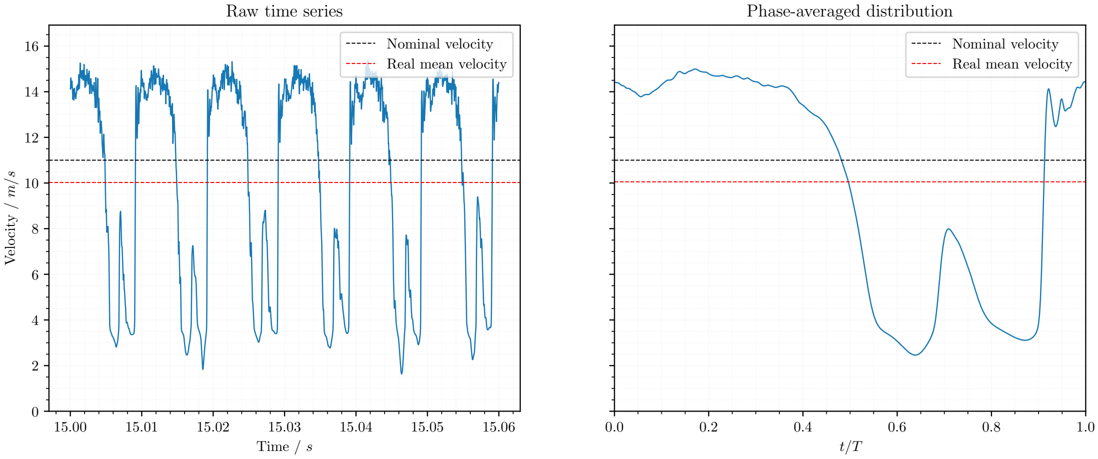

Figure C.17: Mass flow controller set to 49.5% of full scale, valves operated at $f = 100\ Hz$.

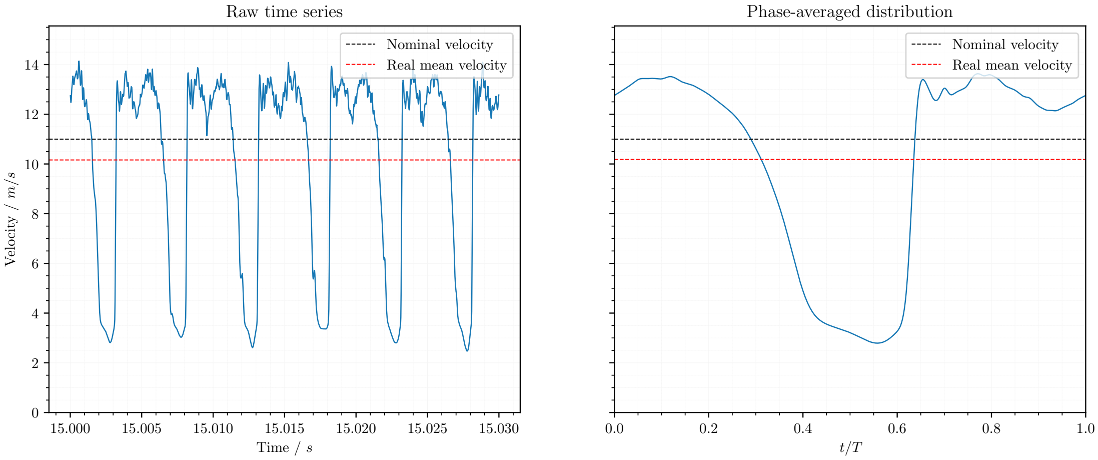

Figure C.18: Mass flow controller set to 49.5% of full scale, valves operated at $f = 200\ Hz$.

Appendix - PIV results, unforced field

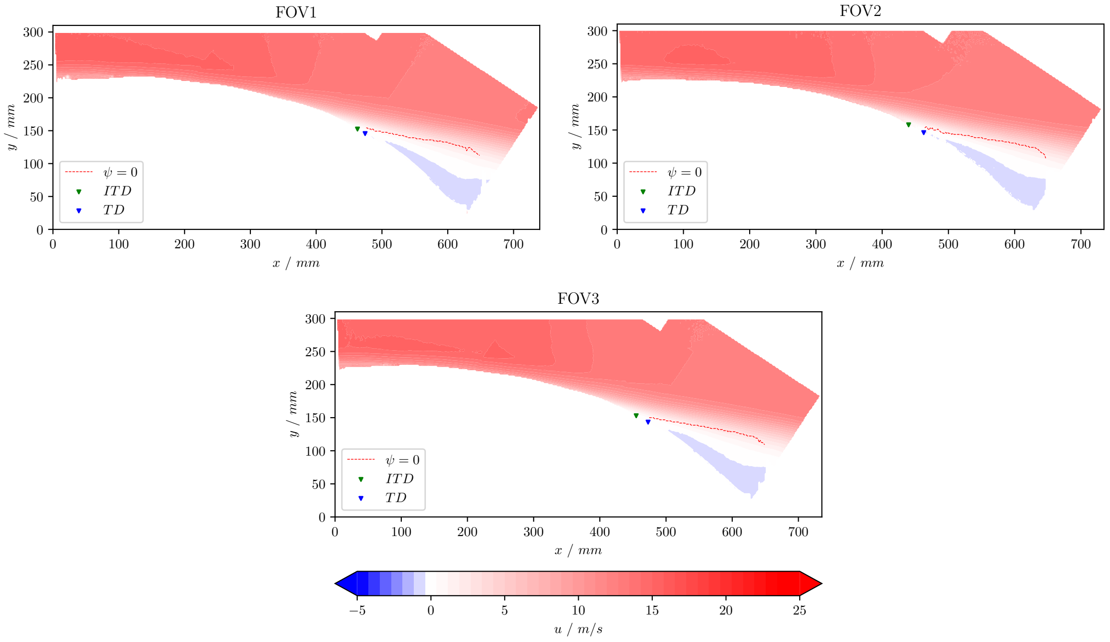

Figure D.1: x velocity component.

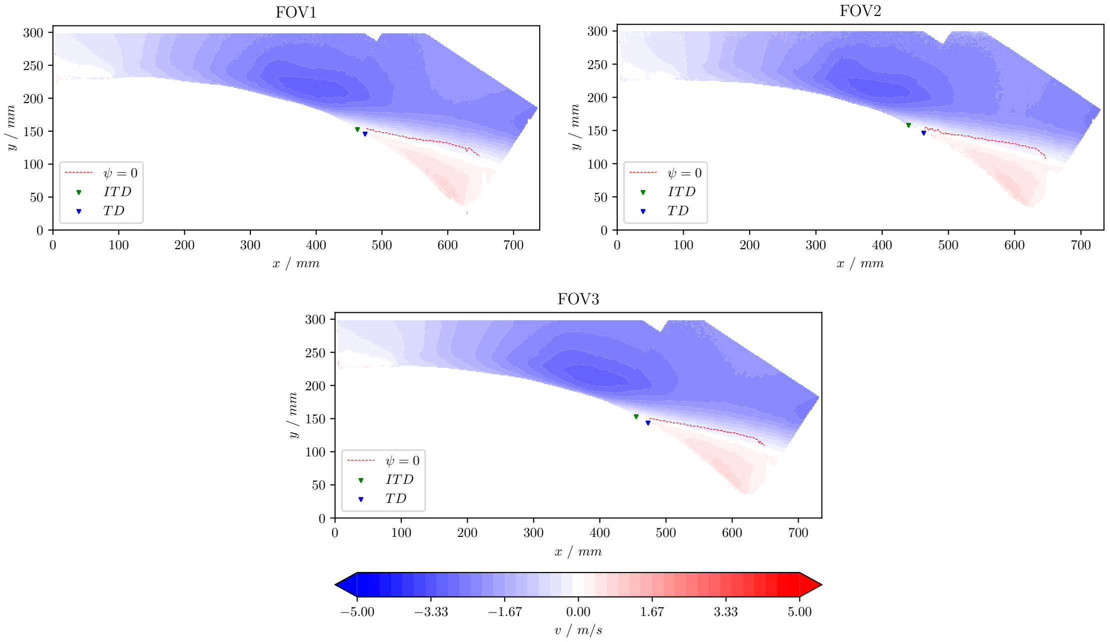

Figure D.2: y velocity component.

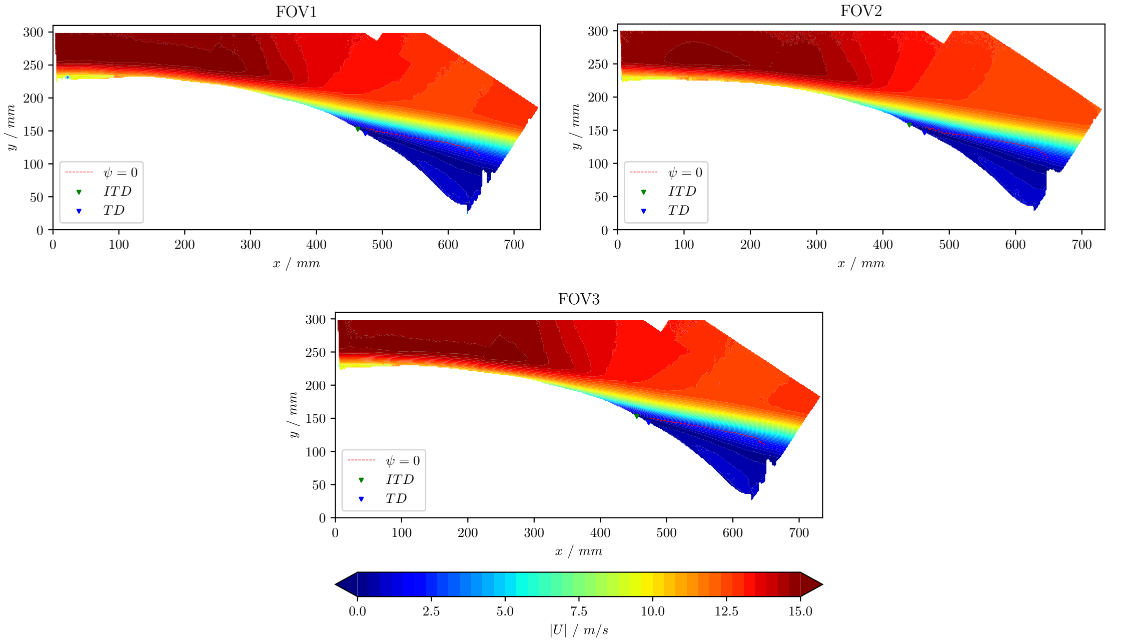

Figure D.3: Velocity magnitude.

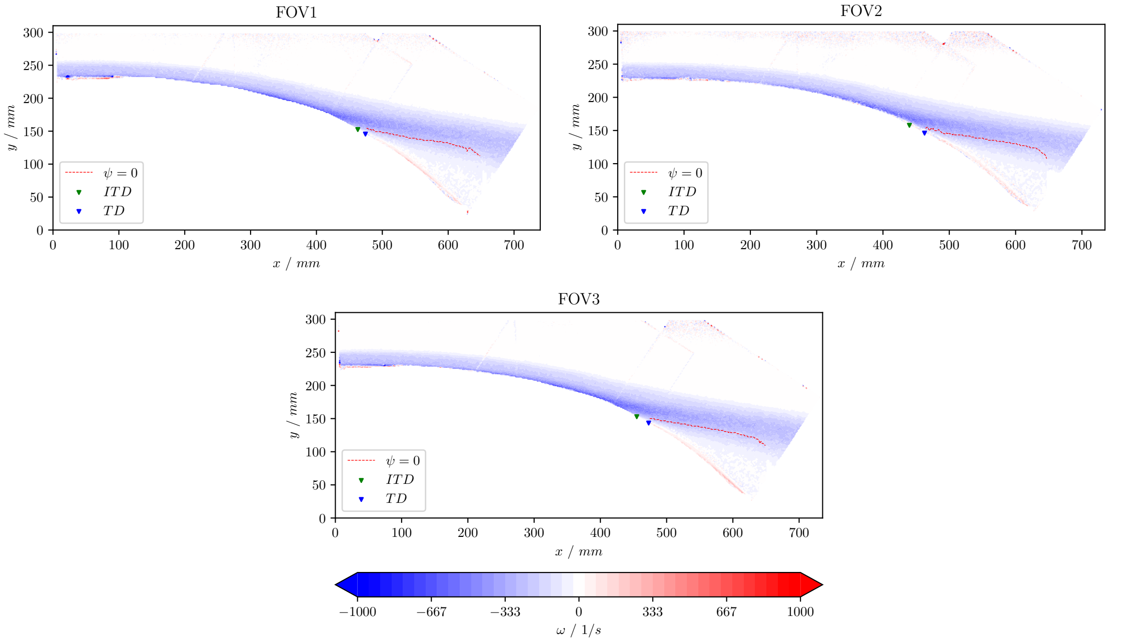

Figure D.4: z vorticity.

Appendix - 12-bin phase-averaging

E.1 Streamwise slits, FOV3, 20 Hz, $VR = 3.33$

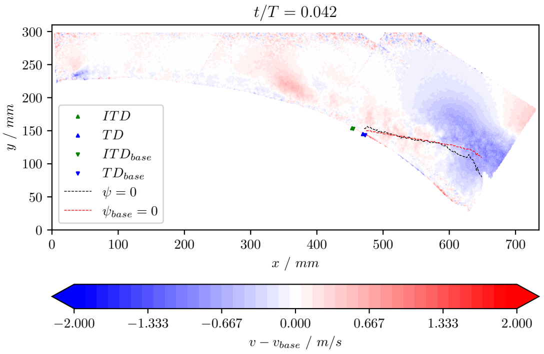

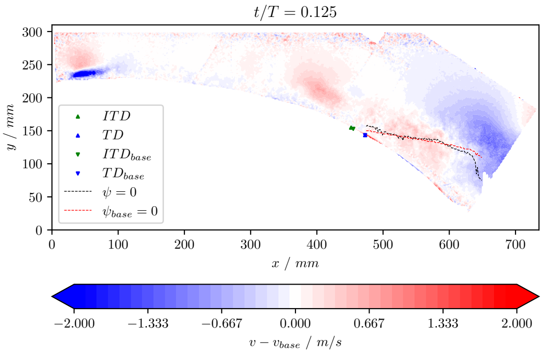

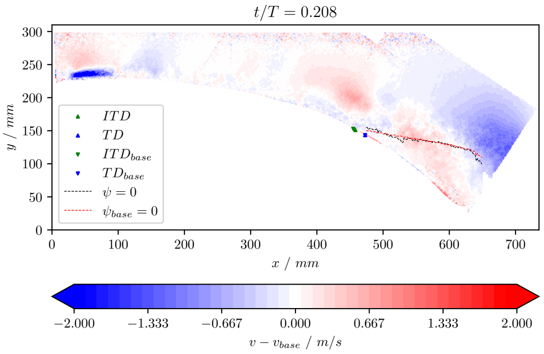

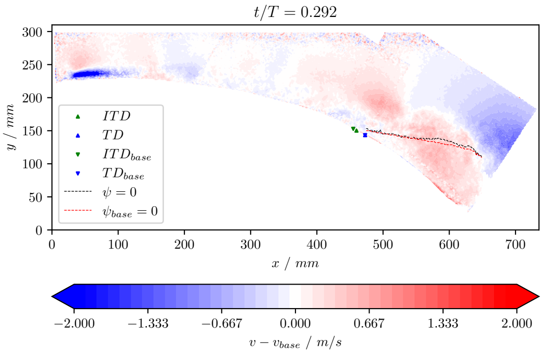

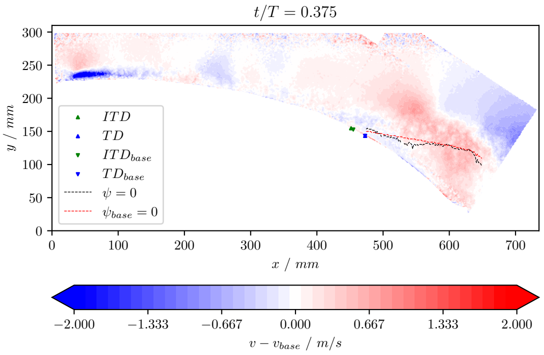

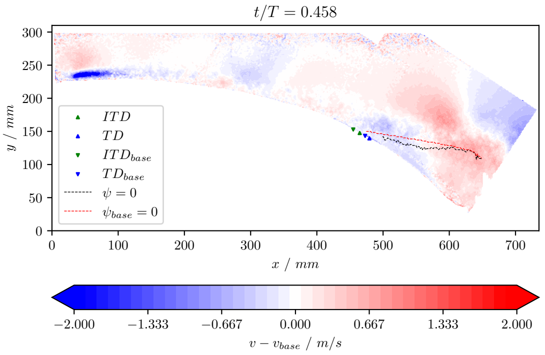

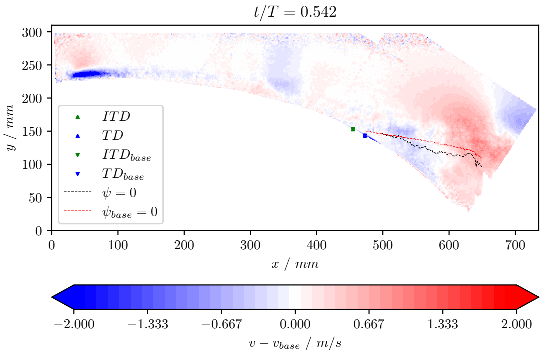

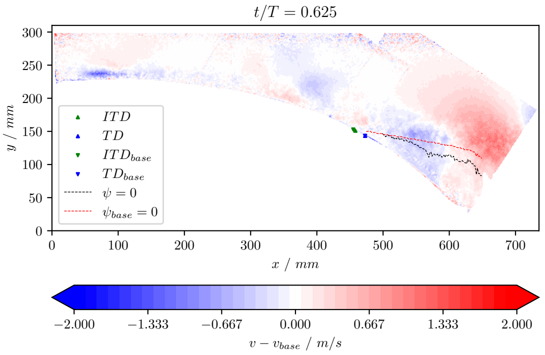

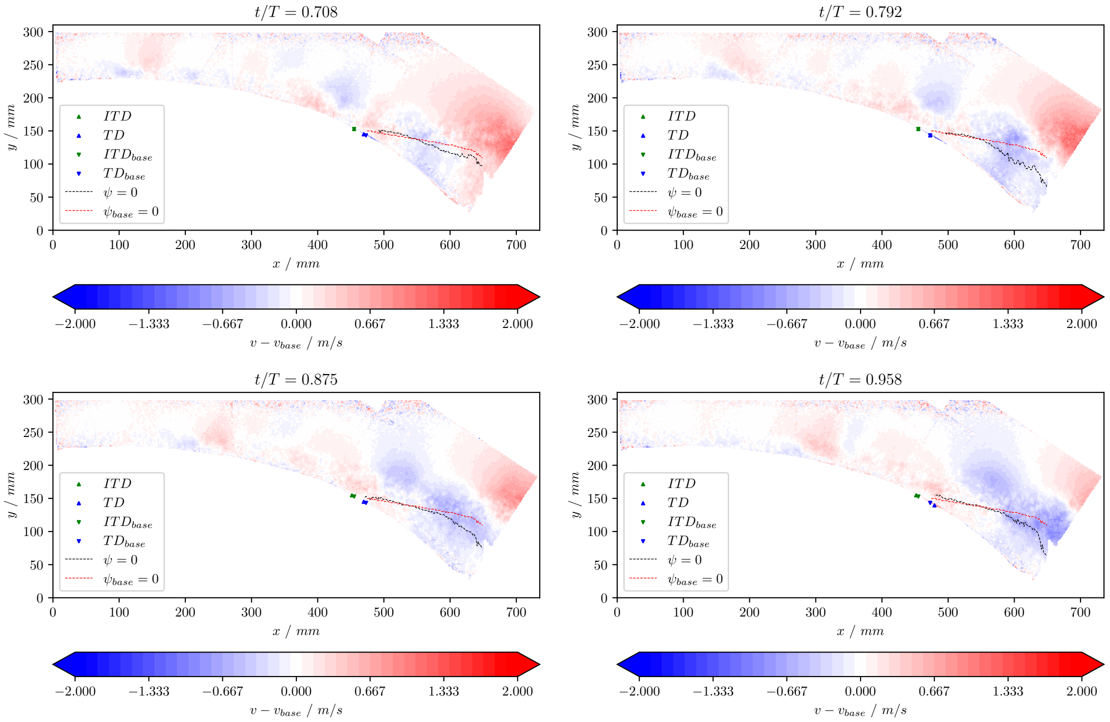
$t/T = 0.708$

$t/T = 0.792$

$t/T = 0.875$

$t/T = 0.958$

Figure E.2: Discrete phase-averaging, 12 bins; the contour shows the difference in y velocity between the forced (streamwise slits, 20 Hz, $VR = 3.33$) and unforced cases for FOV3.

E.2 Skewed slits, FOV1, 20 Hz, $VR = 3.33$

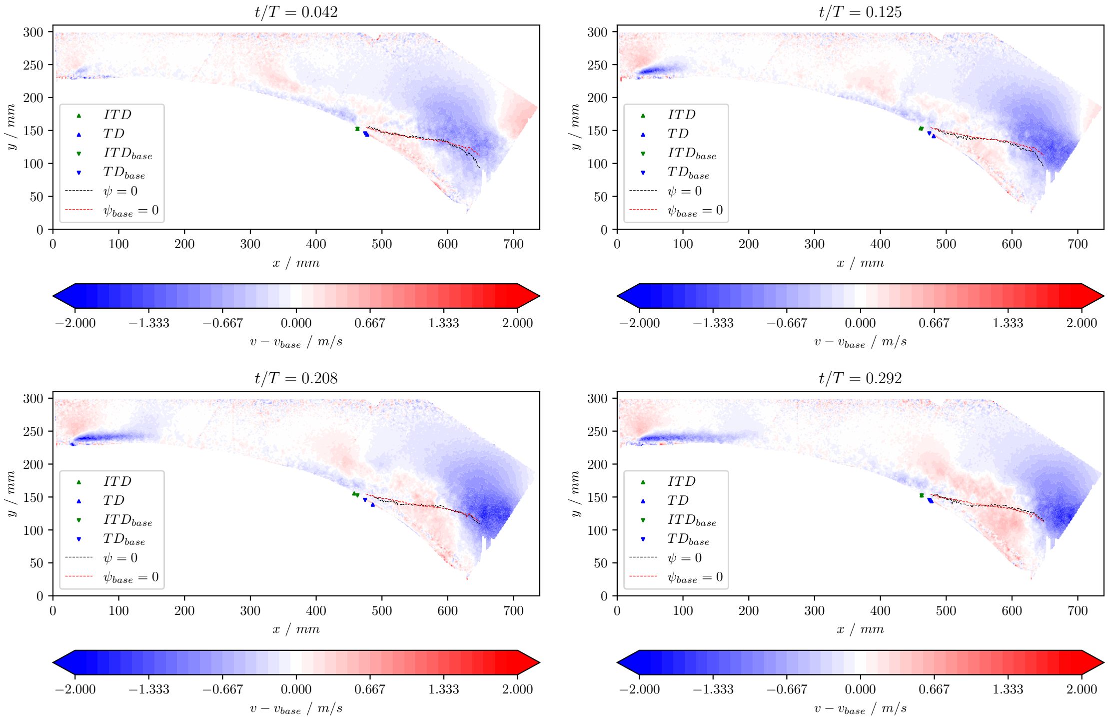
$t/T = 0.042$

$t/T = 0.125$

$t/T = 0.208$

$t/T = 0.292$

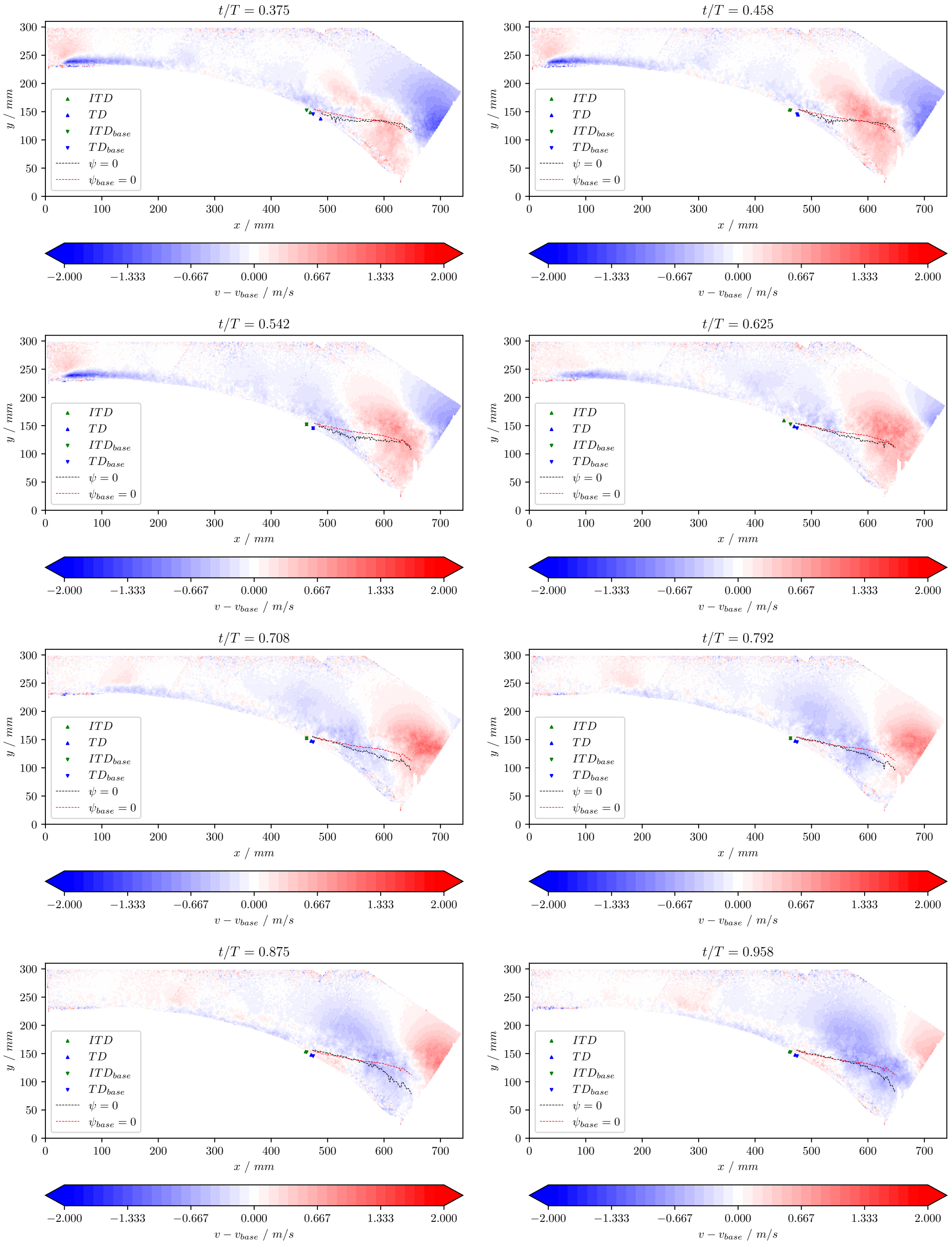

Figure E.4: Discrete phase-averaging, 12 bins; the contour shows the difference in y velocity between the forced (skewed slits, 20 Hz, $VR = 3.33$) and unforced cases for FOV1.

Bibliography

[1] Yoshiaki Abe et al. "Comparison of Separation Control Mechanisms for Synthetic Jet and Plasma Actuators". In: *Actuators* 12 (8 2023). ISSN: 20760825. DOI: `10.3390/act12080322`.

[2] Renzo Arina. *Fondamenti di Aerodinamica*. Levrotto & Bella, 2015.

[3] R. E. Breidenthal. "Structure and mixing of a transverse jet in incompressible flow". In: *Journal of Fluid Mechanics* 148 (1984). ISSN: 14697645. DOI: `10.1017/S0022112084002408`.

[4] Tyler Van Buren et al. "Impact of orifice orientation on a finite-span synthetic jet interaction with a crossflow". In: *Physics of Fluids* 28 (3 2016). ISSN: 10897666. DOI: `10.1063/1.4943520`.

[5] Sébastien Deck. "Recent improvements in the Zonal Detached Eddy Simulation (ZDES) formulation". In: *Theoretical and Computational Fluid Dynamics* 26 (6 2012). ISSN: 09354964. DOI: `10.1007/s00162-011-0240-z`.

[6] J. K. Eaton and J. P. Johnston. "A review of research on subsonic turbulent flow reattachment". In: *AIAA Journal* 19 (9 1981). ISSN: 00011452. DOI: `10.2514/3.60048`.

[7] Brenden P. Epps. "Review of vortex identification methods". In: *AIAA SciTech Forum - 55th AIAA Aerospace Sciences Meeting*. 2017. DOI: `10.2514/6.2017-0989`.

[8] Mohamed Gad-el-Hak and Dennis M. Bushnell. *Separation control: Review*. 1991. DOI: `10.1115/1.2926497`.

[9] J. L. Gilarranz, L. W. Traub, and O. K. Rediniotis. "A new class of synthetic jet actuators - Part II: Application to flow separation control". In: *Journal of Fluids Engineering, Transactions of the ASME* 127 (2 2005). ISSN: 00982202. DOI: `10.1115/1.1882393`.

[10] G. Godard, J. M. Foucaut, and M. Stanislas. "Control of a decelerating boundary layer. Part 2: Optimization of slotted jets vortex generators". In: *Aerospace Science and Technology* 10 (5 2006). ISSN: 12709638. DOI: `10.1016/j.ast.2005.11.006`.

[11] H. Görtler. *On the Three-Dimensional Instability of Laminar Boundary Layers on Concave Walls*. 1954.

[12] David Greenblatt and Israel J Wygnanski. "The control of flow separation by periodic excitation". In: *Progress in Aerospace Sciences* 36 (2000). DOI: `10.1016/S0376-0421(00)00008-7`.

[13] W. H. Hucho. *Aerodynamics of road vehicles*. SAE intl., 1987. DOI: `10.1016/C2013-0-01227-3`.

[14] R. A. Humble et al. "PIV Measurements of a Shock Wave/Turbulent Boundary Layer Interaction". In: (2006).

[15] Pierric Joseph, Xavier Amandolèse, and Jean Luc Aider. "Drag reduction on the 25° slant angle Ahmed reference body using pulsed jets". In: *Experiments in Fluids* 52 (5 2012). ISSN: 07234864. DOI: `10.1007/s00348-011-1245-5`.

[16] H. Kalyankar et al. "On the Use of Discrete Jets for Control of Moments on Tailless Aircraft". In: *AIAA Aviation Forum and ASCEND, 2024*. American Institute of Aeronautics and Astronautics Inc, AIAA, 2024. ISBN: 9781624107160. DOI: `10.2514/6.2024-3758`.

[17] Krishnan Mahesh. *The interaction of jets with crossflow*. 2013. DOI: `10.1146/annurev-fluid-120710-101115`.

[18] Abdelouahab Mohammed-Taifour, Arnaud Le Floc'H, and Julien Weiss. "Active forcing of a pressure-induced turbulent separation bubble". In: *AIAA Scitech 2020 Forum*. 2020. DOI: `10.2514/6.2020-1061`.

[19] Abdelouahab Mohammed-Taifour and Julien Weiss. "Periodic forcing of a large turbulent separation bubble". In: *Journal of Fluid Mechanics* 915 (2021). ISSN: 14697645. DOI: `10.1017/jfm.2021.77`.

[20] A N M Mominul Islam Mukut and Mohammad Zoynal Abedin. "Review on Aerodynamic Drag Reduction of Vehicles". In: *International Journal of Engineering Materials and Manufacture* 4 (1 2019). DOI: `10.26776/ijemm.04.01.2019.01`.

[21] Suman Muppidi and Krishnan Mahesh. "Study of trajectories of jets in crossflow using direct numerical simulations". In: *Journal of Fluid Mechanics* 530 (2005). ISSN: 00221120. DOI: `10.1017/S0022112005003514`.

[22] Stephen B Pope. *Turbulent flows. Turbulent Flows, by Stephen B. Pope.* Vol. 521591252. Cambridge University Press, 2000. DOI: `10.1017/CBO9780511840531`.

[23] Deepak Prem Ramaswamy and Anne Marie Schreyer. "Control of shock-induced separation of a turbulent boundary layer using air-jet vortex generators". In: *AIAA Journal* 59 (3 2021). ISSN: 1533385X. DOI: `10.2514/1.J059674`.

[24] Thomas T. Rice, Keith Taylor, and Michael Amitay. "Pulse modulation of synthetic jet actuators for control of separation". In: *Physical Review Fluids* 6 (9 2021). ISSN: 2469990X. DOI: `10.1103/PhysRevFluids.6.093902`.

[25] P. G. Saffman. *Vortex Dynamics.* Cambridge University Press, 1992. DOI: `10.1017/CBO9780511624063`.

[26] Rajes Sau and Krishnan Mahesh. "Dynamics and mixing of vortex rings in crossflow". In: *Journal of Fluid Mechanics* 604 (2008). ISSN: 14697645. DOI: `10.1017/S0022112008001328`.

[27] Rajes Sau and Krishnan Mahesh. "Optimization of pulsed jets in crossflow". In: *Journal of Fluid Mechanics* 653 (2010). ISSN: 14697645. DOI: `10.1017/S0022112010000388`.

[28] Hermann Schlichting and Klaus Gersten. *Boundary-Layer Theory.* 2016. DOI: `10.1007/978-3-662-52919-5`.

[29] Peter Scholz et al. "Performance optimization of jet actuator arrays for active flow control". In: *CEAS/KATnet Conference on Key Aerodynamic Technologies.* 2005.

[30] R L Simpson. "Turbulent Boundary-Layer Separation". In: *Annual Review of Fluid Mechanics* 21 (1 1989). ISSN: 0066-4189. DOI: `10.1146/annurev.fl.21.010189.001225`.

[31] Bryan Thwaites. "Boundary Layer and Flow Control, Volume I. Edited by G. V. Lachmann. Pergamon, Oxford, 1961. 600 pp. Illustrated. 10 gns." In: *The Journal of the Royal Aeronautical Society* 65 (609 1961). ISSN: 0368-3931. DOI: `10.1017/s0368393100075386`.

[32] D. R. Troolin, E. K. Longmire, and W. T. Lai. "Time resolved PIV analysis of flow over a NACA 0015 airfoil with Gurney flap". In: *Experiments in Fluids.* Vol. 41. 2006. DOI: `10.1007/s00348-006-0143-8`.

[33] B. Vukasinovic, Z. Rusak, and A. Glezer. "Dissipative small-scale actuation of a turbulent shear layer". In: *Journal of Fluid Mechanics* 656 (2010). ISSN: 14697645. DOI: `10.1017/S0022112010001023`.

[34] Julien Weiss, Abdelouahab Mohammed-Taifour, and Quentin Schwaab. "Unsteady behavior of a pressure-induced turbulent separation bubble". In: *AIAA Journal* 53 (9 2015). ISSN: 00011452. DOI: `10.2514/1.J053778`.

[35] Henri Werlé. *Le Tunnel hydrodynamique au service de la recherche aérospatiale.* O.N.E.R.A., 1974.

[36] Wen Wu, Charles Meneveau, and Rajat Mittal. "Spatio-Temporal dynamics of turbulent separation bubbles". In: *Journal of Fluid Mechanics* 883 (2019). ISSN: 14697645. DOI: `10.1017/jfm.2019.911`.

[37] Wen Wu et al. "Response of a turbulent separation bubble to zero-net-mass-flux jet perturbations". In: *Physical Review Fluids* 7 (8 2022). ISSN: 2469990X. DOI: `10.1103/PhysRevFluids.7.084601`.